Experimental Investigation of Disc Cavity Leakage Flow and Hub Endwall Contouring in a Linear Rotor Cascade

A THESIS
SUBMITTED TO THE FACULTY OF THE GRADUATE SCHOOL OF THE
UNIVERSITY OF MINNESOTA
BY

Ryan David Erickson

IN PARTIAL FULFILLMENT OF THE REQUIREMENTS
FOR THE DEGREE OF
MASTER OF SCIENCE

Terrence W. Simon, Adviser

APRIL 2010

Acknowledgments

I would first like to thank my adviser, Professor Terry Simon, for providing me with the opportunity to work along side him on this project. His guidance and level-headed approach to challenges have been appreciated. I have learned a lot from Terry in my time spent with him, and am also grateful for his friendship.

I would like to thank Solar Turbines, Inc. for their financial support during my studies. In particular, Hee Koo Moon and Luzeng Zhang, who have provided technical guidance throughout the project. I hope the project results are of great value to them.

A significant portion of this project was spent on the design and construction of wind tunnel components. Pat Nelsen, Robin Russell, and Bob Nelson were all involved in this process and proved to be excellent resources. Their time and effort working on this project are greatly appreciated. I would also like to thank Peter Zimmerman and Mark Erickson. Peter provided guidance and advice in the student machine shop, and Mark was a valuable resource anytime I needed tools, supplies, or advice.

I am grateful for the help and friendship my fellow graduate students provided during our time together. In no particular order, I would like to thank: Debashish Burman, Josh Quinnell, Krithiga Ganesan, Aaron Boomsma, Yen Seah, Smita Agrawal, Longzhong Huang, and summer student Jeff Diebold. I would also like to acknowledge the resources provided by the Minnesota Supercomputing Institute (MSI) during this project. In the design of heater circuits for the test section, Chris Mattson was gracious enough to provide electrical assistance. He proved that having friends who are also engineers can be convenient once in awhile.

Finally, I would like to thank my family. My wife and best friend, Alexis, is always willing to listen and offer encouragement. My brother, Evan, is always good for a much needed distraction offering conversations about things outside of work and school. Last, but not least, I would like to thank my parents. From a young age they instilled in me the importance of education. I would like to thank them for their support and direction along the way.

Abstract

Experimental and computational results which document mixing of passage flow and leakage flow in a rotor stage of a high pressure turbine are presented. Of specific focus are the effects of hub endwall contour geometries on mixing of the two flows and on film cooling coverage by the leakage flow over the endwall. The understanding of fluid physics in this area has received increased interest recently due to higher endwall heat loads as a result of new combustor designs.

The setting is a linear, stationary cascade which represents many features of the actual engine, such as geometry, Reynolds number, approach flow turbulence level and scale, and leakage mass flow rates. Rotation, density gradient, and upstream airfoil row effects are not represented. Two hub endwall geometries which give quite different acceleration profiles in the airfoil row entry plane region are examined. The flow field in the leakage flow delivery plenum, important to the mixing process, is characterized by measurements and computation.

The effects of leakage flow injection on the passage aerodynamic losses are also measured and computed. The loss pattern at the passage exit shows the effects of boundary layers on the pressure surface, the suction surface, and the two endwalls. Passage secondary flow features, such as remnants of the passage, horseshoe, and corner vortices are visible in the exit passage loss data. The effects of changes in leakage flow injection rate on the losses are found to be minimal for the cases studied.

Measurements of adiabatic effectiveness on the contoured endwall show coverage only over the upstream portion of the passage, with concentration on the suction side. The effects of the horseshoe and corner vortices on mixing of the leakage and passage flows are evident in the effectiveness pattern. Computed effectiveness distributions show similar trends to those seen in the measurements; however, measured effectiveness values are generally lower than computed values, indicating the more rapid dissipation of turbulent transport in the computations than in reality. Comparison of effectiveness distributions shows that the contoured endwall geometry referred to as the “dolphin nose” leads to better overall film cooling coverage on the endwall.

Table of Contents

List of Tables

List of Figures

Nomenclature

Symbols

a	Pipe Radius [m]
A	Hotwire Calibration Constant [dimensionless]
B	Hotwire Calibration Constant [dimensionless]
C	Blade Chord Length [m]
C_{ax}	Axial Chord Length [m]
C_p	Coefficient of Pressure [dimensionless]
$C_{p,Loss}$	Total Pressure Loss Coefficient [dimensionless]
$\overline{C}_{p,Loss}$	Mass Averaged Pressure Loss Coefficient [dimensionless]
D	Pipe Diameter [m]
E	Electrical Potential [volts]
$E(\omega)$	Energy Density Spectrum [$m^2/s^2 \cdot Hz$]
ℓ	Length Scale [m]
Lu	Turbulence Energy Length Scale [m]
n	Hotwire Calibration Constant [dimensionless]
r'	Pipe Radial Coordinate [m]
$u(t)$	Instantaneous Fluctuation about Time Averaged Velocity [m/s]
u'	Root Mean Square of Velocity Fluctuations [m/s]
U_e	Effective Hotwire Cooling Velocity [m/s]
U_o	Pipe Centerline Velocity [m/s]
U_τ	Shear (or Friction) Velocity [m/s]
$U(t)$	Instantaneous Velocity [m/s]
$\overline{U}$	Time Averaged Velocity [m/s]
M	Mach Number [dimensionless]
MFR	Leakage-to-Mainstream Mass Flow Ratio [dimensionless]
N	Sample Size [dimensionless]

P_d Dynamic Pressure [Pa]

P_s Static Pressure [Pa]

P_t Total Pressure [Pa]

Q Volumetric Flow Rate [m^3/s]

R Specific Gas Constant for Air [J/kg·K]

Re_C Reynolds Number scaled on Blade Chord Length [dimensionless]

Re_D Reynolds Number scaled on Pipe Diameter [dimensionless]

Re_{Lu} Reynolds Number scaled on Energy Length Scale [dimensionless]

Re_λ Reynolds Number scaled on Taylor Microscale [dimensionless]

S Blade Span [m]

t Time [sec]

T Absolute Temperature [K]

Tu Turbulence Intensity [%]

x Passage Axial Coordinate [m]

y Passage Pitchwise Coordinate [m]

z Passage Spanwise (Endwall-Normal) Coordinate [m]

Greek

ρ Density [kg/m^3]

Δ Difference Operator

Λ Turbulence Integral Length Scale [m]

η Adiabatic Effectiveness Value [dimensionless]

ε Dissipation Rate of Turbulence Kinetic Energy [m^2/s^3]

λ Taylor Microscale (or Lateral Dissipation Scale) [m]

ν Kinematic Viscosity [m^2/s]

ϕ Fast Fourier Transform Algorithm Output

θ Recovery Temperature [dimensionless]

ω Frequency [Hz]

ω_s Sampling Frequency [Hz]

μ Dynamic Viscosity [Pa·sec]

Subscripts

0 Located at Passage Inlet Plane

1 Located at Passage Exit Plane

ℓ Located at Leakage Flow Rim Seal Slot

w Wall Property

Superscripts

$\bar{}$ Time Averaged Quantity

$'$ Instantaneous Quantity

Chapter 1

Introduction and Background

1.1 Motivation

In 1939 the gas turbine experienced its first practical usage in the areas of power generation and aviation. At that time, turbines operated at a thermal efficiency of around 18% according to Langston [1]. Through a period of steady development over the last 70 years, incremental improvements have led to thermal efficiencies as high as 60% for land based "combined cycle" configurations of the gas turbine. The present study aims to continue in the spirit of this rich history leading to the advancement of gas turbine technology.

One relatively recent topic of interest within the field of gas turbines is that of exhaust emissions. Restrictions on the amount and type of emissions have led to new combustor designs which keep emissions within acceptable levels. Interestingly enough, the new designs have reduced peak combustion temperatures which cause the formation of emissions such as nitrous oxides, while increasing the averaged turbine inlet temperature. Essentially, the change has "flattened" the working fluid's temperature profile through more efficient combustor mixing. The modified temperature profile has in turn led to increased heat loads on endwall surfaces requiring improved cooling schemes. One of those components affected, the hub endwall, is the focal point of this study.

To effectively protect an endwall from extreme temperatures, one must first understand the flow physics which influence heat transfer. For example, fluid moving over the endwall is largely affected by secondary flows. Several vortical structures disturb the endwall boundary layer making it highly three dimensional. In addition, a cross-stream pressure gradient drives endwall flow toward the suction side of the passage. These features make endwall cooling a difficult task. Also, any changes made to improve endwall thermal protection must be such that they only minimally impact stage efficiency. These considerations can pose a significant dilemma for designers, as

the best thermal protection scheme is not likely to be the most aerodynamically efficient scheme.

One method of trying to weaken secondary flows and improve endwall cooling effectiveness is endwall contouring. This method, as a subject of the present study, has been around since the early 1960's. It most likely originated as a response to the discovery and characterization of passage secondary flows in the 1950's. Of particular interest in this study is how endwall contouring affects mainstream and disk cavity leakage flow mixing. This mixing process largely dictates passage secondary flow losses and leakage flow endwall cooling coverage. In an effort to improve performance in these areas, two new endwall geometries and three representative leakage flow blowing rates are studied herein.

1.2 Objectives

In the present study, experiments and supplementary computations are carried out in order to compare the aero-thermal performance of two new axisymmetric endwall contour geometries. Properties measured and computed for comparison include endwall adiabatic film cooling effectiveness, passage temperature fields, and passage aerodynamic losses. Special attention is paid to determine whether the endwall curvature has any effect on secondary flows within the passage. The gathered information is intended to assist designers in determining the applicability of these endwall designs within a real turbine. In addition to endwall contouring effects, a range of disc cavity leakage flow rates is investigated. This information is meant to quantify, over the range tested, the benefits and penalties of introducing leakage flow into the passage using the designated endwall contouring.

Chapter 2

Background on Turbine Endwall Aerodynamics and Heat Transfer

The background provided herein is an abbreviated summary of research relating to turbine endwall aerodynamics and heat transfer. Several excellent review papers exist on these topics in the open literature which survey experimental results dating back to the 1950's. For a more comprehensive review of the topics at hand, the reader is encouraged to refer to these reviews which are referenced in their appropriate sections.

Due to the difficulty in making fluid mechanics and heat transfer measurements within a gas turbine, it is commonplace in the history of turbine research to see simplified test section geometries. There are many variations of these simplified geometries, but the most common ones to be discussed will fit into general categorizations such as linear cascades and rotational test rigs. Research in Computational Fluid Dynamics (CFD) is also spread over a wide range of these geometries. For this reason, the information provided herein will begin with early studies done in linear cascades and build upon them information from more complex geometries. The first section describes the current understanding of endwall aerodynamics and heat transfer. The second section contains discussion of disc cavity leakage flow and air injection upstream of a passage as well as the effects of endwall contouring. These techniques have shown promise under certain conditions to modify flow and heat transfer characteristics near the endwall. The short discussion of these topics should give the reader a good understanding of the background and motivation leading up to the current study.

2.1 Endwall Flow and Heat Transfer in Cascades

The evolution of our understanding of secondary (or endwall) flows is documented in a 1985 review by Sieverding [2]. Here, the common constituents of passage secondary flows are presented with explanations of their origins. While these features are referred

to individually for discussion purposes, it should be noted that they interact highly with each other inside the passage.

The first and largest secondary flow feature is the passage vortex. This vortex is initiated by the presence of vorticity (due to boundary layers) in the fluid entering the passage. Within the passage, the blade curvature causes flow turning and distortion of the inlet vorticity due to a cross-stream pressure gradient. This distortion is, in effect, the growth of the passage vortex. The passage vortex evolution is shown by Sieverding and Van den Bosch [3] in Figure 1. They used colored smoke to visualize stream surfaces moving through a cascade. Of particular importance to the passage vortex description above is the stream surface in Figure 1 marked with dashes and labeled "SS2." Other features of this figure will be described later. The surface "SS2" lies outside the endwall boundary layer at the passage inlet. Moving downstream, one sees that the dashed stream surface begins to roll-up with the fluid nearest the blade pressure side moving toward the suction side of the passage. This roll-up motion is shown here to entrain fluid originally outside of the inlet boundary layer. It is called the passage vortex.

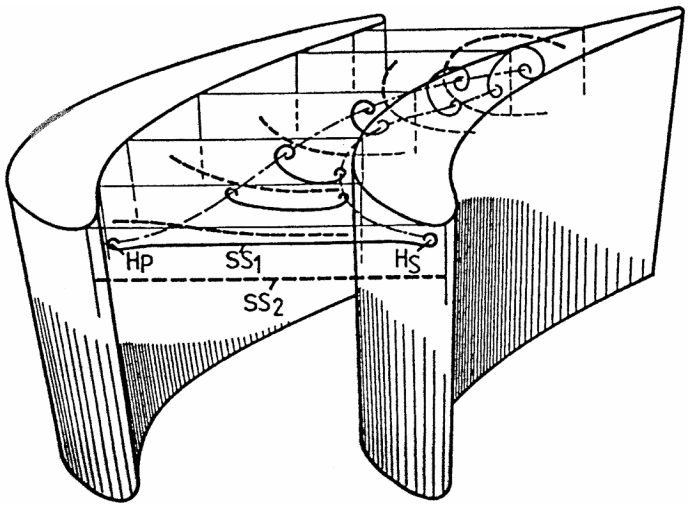

Figure 1. Synchronous Evolution of Horseshoe and Passage Vortices after Sieverding and Van den Bosch [3]

A very closely related feature to the passage vortex is the horseshoe (or leading edge) vortex. It has been shown that a boundary layer approaching a blade cascade separates near the blade leading edge to form a horseshoe vortex. The two "legs" of this vortex rotate in the opposite sense and travel into adjacent passages. The size of this

vortex is greatly dependent upon the approach flow incidence angle. Langston [4] produced a popular figure which illustrates the formation of horseshoe vortices in a blade passage. In Figure 2, the pressure side leg of the horseshoe vortex, which will be referred to as H_p, is labeled "passage vortex." This leg originates near the blade leading edge and migrates from the pressure side of the passage toward the suction side due to the cross-stream pressure gradient. It is strengthened by the endwall crossflow, as was the passage vortex in Figure 1. Through careful study, it was found that the passage vortex and the H_p vortex become one, since they have the same rotational direction and are both driven by the endwall crossflow. This is the reason that Langston simply labels this vortex as "passage vortex" in Figure 2. Referring back to Figure 1, one sees that the H_p vortex migrates across the passage along a smooth curve without noticeable vortical motion. Along its path, the H_p vortex is enveloped by the stream surface marked "SS2." Even though the passage vortex and H_p vortex merge, Sieverding [2] treats them as separate features due to their slightly different origins. He further states "that the reduction or elimination of the leading edge horseshoe vortices will indeed have little effect on the shape and position of the passage vortex." This conclusion disagrees with that of Langston [5], and possibly merits further study. In this review, the passage vortex and the H_p vortex are treated as separate features for discussion purposes. The current level of understanding leaves some "fuzziness" to these definitions.

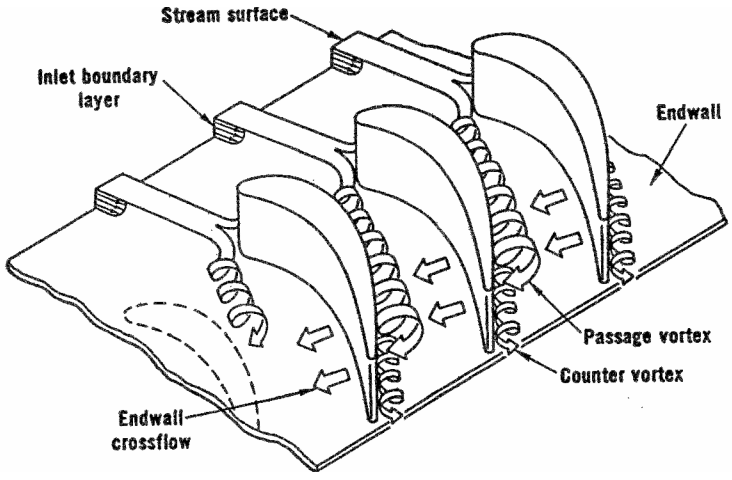

Figure 2. Three-Dimensional Separation of a Boundary Layer Entering a Turbine Cascade from Langston [4]

The second leg of the horseshoe vortex, H_s, originates near the blade leading edge and closely moves along the suction side of the blade, as shown in Figure 2 (labeled "counter vortex"). Since its rotation is opposite to that of the passage vortex, the H_s vortex is weakened due to shear with the passage vortex and endwall crossflow. Due to this interaction, the position of the H_s vortex at any location within the passage varies with the rotational speed of the passage vortex. In his review of endwall secondary flows in 2000, Langston describes the H_s vortex "as a 'planet' possibly rotating about the axis of the passage vortex (the 'sun'). Thus, the position of the counter vortex relative to the passage vortex may be different" than that shown in Figure 2.

Supplementary flow models have been developed more recently which show additional complexities of secondary flows. An example is a study by Wang et al. [6] where detailed visualization of secondary flows was made within a blade cascade with laser light and smoke. These experiments were run at lower-than-engine operating Reynolds numbers to facilitate the smoke visualization, so further verification of all features is a possible topic of future study. The resulting endwall flow model is shown in Figure 3. Of particular interest is documentation of the corner vortices and an induced vortex at the location where the H_p vortex intersects with the blade suction side (labeled "V_{wip}" in Figure 3). The induced vortex rotates in the opposite sense to that of the passage vortex, thus adding to the total dissipation of kinetic energy within the passage. The locations and sizes of corner vortices, which have been documented prior to this study, are somewhat dependent upon the cascade geometry. Highly-loaded blade designs are more likely to show distinct corner vortices.

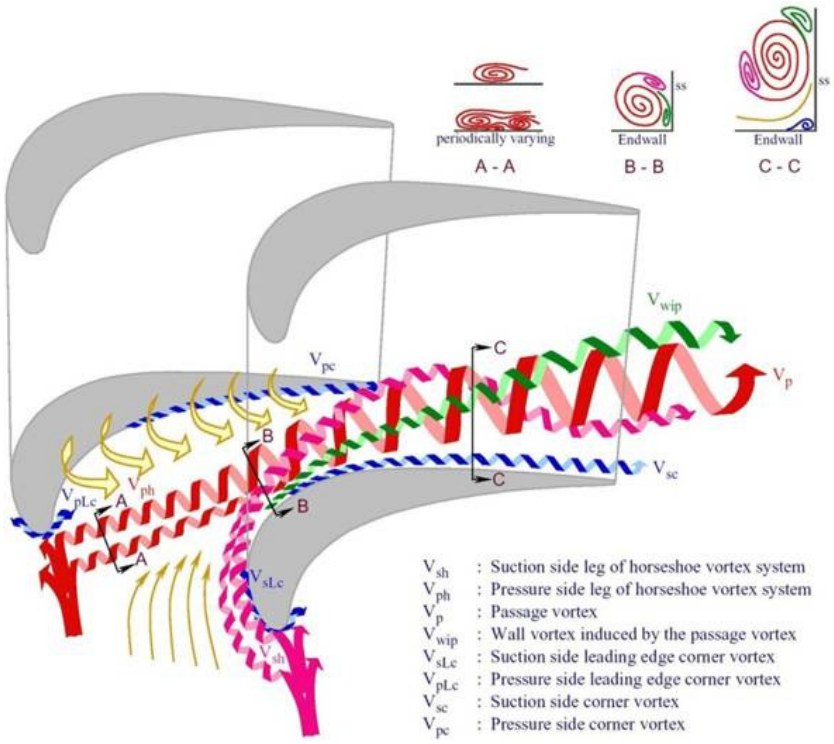

Figure 3. Endwall Secondary Flow model of Wang et. al. [6]

It is clear from these flow models that the nature and interactions of endwall secondary flows are very complex. Information presented so far has dealt with cascade studies having only flat endwalls. The addition of other real complexities, such as non-uniform inlet velocity fields, rotation, off-design conditions, disc cavity leakage flows, and contoured endwalls only reveals the many challenges ahead if we are to completely understand endwall secondary flows. Simon and Piggush [7] produced a review which considers some of these additional complexities and incorporates the current (as of 2006) state of understanding with available studies.

Regardless of the level of understanding of secondary flows in complex geometries, the net outcome is seen in the form of aerodynamic losses. These losses are irreversibilities that occur within the passage due to viscous dissipation. Some of the losses that occur over a turbine stage are directly attributable to secondary flows and boundary layers, while others occur in the turbulent freestream flow. According to Sharma and Butler [8], the total aerodynamic losses attributed to secondary flows can be as high as 30-50% of the total passage losses. The magnitudes of aerodynamic losses are

largely geometry dependent, making direct comparisons of data from other studies impossible.

A comprehensive survey of endwall heat transfer work is given in the review of Simon and Piggush [7]. The existing literature reveals that heat transfer patterns over the endwall surface are largely shaped by the secondary flow paths. Vortices shearing along the endwall tend to create locally high heat transfer coefficients. As an example, work by Goldstein and Spores [9] is included in Figure 4 which shows results of mass transfer measurements made along the endwall of a rotor cascade. The mass transfer coefficients offer insight into heat transfer through the heat-mass transfer analogy; however, for the current discussion purposes, the shapes of the contour patterns are of most concern.

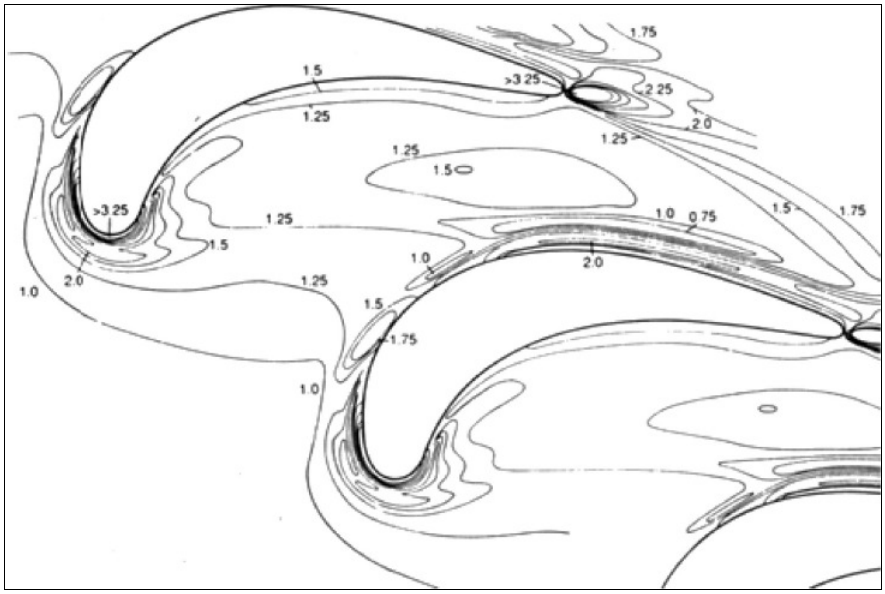

Figure 4. Mass Transfer Increase over Flat-Plate Values for a Turbine Rotor Cascade from Goldstein and Spores [9]

Slightly upstream of the passage, the mass transfer contour level of 1.0 is shown to distort towards the passage suction side due to the cross-stream pressure gradient. Additionally, near each blade's leading edge, high mass (or heat) transfer coefficients are seen to "wrap" around the blade with very high values along the endwall-to-suction side corner. This is evidence of the horseshoe vortex's influence in this area. Some evidence of the H_p vortex moving across the passage towards the blade's suction side may be seen in elevated mass transfer coefficient levels (>1.25) in the middle of the passage. Along the

back half of the endwall near the blade's suction side, elevated levels indicate the effects of the passage vortex and corner vortices. Similarly, at the other side of the passage, a mass transfer coefficient of 1.5 exists near the blade's endwall-to-pressure side corner. This is likely evidence of a corner vortex. Along the endwall near the blade trailing edge very high mass transfer coefficients are seen which rival those near the leading edge. These levels show the significance of blade wakes on endwall heat transfer.

2.2 Effects of Disc Cavity Leakage Flow and Endwall Contouring

A step forward from the various studies which relate to continuous, flat endwalls, is the addition of leakage (or purge) flow ejection at the stator-to-rotor interface. At this interface, a small cavity is designed into the engine to provide clearance between the rotor disc and the stator. The dimensions of this cavity can vary as a result of transient operating conditions. The ideal cavity is as small as practical. The cavity must be designed to protect from hot gas ingression. Current designs meter flow bled from the high pressure compressor into the cavity using labyrinth seals, as shown in Figure 1 (Taken from Dénos et al. [10]). This flow, used to prevent ingression of hot gas from the passage, offers cooling potential. This disc cavity leakage flow will have an effect on endwall secondary flows. In studies of cascades with upstream air injection, researchers such as Blair [11], Biesinger and Gregory-Smith [12], and others, have shown that injecting air upstream of passages through slots and holes can, in some cases, influence the formation of secondary flows (sometimes deduced from heat transfer measurements). Their geometries, used for air injection experiments to test for the control of secondary flows were predominantly slots, instead of disc cavities. Nevertheless, their findings are relevant. Under certain conditions, various researchers (see Simon and Piggush [7]) were able to decrease the effects of secondary flows on losses and heat transfer. Special consideration in these cases was given to injected air-to-mainstream pressure ratios, mass flow rates, and injection angle. While these cases have shown promising results, it is also likely that injected air (or in the case of a rotor, leakage flow) can have a negative impact on aerodynamic efficiency. Thus, in the case of disc cavity leakage flow, the injection

geometry becomes very important as it helps dictate the mixing interaction between hot gas path flow and leakage flow which exits the disc cavity.

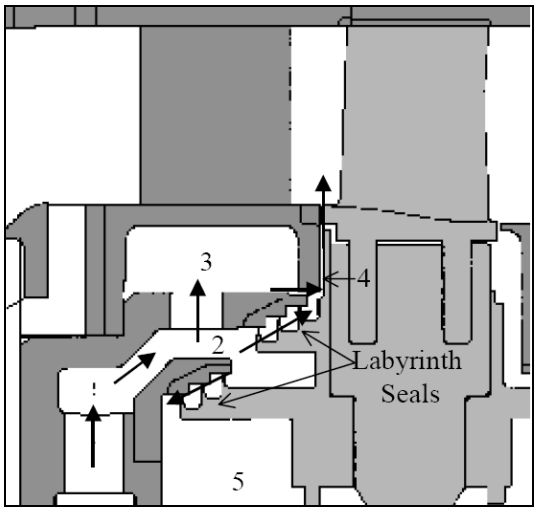

Figure 5. Representative Engine Cross-Section showing location of Labyrinth Seals and Disc Cavity from Dénos et al. [10].

Another important consideration of disk cavity leakage flow is that the use of excess air offers an efficiency penalty since that compressor discharge air is not heated in the combustor or expanded in the vane row. Thus, though it may provide cooling, it must be used sparingly. Unfortunately, studies documented in the literature of disk cavity leakage flow and effects on endwall flow and heat transfer are geometry dependent. Various designs of disc cavities present in the literature show leakage flow being discharged radially, tangentially, or at angles which range between these two extremes with respect to the mainstream flow. Most early studies in this area focused on the problem of parallel disks (one rotating) with a shroud, as described in a review by Owen [13]. Many of the parallel disc studies focus on the problem of finding the minimum coolant flow rate for preventing ingression, such as that of Bhavnani et al. [14]. Ko et al. [15], and others, investigated thermal transport at the disc cavity/mainstream interface with a parallel disc geometry. Such research identified recirculation zones within the cavity where ingested mainstream fluid could create thermal-stress problems. More recently, Cao et al. [16] performed unsteady CFD simulations in a parallel disc geometry that did not include blades. They identified rotating flow features within the disc cavity that resulted in

alternating cells of ingression and ejection. These cells were verified by pressure measurements in a two-stage turbine rig. They were found to not be strong functions of disk speed. The cells generally rotated at 90-97% of the rotor disc speed and were hypothesized to be driven by instabilities at the mainstream/disc cavity interface. This particular study is interesting as most unsteady ingression/ejection behavior was previously attributed to asymmetries in the rotor inlet pressure field caused by stator wakes.

Several recent numerical/experimental studies from the von Kármán Institute (e.g. Dénos et al. [10], Paniagua et al. [17], and Pau et al. [18]) focused on the effects of leakage flow on the mainstream flow. Their geometry essentially matches the case previously discussed of a radial outflow disc cavity with no step between the stator rim and the rotor hub; however, it included also the effects of blading, temperature ratio, Mach number, and operating Reynolds number. In general, they found that leakage flow increases secondary flow losses, as most of it is entrained into the main passage vortex. This finding suggests also that leakage flow has cooling potential for the endwall, but only in the upstream portion of the passage (path of the H_p vortex).

Other disc cavity designs can be found in the open literature. These designs allow for leakage flow ejection which is not entirely radial. Such a design requires contouring of the rotor hub endwall; a subject which has not yet been broached in this review. Endwall contouring has been studied extensively as a means of slowing the growth of secondary flows. Positive results have been seen in cases where the wall contour causes acceleration of the endwall boundary layer flow upstream or inside the passage. Most of these studies have taken place within inlet guide vane cascades. Documentation of many of these studies is available within Burd [19] and Simon and Piggush [7]. Burd highlights one of the more promising endwall contours for inlet guide vanes where the contour causes a reduction in passage area slightly upstream of the blade trailing edge. This allows much of the passage flow turning to occur at lower velocities and acceleration in the rear of the passage to decrease aerodynamic losses.

With the knowledge of endwall contouring studies within passages of inlet guide vane rows, it is now desirable to relate that information over to rotors passages. More

specifically, to how contouring can affect the injection of disc cavity leakage flow. A study by Girgis et al. [20] showed that stage efficiency with tangential leakage flow injection can improve cooling over that with radial injection. Another study considering disc cavity flow and endwall contouring by Ong et al. [21] incorporates a very small downward step between the stator rim and a rounded rotor platform. The leakage flow in this case is injected through a labyrinth-type seal in their rotating rig. Their geometry is shown in Figure 6.

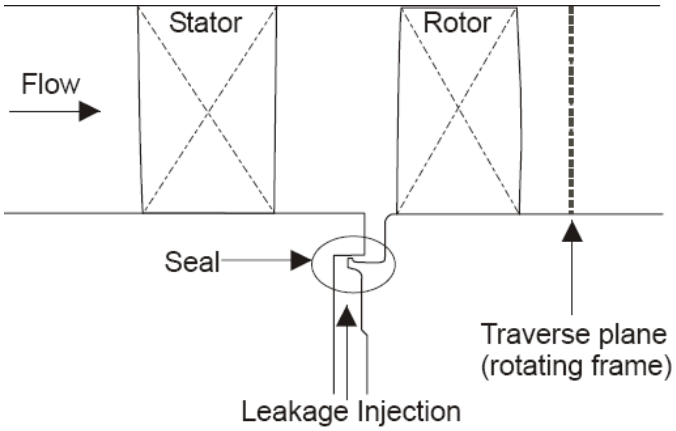

Figure 6. Low Speed Research Turbine Geometry of Ong et al. [21]

Their findings reveal that leakage flow enters the passage with less swirl than that of the main flow, effectively decreasing efficiency in downstream blade rows due to enhanced mixing by stronger secondary flows. They also cite the velocity difference of leakage and mainstream flows as a source of loss at the injection location due to mixing, and note an improvement in stage efficiency when injecting leakage flow with additional swirl. A similar computational study by Marini and Girgis [22] looks at the effect of modifying the endwall leading edge shape on mainstream/leakage flow interaction. They compared one endwall contour that was recessed below the stator rim having gradual curvature with one that was level with the rim. Their two leading edge contour geometries are shown in Figure 7.

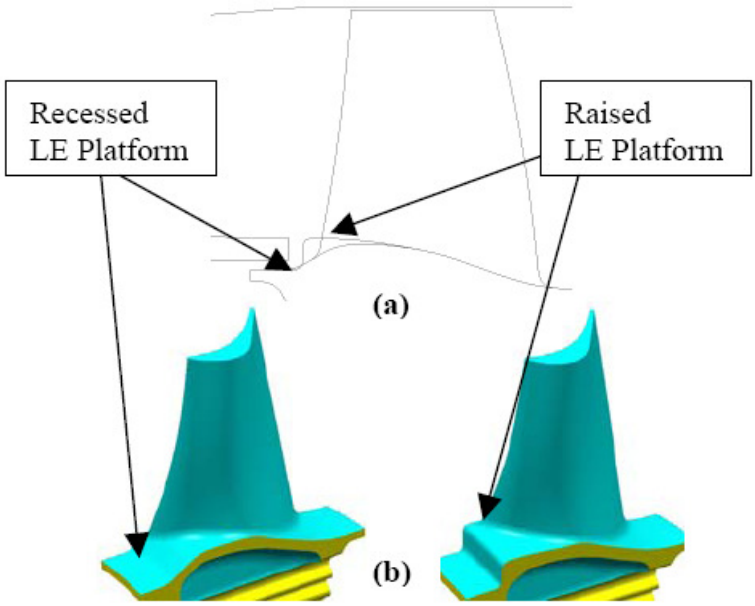

Figure 7. Blade Leading Edge Endwall Shapes of Marini and Girgis [22]

Results suggest that the recessed endwall design is more sensitive to changes in leakage flow rates and produces lower stage efficiency than that computed with the no-step counterpart. Thus, the raised endwall contour geometry is a more stable option under off-design conditions. The few studies above indicate the recent interest in endwall contouring as applied to the rotor hub endwall. They have led to important findings, but much remains to be learned with the complex geometries and secondary flows involved. The current study incorporates two new endwall leading edge contours as well as multiple leakage flow blowing ratios inside of a cascade with rotor blade profiles. The leakage flow injection path is simulated through a flow delivery box with dimensions taken from a disc cavity of a real engine. Further descriptions of the current test section geometry are given in the following chapter.

Chapter 3

Experimental Test Facility

3.1 Wind Tunnel

The wind tunnel facility is designed to deliver properly conditioned flow to the test section. It is of the subsonic, open return type and is comprised of four sections being the main fans, auxiliary fans, turbulence generator, and nozzle. Several modifications to the pre-existing wind tunnel were required for this study. Figure 8 shows the final layout of the wind tunnel's various components. Their details will be discussed in the following sections.

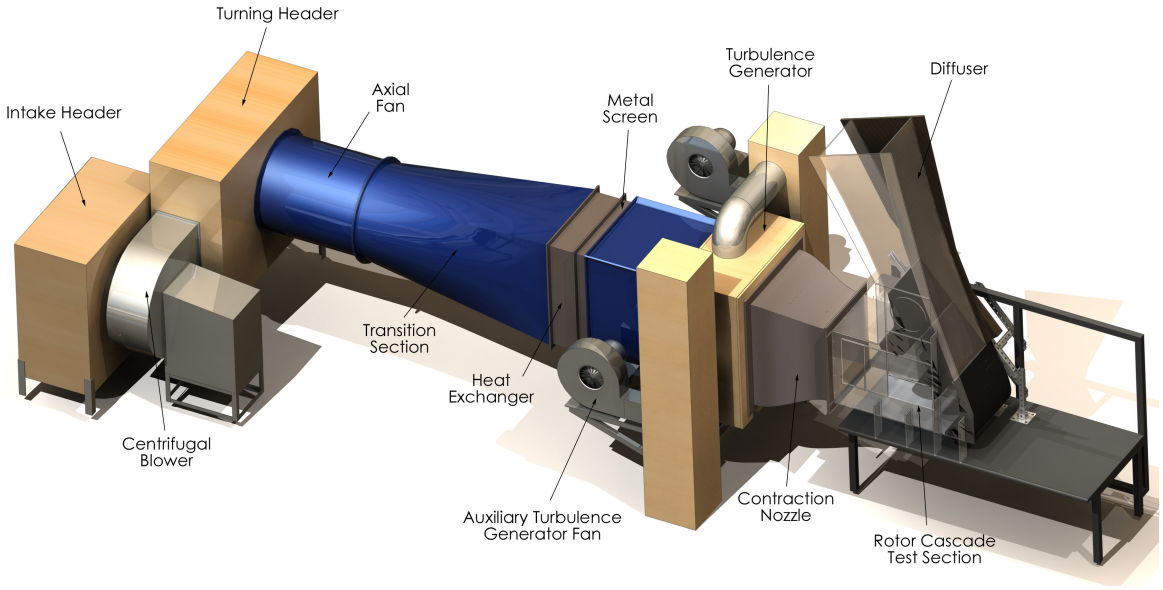

Figure 8. Wind Tunnel Layout

3.1.1 Main Flow and Fans

At the intake of the wind tunnel is a large header fitted with several air filters. The room air is filtered as it passes through the header and drawn into a 3.7kW (5HP) centrifugal blower (General Purpose Fan, size 183 ACF) made by The New York Blower Company. This blower was not part of the original base wind tunnel but was added later to achieve

increased fan power. At the outlet of this blower, the pressurized air travels through a large 90º turning header and into the base wind tunnel.

The base wind tunnel was designed and built by Engineering Laboratory Design, Inc. It is powered by a 5.6 kW (7.5 HP) axial flow fan (Axivane Model No. 29-17-1770AP) by Joy Manufacturing Company. The fan is outfitted with a motor speed controller (Toshiba Model No. VFS11-2075PM-WM) allowing variable operating frequency between 0-60 Hz at increments of 0.1 Hz. Downstream of the fan is a radial-to-square fiberglass transition section connected to an air cooled heat exchanger. The heat exchanger is not utilized in this study; however, along with a metal screen it helps remove any large scale rotation and/or vorticity created by the axial fan. Completing the base wind tunnel is an open settling chamber which lies just upstream of the turbulence generator.

3.1.2 Auxiliary Flows and Fans

Due to the high flow rates involved in this study, several auxiliary fans are utilized to deliver air to various locations of the wind tunnel. Each auxiliary fan is dedicated to a specific component within the wind tunnel or test section and does not simply supplement the main flow fans. The three components fed by auxiliary fans are the turbulence generator, temperature conditioning slot, and leakage flow plenum.

3.1.2.1 Auxiliary Turbulence Generator Flow

As will be described further in Section 3.1.3 below, the turbulence generator uses two separate flows during operation. The first flow is simply the main flow as described in Section 3.1.1. The secondary (auxiliary) flow is provided by two identical 3.7 kW (5 HP) centrifugal blowers (Model 4C330) made by the Dayton Electric Manufacturing Company. One blower is positioned on each side of the wind tunnel next to the turbulence generator. Connected to each blower is a large flow distribution cabinet approximately 2.32 m x 0.42 m x 0.43 m (7.62 ft x 1.38 ft x 1.42 ft) in size. The cabinets are used to supply flow to all four sides of the turbulence generator using 25.4 cm (10 in.) diameter ducting as seen in Figure 9. The 90º elbows used in the top and bottom delivery

lines are packed with a plastic honeycomb material to reduce swirling effects. Further discussion of the flow after it enters the turbulence generator is offered later in Section 3.1.3.2.

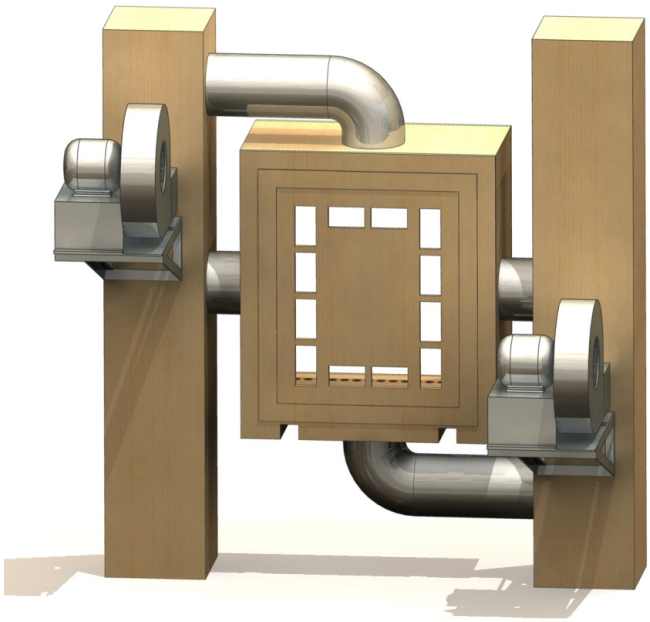

Figure 9. Auxiliary Flow Delivery to Turbulence Generator

3.1.2.2 Auxiliary Temperature Control Slot Flow

Another component that is supplied by an auxiliary fan is the approach flow temperature control slot. This element is actually part of the test section and lies just downstream of the nozzle. Its supply flow is provided by a 1.5 kW (2 HP) centrifugal blower (Model HPB) made by the Cincinnati Fan and Ventilator Company, Inc. A MagneTek GPD333 motor controller drive is used to adjust the fan's rotational speed by means of pulse width modulation. Increments of 0.1 Hz are available for adjusting the fan motor frequency within a 0-60 Hz range. As the flow exits the fan, it travels through approximately 2.3 m (7.5 ft) of 10 cm (4 in.) diameter Class B gas vent piping. Inside these pipes, are a total of eight heating elements which can provide up to 2.8 kW of heating power. The piping connects to a header which turns and redistributes the flow. A fine screen is placed at the exit of the header to help further distribute the exit flow by creating an additional pressure drop. The header is then connected directly to the acrylic plenum which

supplies the temperature control slot. Details regarding the temperature control slot are given in Section 3.2.4.

3.1.2.3 Auxiliary Leakage Flow

A very critical part of this study is the topic of leakage flow dynamics. This section is devoted to the components used to ensure proper delivery and metering of flow to the leakage plenum. Details regarding the plenum and its purpose are covered later in Section 3.2.3. Providing the fan power for the leakage flow is a 1.5 kW (2 HP) centrifugal blower (Model HPB) made by the Cincinnati Fan and Ventilator Company, Inc. The fan's rotational speed is regulated through the use of a MagneTek GPD333 motor controller drive identical to the temperature control slot's drive. Connected to the fan's outlet is a PVC flange and 38 cm (15 in.) section of schedule 40 straight pipe. The piping is 10 cm (4 in.) in diameter and packed with approximately 500 small straws (3 mm I.D.) which act as flow straighteners. Downstream of the flow straightener is a long length of straight pipe having an ℓ/D of 14.25. This piping serves as a development length before the flow is introduced to a Meriam Instrument "Laminar Flow Element", Model 50MC2-4 (Section 4.4.1). A differential pressure reading is made across the laminar flow element by connecting the pressure ports of the flowmeter and a Dwyer Instruments inclined tube manometer (see Section 4.3.1.2) with equal lengths of ¼" I.D. Tygon tubing. Through the use of the manometer and motor controller, the leakage flow rate may be monitored and adjusted as necessary in real-time. Connected on the downstream side of the flowmeter is another section of straight PVC pipe with an ℓ/D of 12. The lengths of straight pipe connected to the flowmeter should be adequate as the manufacturer (Meriam Instrument) recommends a minimum of 10 diameters upstream and 5 diameters downstream. Attached to the end of the straight pipe is a round-to-square duct transition section followed by a large header. This header turns the flow 90º and connects to the leakage flow plenum where the air is drawn into the test section.

3.1.3 Turbulence Generator

The turbulence generator's function is to create a uniform turbulence intensity distribution with large eddy length scales. Such turbulent flow is characteristic of current dry low NO_x combustors. In this respect the turbulence generator may be thought of loosely as a combustor simulator. The ultimate goal, however, is to create a properly conditioned inlet flow to the test section and not accurately simulate any one combustor design. The current apparatus was redesigned from a previous version within the laboratory (See Oke [23]) to satisfy flow rate requirements. The underlying theory for both turbulence generators was based on the recommendations of Ames [24], Chung [25], and Wang [26].

In principle, the apparatus is a large mixing volume where two separate flows, namely the core and cross flows, are allowed to interact and create shear. The mixing volume has a width of 76.2 cm (30 in.), height of 91.4 cm (36 in.), and depth of 53.3 cm (21 in.) yielding an aspect ratio of 1.2. Delivered by the wind tunnel as described in Section 3.1.1, the core flow approaches the turbulence generator and is abruptly met with a large blockage. This blockage lies normal to the flow direction and is the turbulence generator's front face seen in Figure 10 (left). Slot openings are machined into the front face to create strong streamwise jets that pass into the turbulence generator's mixing zone. Inside the mixing zone a second flow, called the cross flow, is delivered as described in Section 3.1.2.1 and injected from holes in the turbulence generator's side walls. The holes are aligned in two rows along the perimeter of the apparatus as seen in Figure 10 (right). These holes create circular jets which are oriented normal to the streamwise direction causing very strong interaction between the core and cross flow jets. Both the mixing of the jets and the spacing between slots and holes are important for the formation of turbulent eddies.

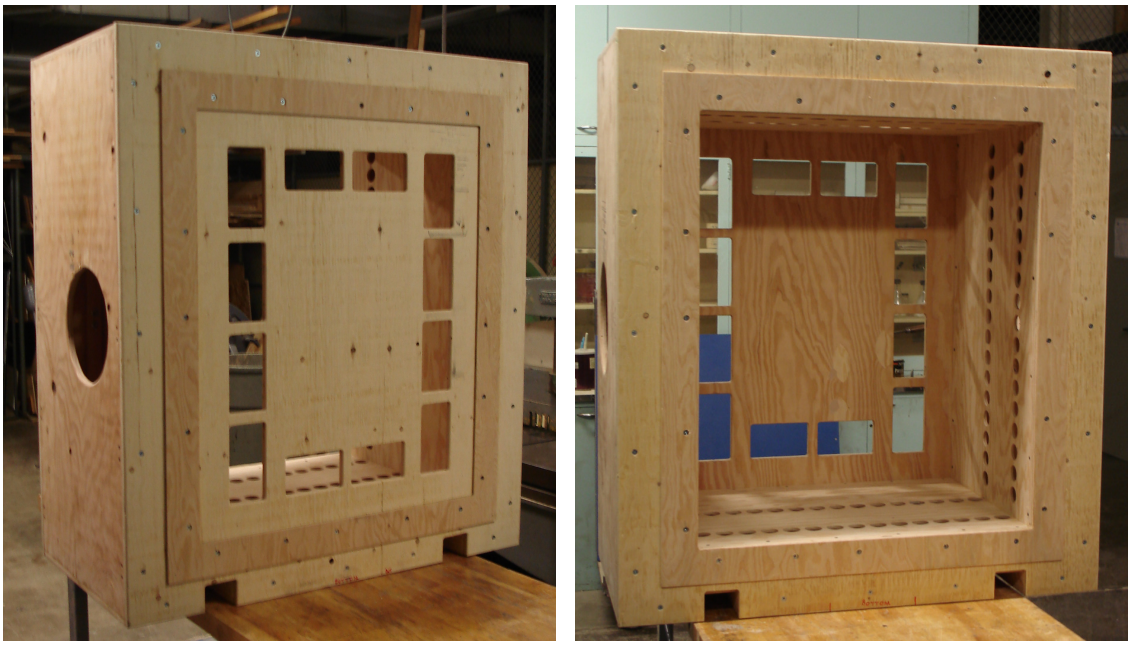

Figure 10. Turbulence Generator Front View (Left) and Back View (Right)

3.1.3.1 Core Flow Jets

The core flow jets are created as air travels through twelve rectangular slots in the turbulence generator's front face. There are two slightly different slot sizes used depending on whether the slot's long edge is oriented vertically or horizontally. A total of eight vertical slots are used with lengths of 17.2 cm (6 ¾") and widths of 8.9 cm (3.5 in.). The four horizontal slots have dimensions of 15.2 cm (6 in.) by 8.9 cm (3.5 in.). As seen in Figure 11, all slots are offset from the connection flange's inner edge approximately 7.6 cm (3 in.). This is also the distance from the downstream tunnel walls since they line up with the connection flange's inner edge. Spacing between neighboring slots is typically 2.5 cm (1 in.) regardless of whether they are vertical or horizontal slots. The only exception occurs where there is a neighboring slot of a different direction, in which case the spacing is doubled.

The total flow area opened up by the core flow slots is approximately 1760 cm^2 (273 in^2) which results in an average jet velocity of roughly 8 m/s. Just behind (downstream of) the front face, both regions of strong streamwise momentum and very low momentum

are created due to the presence of the blockage. This geometry is critical in order to create large recirculation zones in the mixing zone.

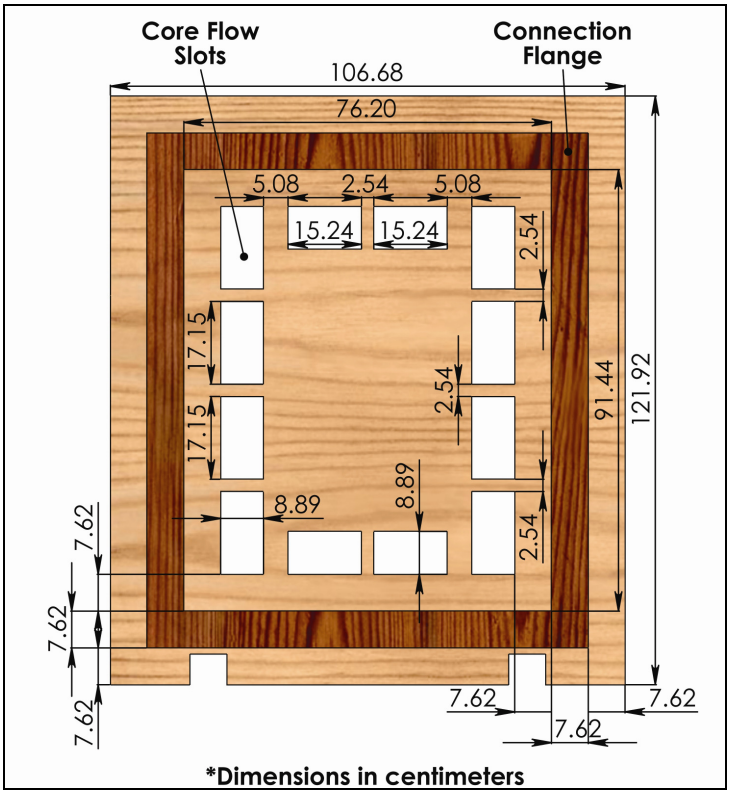

Figure 11. Front Face of Turbulence Generator

3.1.3.2 Cross Flow Jets

Situated along the perimeter of the turbulence generator's inside walls are two rows of holes as seen in Figure 12. These holes create circular jets, referred to as the cross flow jets, which pass into the mixing zone of the turbulence generator. Each hole has a diameter of 3.8 cm (1.5 in.) and within their respective row they are spaced on 5 cm (2 in.) centers. The first row of holes is located 25.4 cm (10 in.) downstream of the turbulence generator's front face and the distance between rows is 17.8 cm (7 in.) on all four inside walls.

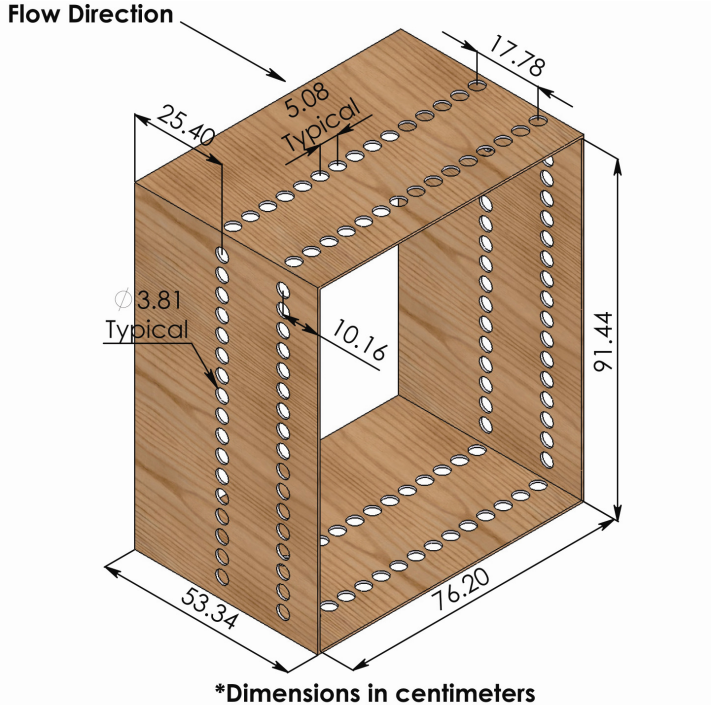

Figure 12. Turbulence Generator Cross Flow Walls

The total flow area for the cross flow jets is 1460 cm^2 (226 in^2) with each jet having a velocity around 18 m/s. All jets were surveyed using a pitot-static pressure tube to measure hole-to-hole variation of velocity head. Initially, modifications were needed in order to achieve better flow uniformity between holes. The changes focused on delivery of the flow to the holes and not hole layout or size. The auxiliary turbulence generator flow, as described in Section 3.1.2.1, is delivered into a distribution plenum which surrounds the turbulence generator shown in Figure 13. Angled baffle plates are placed just inside the delivery hole to divert flow from passing directly into the cross flow jet holes. Without the baffle plates, much stronger cross flow jets would exist nearest the delivery hole. Instead, the flow is forced outward from the delivery hole along the casing wall and a more uniform pressure driven flow situation is created. After installing the baffle plates, a hole-to-hole velocity survey was again completed along all four walls. Jet velocities were found to vary ±2 m/s within their respective row. This amount of variation was considered acceptable. Using these measurements it was also determined that opposing rows of holes had similar jet velocities and integrated flow rates. This finding shows that energy is being injected into the mixing zone in a symmetric manor.

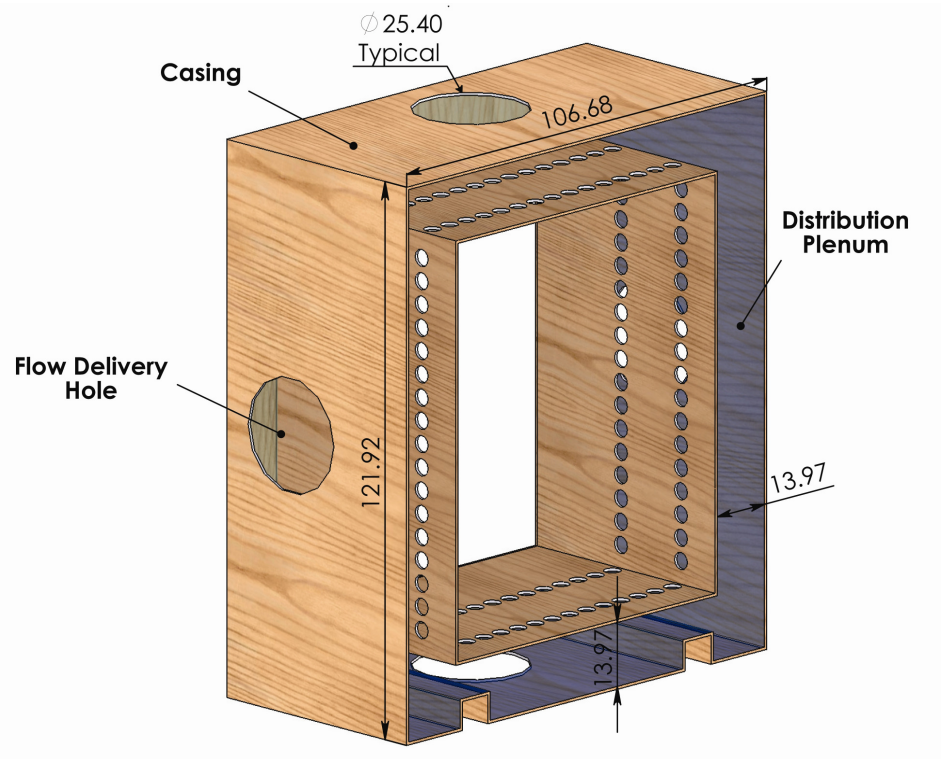

Figure 13. Casing of Turbulence Generator (Shown with Inside Walls)

3.1.4 Nozzle

Connected to the downstream side of the turbulence generator, the two-dimensional nozzle provides a flow area contraction between the wind tunnel and test section. This area reduction serves a second purpose in that it strains the flow resulting in a more uniform velocity distribution at the exit. The nozzle is made of 13 gage (2.3 mm/0.09 in. thickness) 304 stainless steel including its flanges. All four outside walls are rolled and welded along joints to conform to the designed contours. The area ratio is approximately 2.1:1 with inlet dimensions of 91.4 cm x 76.2 cm (36 in. x 30 in.) and outlet dimensions of 64.5 cm x 50.6 cm (25.4 in. x 19.9 in.) as seen in Figure 14. The total length in the streamwise direction is 60 cm (23.6 in.). Flanges having a width of 7.6 cm (3 in.) are used for connecting the nozzle to upstream and downstream components.

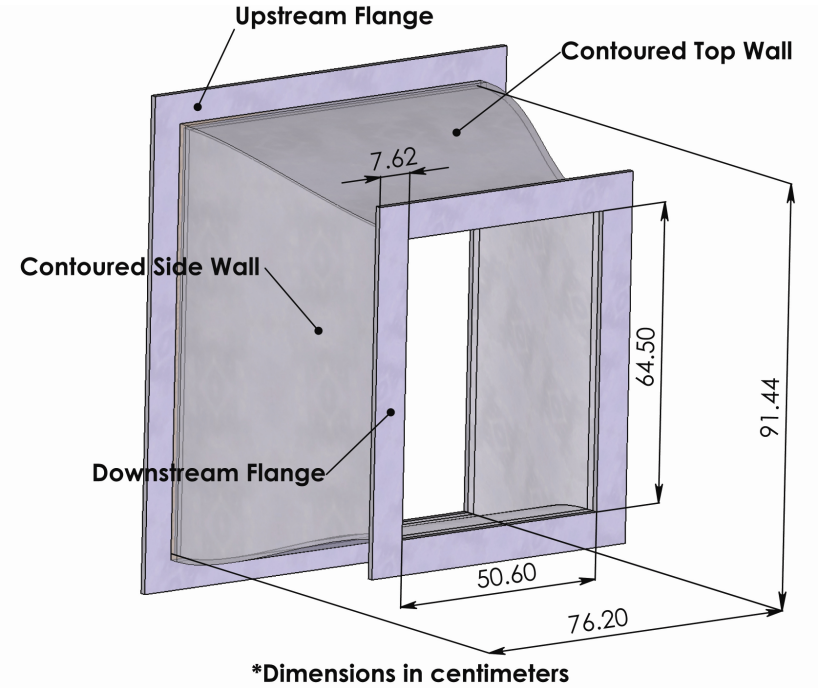

Figure 14. Contracting Nozzle Geometry

3.1.4.1 Contours of Top/Bottom and Side Walls

The nozzle walls are designed to incorporate concave and convex curvature. This design is not required as the flow is quite turbulent, however it is often used to ensure that flow streamlines are parallel to the walls at both the inlet and exit planes. To accomplish this wall contour, a numerical technique called a regression analysis is performed.

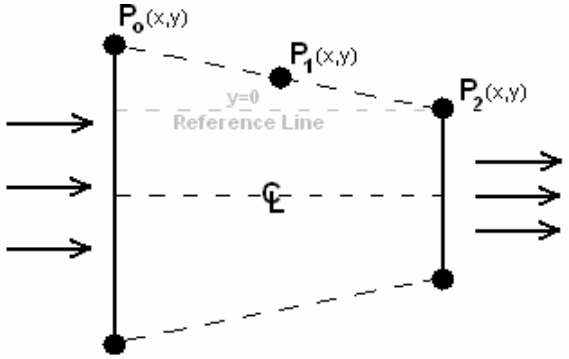

Figure 15. Sketch of Nozzle Wall Contour Problem

A cubic polynomial is used to mathematically describe the wall's contour and appropriate boundary conditions (coordinates in physical space) are defined that the function must satisfy. Each wall contour is split into two sections which span from points P_0 to P_1, and P_1 to P_2 as seen in Figure 15. The regression is carried out in a piecewise fashion with boundary conditions coupling the two regions. This problem is often referred to as a "Clamped Cubic Spline" which results from forcing certain characteristics at the nozzle wall endpoints (P_0, P_2). In this case, the endpoints are forced to have both first and second derivatives of zero so that streamlines would theoretically be parallel when both entering and exiting the nozzle. Matching conditions are utilized at the midpoint location (P_1) to ensure there are no discontinuities over the interval. A set of equations using this information are then solved simultaneously resulting in functions for the wall contours.

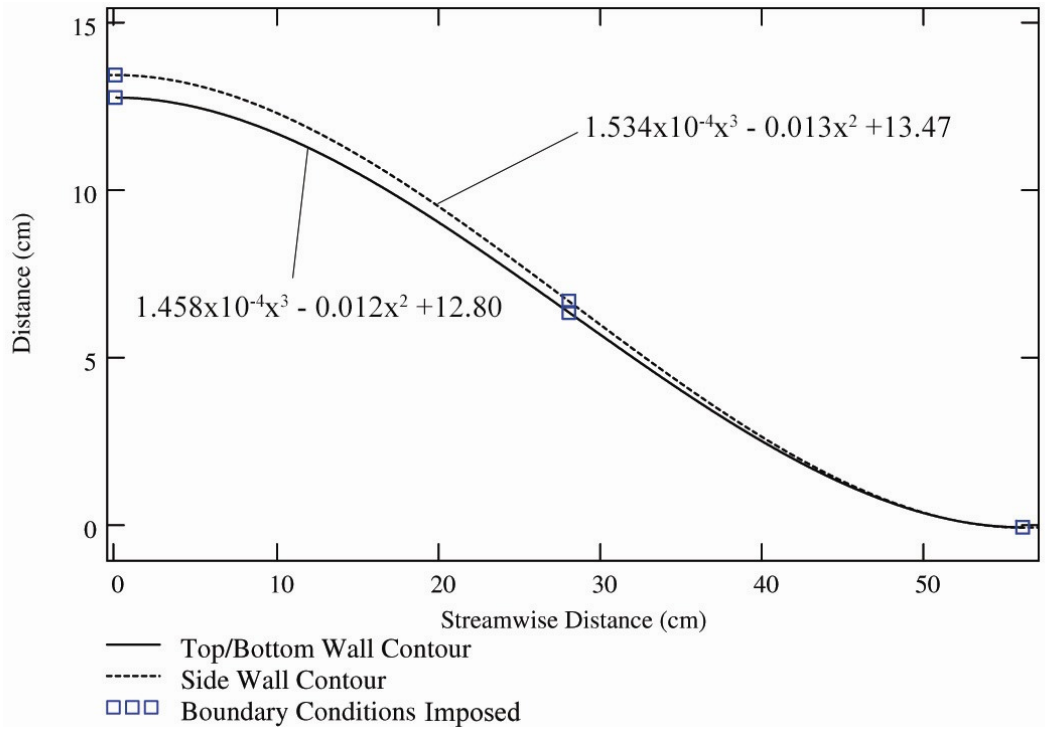

Figure 16. Nozzle Wall Contours

The results of the regression analysis are shown in Figure 16. Cubic polynomials are given for both wall contours for reference. These functions were utilized during the nozzle manufacturing process when rolling the walls.

3.2 Rotor Cascade Test Section

The test section is designed to simulate the geometry and flow inside an airfoil passage of a modern, mid-sized gas turbine engine. It is a two passage cascade which contains three rotor blades, two contoured endwall designs, a flat endwall, a leakage flow slot and plenum, and a temperature control slot for creation of a thermal boundary layer.

All components were designed with the help of SolidWorks CAD software to produce engineering drawings. These drawings, and in some cases the CAD files themselves, were used by machinists in the Mechanical Engineering Research Shop to make each test section component. Additional machining and test section assembly were performed in the Mechanical Engineering Student Shop and the Heat Transfer Laboratory, respectively. Documentation for the test section design is given in the form of CAD and PDF files which are available on the accompanying thesis DVD.

3.2.1 Rotor Blades

Three blades were constructed from medium-density fiberboard (MDF) for this study. This material is an engineered wood made of fibers, wax, and an adhesive binder under high pressure and temperature as described in Rowell [27]. It is chosen for its good machinability, relatively low cost, and low thermal conductivity ranging between 0.12-0.15 W/mK. Since MDF is commercially available in sheets, the airfoils were constructed by machining the cross-sectional profile into several sheets and stacking them to achieve the desired blade span. Figure 17 shows many of these blade "slices" loosely stacked on one another during the construction process. These blade slices were later bonded together, sanded, finished with a polyurethane sealer, and painted black. For additional clamping force, the blades are fitted with threaded rods passing through their span. Nuts on either side of the blade may be tightened manually to keep the blades under compression.

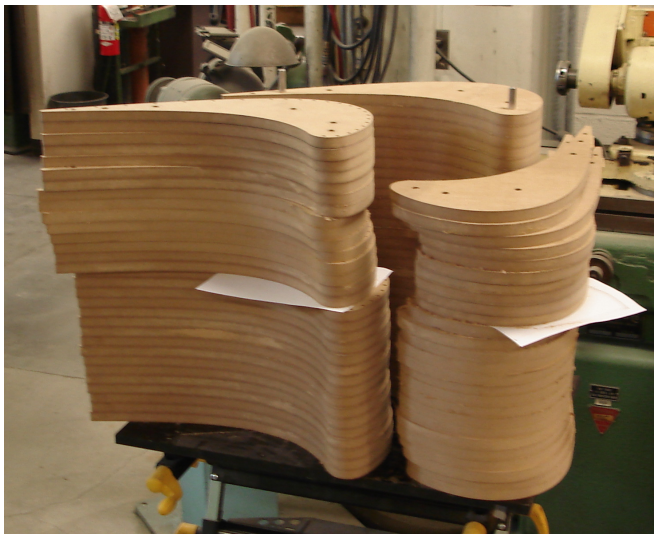

Figure 17. Rotor Blades During Construction

Static pressure taps are also included into the blade design as detailed in Section 3.2.1.2. To accommodate pressure taps, ports were drilled into the airfoils at the required locations as shown in Figure 18. These internal ports are 0.64 cm (1/4 in.) in diameter and pass approximately 3 mm (0.12 in.) below the blade's surface ending at the midspan. Stainless Steel tubing with a 4.7 mm (3/16 in.) I.D. is inserted into the ports and fixed with a Room Temperature Vulcanizing (RTV) silicone securing them in place. The tubing is cut so that it extends out of the ports approximately 2 cm (0.8 in.) for connection to Tygon plastic tubing.

The blade is structurally supported through the use of 1.3 cm (1/2 in.) diameter steel dowel pins inserted at the tip and hub. At the tip, two pins pass from the blade into holes in the flat endwall. Similarly, two pins are used at the blade's hub which connect to the test section's superstructure. In addition to the pins, the hub endwalls provide load support as they extend outward around the blade.

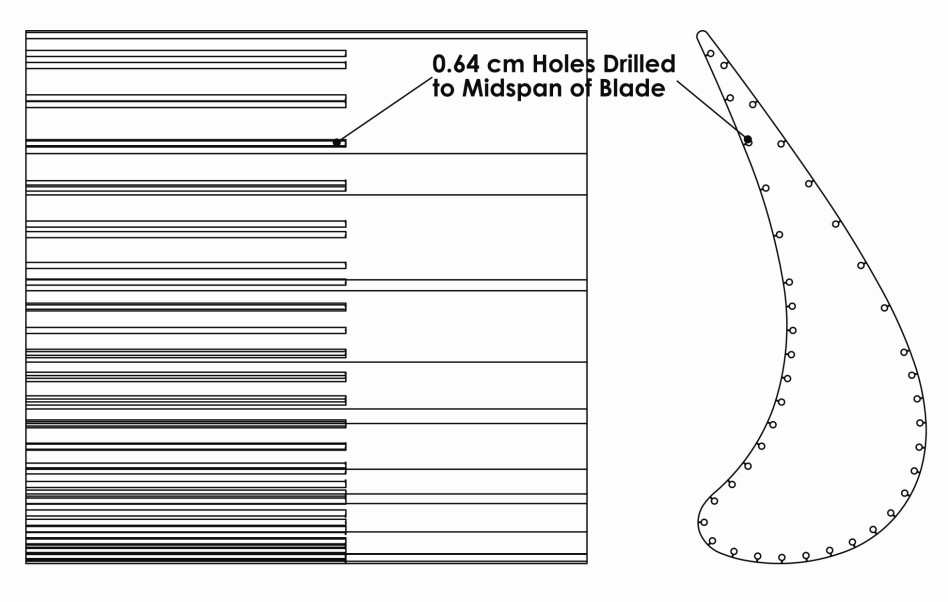

Figure 18. Blade Drawing Showing Internal Ports and Profile

3.2.1.1 Rotor Blade Profile and Cascade Layout

The rotor blade profile is obtained from a mid-sized modern industrial gas turbine. The two-dimensional blade profile used in this study is actually taken from a selected cross-section of a three-dimensional blade. A scaling factor of approximately 14x is used for these blades in reference to their size in the actual engine. When arranged in the cascade, the blades provide a flow turning angle of approximately 110º, and thus are highly loaded. Details of the cascade layout and other blade parameters are given in Figure 19 and Table 1.

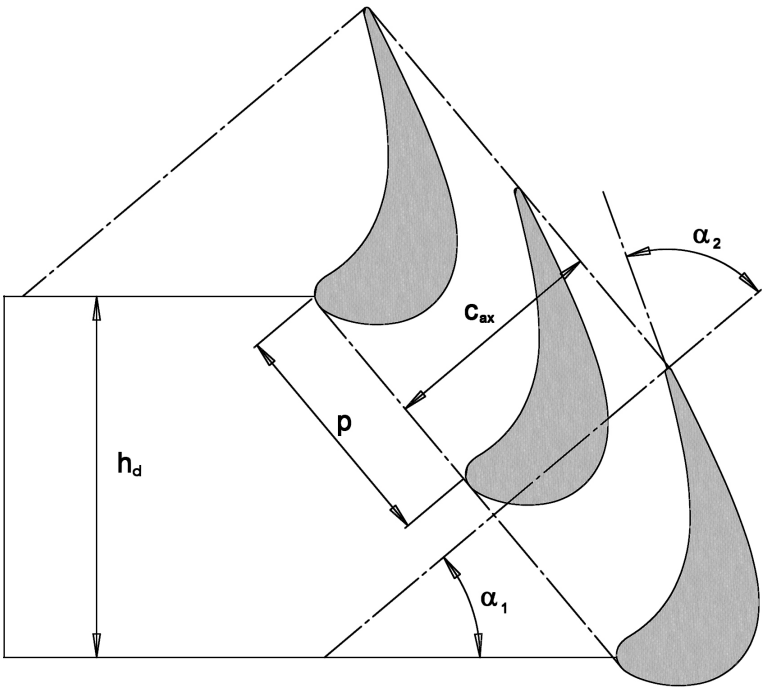

Figure 19. Cascade Layout

Table 1. Rotor Design Parameters

Scale Factor:	14.06
Chord Length (C):	55.79 cm
Axial Chord Length (C_{ax}):	43.20 cm
Pitch (p):	42.10 cm
Blade Aspect Ratio:	1.20
Inlet Flow Angle (α_1):	40.0°
Outlet Flow Angle (α_2):	70.0°
Inlet Duct Height (h_d):	64.50 cm

3.2.1.2 Blade Static Pressure Taps

Taps are available for measuring static pressure at the midspan of all three cascade blades. Each tap was drilled using a 0.5 mm (0.02 in.) diameter bit to an ℓ/D of approximately 6. A rotating table was used to orient the blade's surface perpendicular to the drill for each hole. All taps were then cleared with a needle and checked for smoothness at the blade surface. An effort was made to ensure that no burrs were present while still keeping holes square-edged. Recommendations from Shaw [28] and Goldstein

[29] were followed during this process to minimize errors which may be attributed to hole dimensions. A total of 40 pressure taps are drilled around the profile of the blade. The spacing between taps was adjusted based on the curvature of the surface, resulting in more taps being placed in highly accelerated (large pressure gradient) regions. Their locations are shown in Figure 20 as well as Table 2.

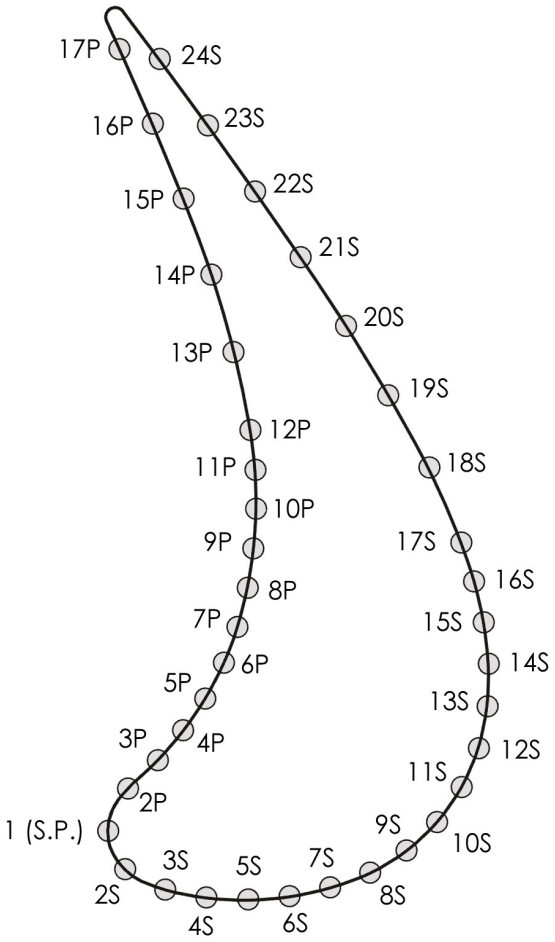

Figure 20. Static Pressure Tap Locations

Table 2. Static Pressure Tap Locations

Tap	x (cm)	x/C_{ax}
1 (S.P.)	0.000	0.000
2S	2.699	0.048
3S	5.548	0.099
4S	8.196	0.147
5S	10.820	0.194
6S	13.445	0.241
7S	16.071	0.288
8S	18.713	0.335
9S	21.384	0.383
10S	24.054	0.431
11S	26.726	0.479
12S	29.396	0.527
13S	32.055	0.575
14S	34.707	0.622
15S	37.318	0.669
16S	39.928	0.716
17S	42.519	0.762
18S	47.666	0.854
19S	52.785	0.946
20S	57.891	1.038
21S	62.993	1.129
22S	68.081	1.220
23S	73.169	1.312
24S	78.258	1.403
2P	3.015	-0.054
3P	5.565	-0.100
4P	8.031	-0.144
5P	10.497	-0.188
6P	12.965	-0.232
7P	15.421	-0.276
8P	17.902	-0.321
9P	20.384	-0.365
10P	22.865	-0.410
11P	25.347	-0.454
12P	27.827	-0.499
13P	32.859	-0.589
14P	37.888	-0.679
15P	42.930	-0.769
16P	47.996	-0.860
17P	53.062	-0.951

Each tap leads to its own individual port on the inside of the blade as described in Section 3.2.1. The port is then connected by plastic Tygon tubing to a two-way pneumatic valve (model TV-2S) made by Clippard Minimatics. A large switchboard of these valves was constructed using various fittings to patch them together into a common line. That line is then connected to a pressure transducer for monitoring as described in Section 4.3.2.

3.2.2 Endwalls

Of particular importance to this study are the endwalls. For the hub endwall, two different contoured shapes are available for use. The contouring for both takes place along the axial direction only. To differentiate between these two endwalls, they will be referred to hereafter as the "dolphin nose" and "shark nose" endwall shapes where necessary. Opposite the aforementioned contoured endwall at the blade's tip is a flat wall. This endwall is made of a 1.27 cm (1/2 in.) acrylic sheet. It serves a second role by providing access to the test section via its removable panels. This feature is described in Section 3.4.1. With respect to the actual engine, all radial curvature is removed from the endwalls as this test section is a linear cascade.

The contoured endwalls are machined from MDF sheets in a similar fashion to the airfoils. Initially the material is laid out with sheets stacked and bonded to one another as shown in Figure 21. A mill is then used to machine the appropriate contour into the material as well as cut the outside geometry. To facilitate easy handling and installation, each endwall is made in two pieces, or inserts. These inserts share an identical outside geometry to make them interchangeable inside the test section regardless of their axial contouring. An example of the insert geometry is shown in Figure 22. After machining is complete, a polyurethane sealer and several coats of paint are applied to finish the material.

Structural support for the endwalls is provided by fasteners on the backside of the endwalls. Each endwall insert has three fastening locations enabling 9.5 mm (3/8") bolts to be fed through the metal superstructure and into the endwalls. Access to the bolts is available on the back side of the test section to make the endwalls easily removable.

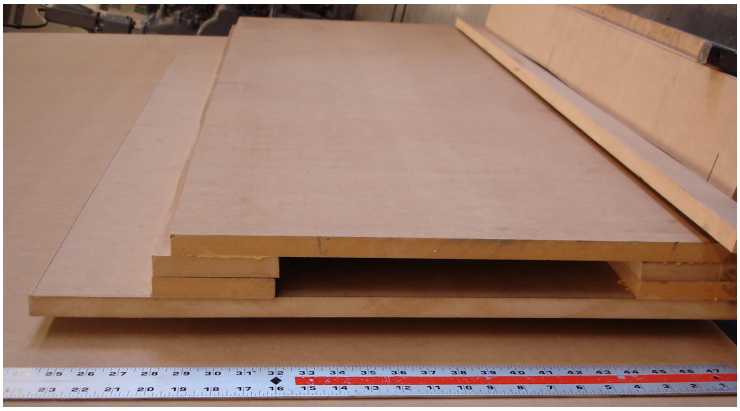

Figure 21. Endwall Shape During Construction

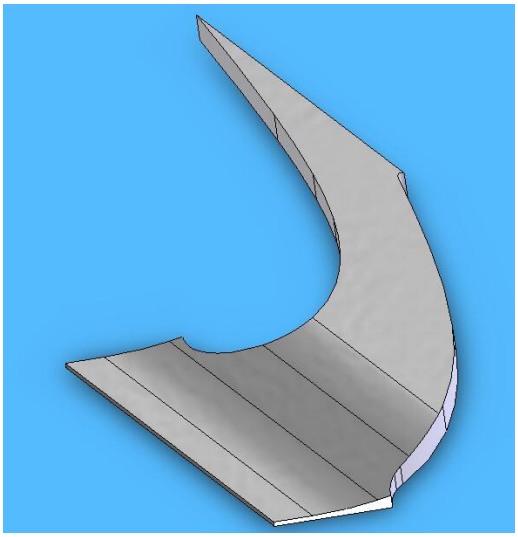

Figure 22. Example Endwall Insert Geometry

3.2.2.1 Shark Nose and Dolphin Nose Endwall Contours

As previously mentioned, two different contours are used for the hub endwall in this study. Both contours are taken from 2D engineering drawings provided by Solar Turbines, Inc. The drawings were digitized and scaled appropriately to arrive at their final design. While detailed dimensions of the endwall contours cannot be given, a visual comparison of the two profiles is offered in Figure 23.

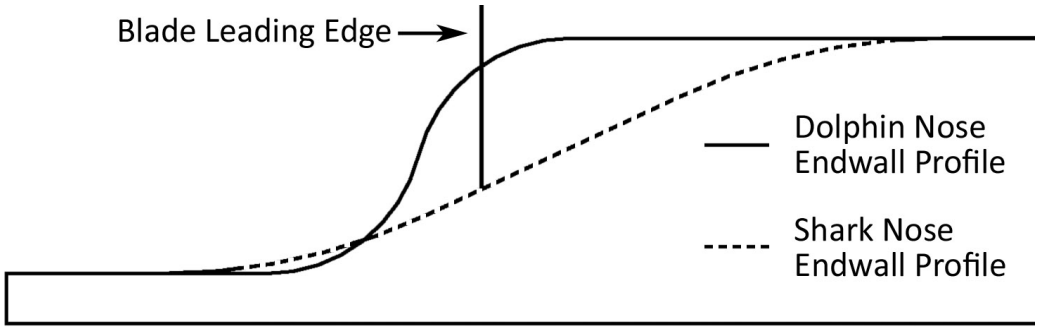

Figure 23. Comparison of Dolphin and Shark Nose Endwall Contours

The dolphin nose endwall contour displays very strong curvature beginning at an $x/C_{ax} = -0.14$. This concave section meets tangent to a convex curve extending to $x/C_{ax} = 0.06$, which is just past the blade's leading edge. In contrast, the shark nose contour is much more gradual, beginning at an $x/C_{ax} = -0.21$ and ending inside the passage at an $x/C_{ax} = 0.31$. Both contours are seen in Figure 23 relative to the blade leading edge as displayed by a solid vertical line. It should also be noted that both contours end at the same downstream elevation (right edge of Figure 23). This height is also in the same plane as the approach flow wall. Thus, no upward or downward step exists between the approach flow wall and hub endwall.

3.2.3 Leakage Flow

Leakage flow plays a very important role within a turbine by preventing hot gas path ingression into areas where it may cause damage. Specifically in this study, the leakage flow which passes through the stator/rotor interfacial gap is simulated. In the engine, a stator/rotor interfacial gap is necessary for the rotor is moving at very high rotational speeds immediately downstream of the stator. The problem of keeping a tight clearance between the stator and rotor is further complicated by thermal expansion due to transient thermal loads. Since tolerances of the interfacial gap are difficult to control, and fluid from the main gas path entering this area would damage the engine, a "leakage flow" is bled from the compressor and is exhausted through the stator/rotor interfacial gap within the turbine.

The leakage flow for this test section is delivered as described in Section 3.1.2.3. From the large turning header, the flow enters into a large acrylic box which will be referred to as the "leakage plenum." This plenum was designed to simulate the disc cavity components through which leakage air flows in a real engine. After traveling through the plenum, the leakage flow enters into the main wind tunnel by means of the leakage flow slot. This slot is situated immediately upstream of the hub endwall and represents the stator/rotor interfacial gap of an engine.

Of particular importance to this study is the amount of leakage flow entering the plenum. As mentioned previously, the leakage flow is metered during operation and can be adjusted appropriately. The chosen flow rates used in this study are scaled on the total wind tunnel flow approaching the leakage slot using a mass flow ratio (MFR). Using this scaling parameter, the leakage flowrates have a MFR of 0.5%, 1.0%, and 1.5%.

3.2.3.1 Leakage Plenum Geometry

In an attempt to more accurately simulate how leakage flow enters the rotor passage, various dimensions and length scales were taken from a modern gas turbine engine drawing. These dimensions were scaled appropriately and used to design the leakage plenum as seen in Figure 24 and documented in Table 3.

Table 3. Leakage Plenum Dimensions

Leakage Plenum Dimensions	
Stator Endwall Lip (h_s):	2.14 cm
Rotor Endwall Lip (h_r):	2.85 cm
Rim Seal Gap (h_i):	0.50 cm
Plenum Height (h_p):	28.80 cm
Plenum Width (w_p):	21.60 cm
Chamfer Angles (β):	15.0°

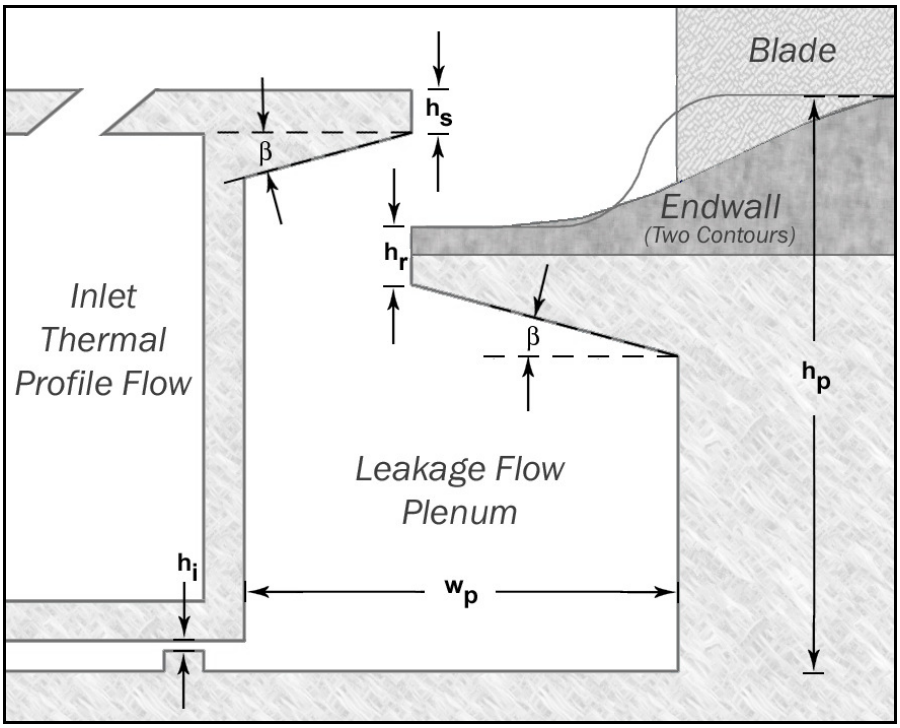

Figure 24. Leakage Plenum Dimensions

With regard to Figure 24, several things should be noted for the reader's reference. The main flow enters the figure from the top left corner moving rightward. Similarly, the leakage flow moves from left to right entering the channel in the bottom left corner of the figure. As the leakage flow travels through the channel, it is abruptly met with a reduced area. This contraction is designed to simulate a rim (labyrinth) seal in the engine where local fluid velocities become very high. Past the rim seal, the leakage flow enters into a large open volume where it mixes and is directed upward. It then travels through the leakage flow slot and onto the contoured hub endwall. Shown in this figure is the shark nose endwall contour (shaded) and the dolphin nose endwall contour (single line).

3.2.4 Approach Flow Temperature Control Slot

Upstream of the passage ($x/C = -0.641$) an open slot running the length of the wind tunnel's sidewall is used to inject additional fluid into the main flow. The delivery of this flow is discussed in Section 3.1.2.2. As the fluid travels into the plenum and out the 45º slot it mixes with near-wall fluid of the main flow. By controlling the temperature and

flowrate of the fluid, different temperature gradients may be created. Thus, there is some flexibility in this setup although it is strictly limited to affecting near-wall flow. For this particular application this method is adequate since temperature profiles have been shown to be fairly flat through most of the spanwise direction.

Documentation of the approach flow temperature gradient is given in Section 6.2.3.

3.3 Wind Tunnel Exit Flow

The two components that aid in managing the wind tunnel's exit flow are the tailboards and diffuser. They are important in order to properly adjust the amount of flow traveling through each of the cascade's two passages, as well as more efficiently exhaust the wind tunnel exit flow into the room. Each component is described in more detail in the following sections.

3.3.1 Tailboards

The presence of elliptic behavior in a linear cascade causes exit flow conditions to affect inlet conditions. For this reason, careful consideration must be taken into account when dealing with downstream boundary conditions such as wall placement. For this test section, the tailboards are connected to the airfoils at the exit plane of the passage and are designed for easy adjustment to overcome wall sensitivity. They are made of a 0.16 cm (1/16 in) thick polycarbonate sheets and fitted with several full-width acrylic ribs for added stiffness. The ribs are made to accept C-clamps at their ends which hold the tailboards snug to the diffuser's side walls. The polycarbonate material bends in between these fixed points to smoothen out the curvature of the wall.

The final tailboard position is determined by taking static pressure measurements along the midspan of all three blades. As previously mentioned, the blades are fitted with pressure taps which are used to measure local static pressure values. Once pressure profiles on all three blades are measured, their relative values are analyzed. Adjustments to the tailboards are made to either increase or decrease the exit area of a passage depending upon the data. The end goal is to introduce an equal amount of fluid (flowrate) into the two passages.

3.3.2 Diffuser

While traveling through the cascade passage, the working fluid is strongly accelerated and exits with a static pressure that is lower than the room's ambient pressure. To efficiently exhaust this flow into the room, a diffuser is used to recover some of the static pressure. Simply stated, by slowing down the exit flow in a diffuser a higher flowrate can be achieved as compared to a test section that would directly exhaust into the room.

The front and back walls of the diffuser are made of 1.27 cm (0.5 in) thick acrylic sheets with a length of 122 cm (48 in) and width of 50.8 cm (20 in). Both sidewalls are made from 1.9 cm (3/4 in) thick plywood with a polyurethane finish to decrease roughness. An optimum geometry for the diffuser was designed based on recommendations by Sovran and Klomp [30]. The resulting diffuser has an area ratio of 2.1, divergence half-angle of 7º, and streamwise length of 122 cm (48 in). Based on the referenced data, the pressure recovery coefficient (based on mass-averaged quantities) for this design is approximately 0.63. Through further review of diffusers in highly turbulent flow as in Hoffman [31], it was concluded that this divergence angle is adequate and possibly on the conservative side. This is because turbulent flow contains more momentum near the wall versus a comparable laminar flow. Thus, separation due to adverse pressure gradients is delayed.

It is worth noting for future work that the diffuser's pressure recovery could be increased by either adding length or designing a multi-vaned diffuser. Since the length of the diffuser is restricted by ceiling height for this case, the first option is not possible. The second option, however, is viable and would have been incorporated. Through a few simple calculations utilizing experimental data from Sovran and Klomp, one could design a diffuser with the same streamwise length and three passages (two vanes) giving a pressure recovery coefficient of 0.76. This would result from a diffuser with an area ratio of 3.0 and divergence half-angle of 4.5º. For this reason, a multi-vaned diffuser is recommended for future designs as it could be incorporated with relative ease.

3.4 Test Section Measurement Access and Traversing System

To facilitate measurements and adjustments within the cascade, the test section was designed with removable panels on the flat endwall. In conjunction, a movable hole panel is used to support measurement probes and provide access to important locations. Outside of the test section a three-axis automated traversing system is used to control movement of the measurement probe. These components, along with the appropriate computer control commands, allow for measurement access within the linear cascade test section.

3.4.1 Flat Endwall Panels

The flat endwall is made of acrylic and has several components as seen in Figure 25. The front cover is the largest piece and provides structural support through several legs that rest on the table, and also from connections to the nozzle flange. Several through-holes are drilled into the front face which allow dowel pins to be inserted into the three blades. These connections assist in supporting the weight of the blades as well as provide rigidity when they are fully loaded.

The removable panels are designed to overlap each other and lock into place by using small latches. These panels can be arranged in a number of configurations enabling translation of the movable hole panel. Where necessary, through-holes are drilled into the panels just as described for the front cover.

3.4.2 Movable Hole Panel

The movable hole panel facilitates probe movement within the passage. As seen in Figure 26, it is comprised of inner and outer disks which rotate relative to each other via ball bearings along their perimeter. At the edge of the inner disk, a small probe holder is mounted which accepts up to a 6.4 mm (1/4 in) probe diameter. With this design, the movable hole may be moved to any location within the outer disk. For more details see Piggush [32].

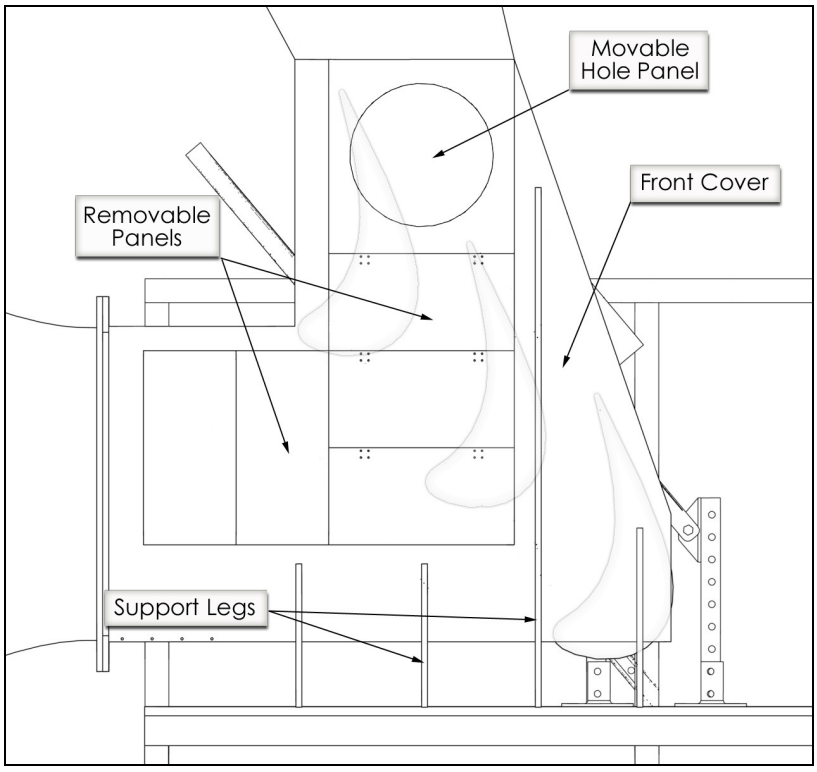

Figure 25. Flat Endwall Components

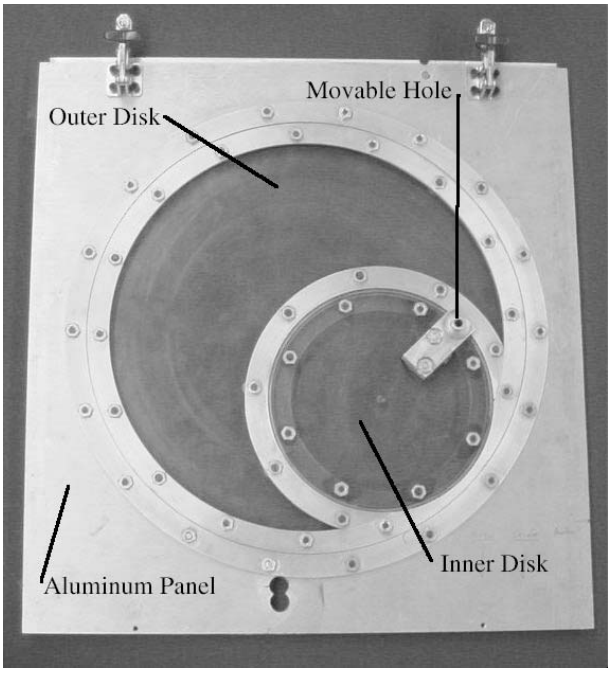

Figure 26. Movable Hole Panel (Taken from Piggush [32])

3.4.3 Automated Traversing System

The automated traversing system is used to control the probe's position within the test section. It is configured for movement along three axes in conjunction with the movable hole panel as seen in Figure 27. The traverse system is mounted onto a variable-height table which allows coarse adjustments to be made for different setups.

At the base of the system is a Velmex UniSlide® model MB4024K1J-S6 which controls movement in the spanwise direction. This unit is driven by a stepper motor having 1.8º rotation per step (200 steps per revolution) and lead screw with a travel of 45.7 cm (18 in). Mounted onto the base unit in a perpendicular orientation are two identical MB2515K1J-S3 Velmex UniSlides. These units are also motor driven with 1.8º rotation per step (200 steps per revolution) and 30.5 cm (12 in) of travel. For more detailed information and specifications of the UniSlides refer to Velmex [33].

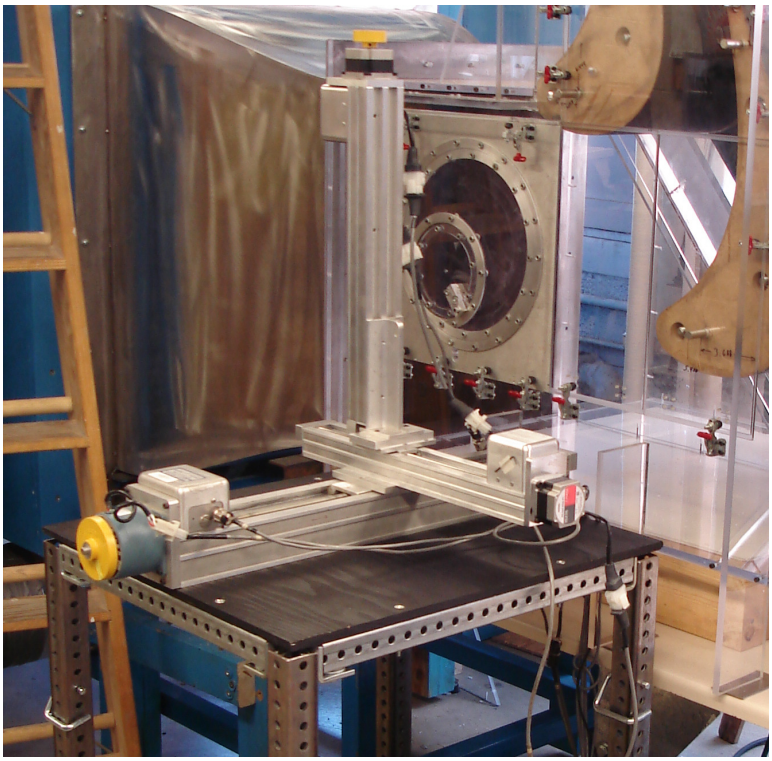

Figure 27. 3-Axis Automated Traverse System

® UniSlide is a Registered Trademark of Velmex, Inc.

To control the three stepper motors, an NF90 Series Stepping Motor Controller made by Velmex, Inc. is used. This hardware is interfaced to a personal computer using an IOtech Serial 488A Bus Converter, IEEE 488.2 (GPIB) cable, and National Instruments PCI-GPIB card. The system allows control and status commands to be sent back and forth between a personal computer and the Stepping Motor Controller. All programs which perform such commands are written using the C++ programming language in this study.

As can be imagined, many different probe movement paths are required. For this reason, a C++ program called *ME DAQ* was written and used for all measurement types and locations. This program as well as its source code may be found on the accompanying thesis DVD.

Chapter 4

General Measurement Techniques

This chapter contains information on the measurements techniques employed in the study. Included are general descriptions, measurement theory, references, and calibration procedures and results.

4.1 Velocity Measurements

Accurate velocity measurements are of fundamental importance to this study. In this section, an overview of the thermal anemometry and Pitot-static tube measurement techniques is given.

4.1.1 Thermal Anemometry

Thermal anemometry is a technique by which a fluid's velocity is indirectly measured as it passes over a heated sensor. With an understanding of the fundamental convective heat transfer problem of a heated cylinder in a cross flow, the relationship between velocity and the sensor's cooling rate can be described. This correlation assumes that other parameters important to the underlying heat transfer problem (i.e. density, viscosity, sensor temperature, and freestream temperature, etc.) are held constant.

In this study, an AN-1005 anemometer (AA Lab Systems, LTD) is used in Constant Temperature Anemometry (CTA) mode as a means of deducing velocities. The CTA method operates using a control circuit (Wheatstone Bridge) which continually maintains a constant sensor resistance (proportional to temperature). To do so, the anemometer bridge modifies the voltage across the probe delivering more or less power as needed. By means of a simple energy balance, it is seen that the power delivered to the sensor for heating purposes equals the sensor's cooling rate. Assuming that all parameters except voltage and velocity remain constant, King [34] derived an expression which may be written in a more generalized form as in (Eq. 4.1). This relationship is used when calibrating hotwire sensors and shows good agreement with measurement data.

$$E^2 = A + B \cdot U_e^{\,n} \qquad \text{(Eq. 4.1)}$$

where

E = Voltage
A,B = Calibration Constants
U_e = Effective Cooling Velocity
n = Constant (Typ. 0.43-0.45, King = 0.5)

Two different hotwire sensor models made by TSI, Inc. are used in this study. The first is referred to as a "boundary layer probe" (TSI model 1218-1.5) due to its curvature allowing for near-wall placement. This probe is shown in Figure 28 (Top). The second is a general purpose straight probe (TSI model 1210-1.5). Calibration and measurement procedures are identical for the two probe models and thus are not differentiated in the following sections. For more information on hotwire probes refer to TSI, Inc. [35].

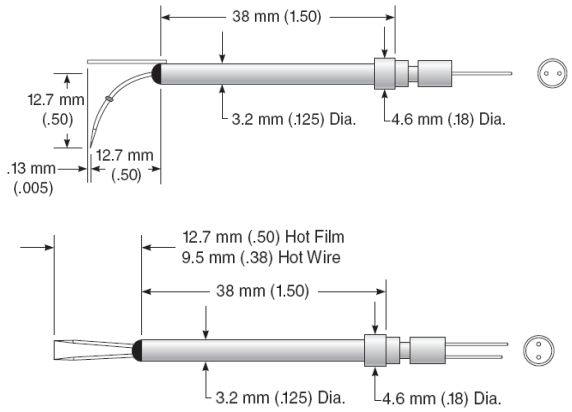

Figure 28. Boundary Layer (Bottom) and General Purpose (Top) Hotwire Probes from TSI, Inc.[35]

4.1.1.1 Hot Wire Sensor Calibration Procedure

The hotwire calibration procedure is completed using a orifice meter type device originally designed by Wilson [36] and shown in Figure 29 (taken from Adolphson [37]). The apparatus produces a steady, low turbulence jet using a baffle, flow straighteners, fine screens, and elliptical nozzles. Just upstream of the calibration jet is a compressed air hose connection and two needle valves for flow throttling. The device is suitable for measuring a wide range of velocities as hotwire sensors may be placed either in the inner

chamber or at the exit of the metering nozzle. For this study, all calibrations were performed with the hotwire sensor mounted at the metering nozzle's exit. Other equipment used during the calibration procedure includes a U-Tube manometer (See Section 4.3.1.1), Resistance Temperature Detector (RTD), and voltmeter.

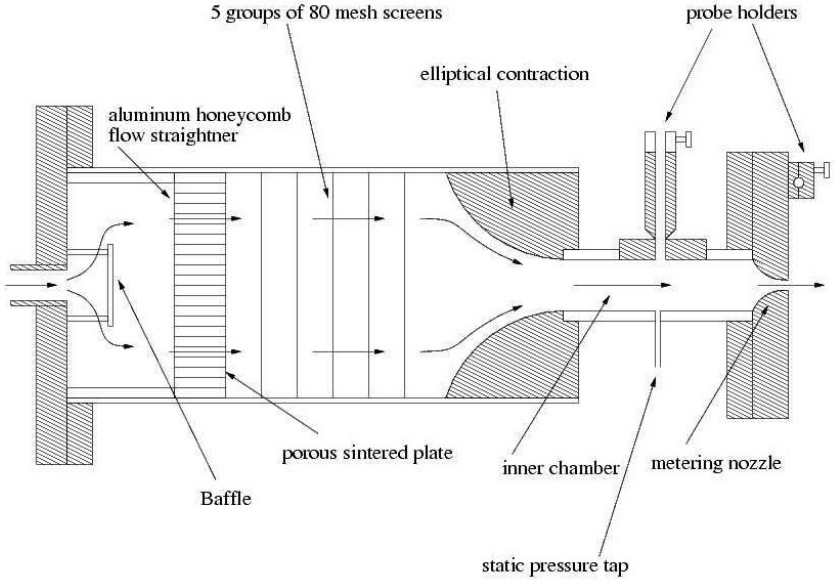

Figure 29. Calibration Jet Facility. Taken from Adolphson[37]

The general calibration procedure begins by configuring the anemometer channel to be used. This is done as explained in the AN-1005 user's manual and includes operations such as compensating for lead wire and probe holder resistance. At this time it is important to tune the anemometer's pulse frequency response by placing the hotwire sensor in a characteristic flow to be measured. This process assures that the anemometer's circuitry will not modify velocity fluctuations due to under/over damped response. An oscilloscope is used to view the anemometer's signal in real-time and the channel's damping trimpot is adjusted until a satisfactory pulse response is achieved. A sample pulse response from this study is shown in Figure 30. For more information consult the AN-1005 user's manual.

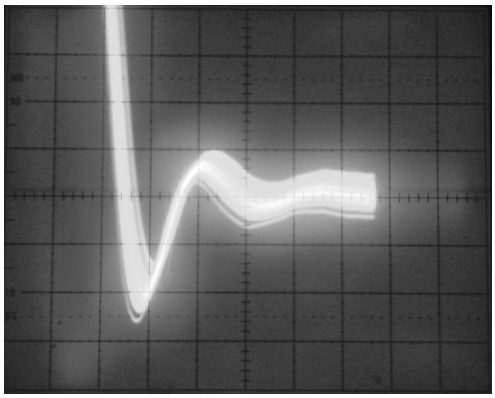

Figure 30. Sample Anemometer Pulse Frequency Response

Once the anemometer channel is configured, the compressed air supply, U-Tube manometer, and RTD are attached to the calibration jet facility. To measure resistance the four-wire RTD cables are then connected to the voltmeter, followed by the anemometer output to the data acquisition system using an IEEE 488 cable. This setup allows for the simultaneous measurement of voltage, pressure, and temperature from the anemometer, manometer, and voltmeter, respectively.

With the hotwire sensor mounted to the calibration jet apparatus, the needle valves are opened and adjusted to the chosen $\Delta P = P_{chamber} - P_{ambient}$ values as read by the manometer. At each ΔP value, the RTD resistance is recorded manually and the anemometer voltage is sampled using data acquisition software. This process is repeated in a random order over a range of ΔP values. Finally, the ambient pressure and relative humidity are recorded for reference.

4.1.1.2 Hot Wire Calibration Results

Results from a typical hotwire calibration are given in Figure 31 as $U_e^{\,n} = f(E^2)$. This form is suggested by (Eq. 4.1) and a linear least squares fit is utilized to find the appropriate calibration constants.

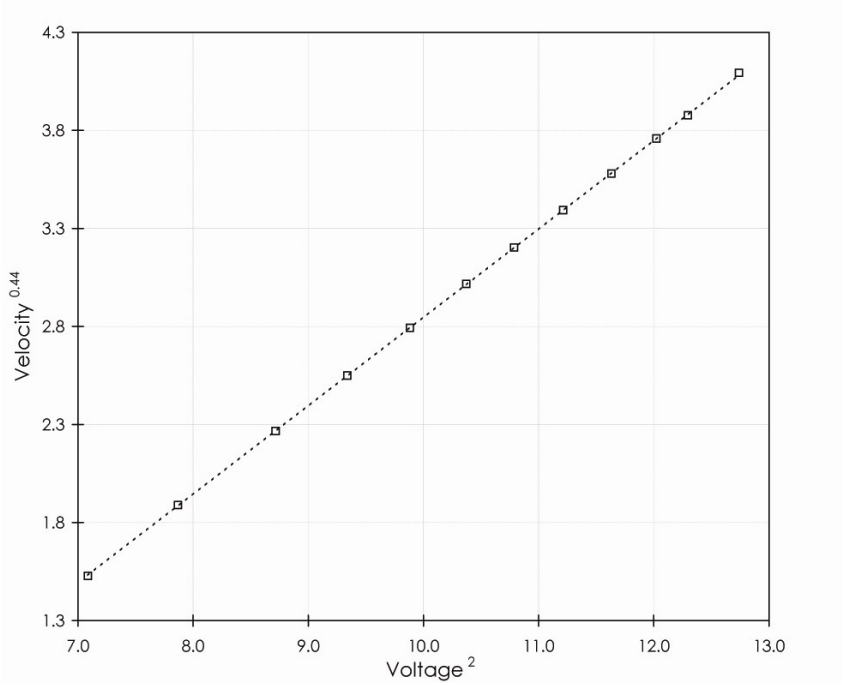

Figure 31. Typical Hotwire Calibration Data

Since the best value of the velocity coefficient n is not well defined, an optimization is carried out. Least squares fits are performed using several velocity coefficient values in the range of $0.43 \le n \le 0.45$. It is then possible to compare curve fit predictions to each measured data point. Curve fits are evaluated based on their deviation from measured velocity values and the optimal fit is chosen.

As an example, the linear least squares fit performed on the data in Figure 31 resulted in the function $U_e^{0.44} = -1.6686 + 0.4516 \cdot E^2$. The mean fit error was $Err_{fit\_mean} \approx 0.25\%$ with a standard deviation of $Err_{fit\_stddev} \approx 0.21\%$.

It should be noted that sources of uncertainty other than calibration error do exist. Due to a hotwire's relative insensitivity to flow direction, cross stream components of velocity can lead to significant uncertainty. With these considerations, a total uncertainty of 5% is suggested by Oke [23] over the utilized velocity range.

4.1.1.3 Qualification of Hot Wire Measurements

After calibration it is important to qualify hotwire measurements by comparing them against accepted data. For this study, velocity measurements are taken in a fully-developed pipe flow and compared with data from Laufer [38]. The pipe flow facility used has an I.D. of 5.08 cm (2") with an ℓ/D of approximately 75 ensuring fully-developed flow. The maximum velocity achieved in the pipe is 13.9 m/s which results in a Re_D of approximately 44,200. This Reynolds Number is slightly lower than that achieved by Laufer (Re_D = 50,000); however, the two flows are still considered to be comparable. The reported data and and Laufer's data are scaled and normalized for comparison. The agreement is generally good.

The velocity profile as shown in Figure 32 is normalized on the pipe centerline velocity U_o with the wall located at $r'/a = 0$ and the centerline at $r'/a = 1$. As a result of comparing these data sets, it can be said that the velocity measurements taken with the hotwire sensor are acceptable in terms of relative magnitude. It should be noted that velocities are not measured at $r'/a = 0$ in either data set. Instead, this point is assumed from the no slip boundary condition.

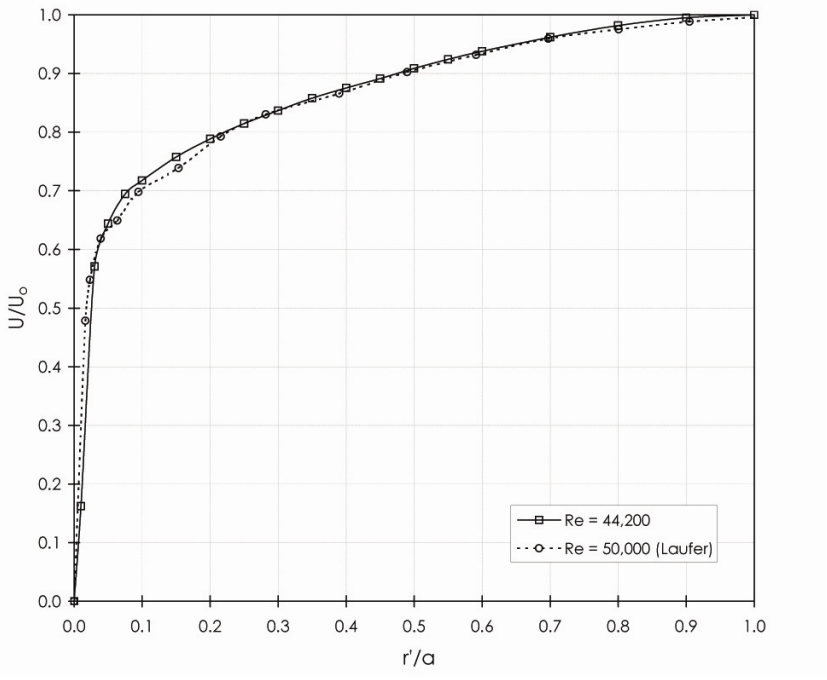

Figure 32. Normalized Velocity Distribution in Fully-Developed Pipe Flow

Measurements of velocity fluctuations due to turbulence are also compared to Laufer's data. For all readings, hotwire voltages are taken at a rate of 1 kHz for a period of 30 seconds. The velocity fluctuations, $u(t) = U(t) - \overline{U}$, are quantified by taking the root mean square ($\sqrt{\overline{u(t)^2}}$) of the signal. That magnitude, which will be referred to as u', has units of velocity and is scaled upon the shear (or friction) velocity U_τ (Eq. 4.2) and plotted in Figure 33.

$$U_\tau^{\,2} \equiv -\nu\left(\frac{dU}{dr}\right)_{r=a} \qquad \text{(Eq. 4.2)}$$

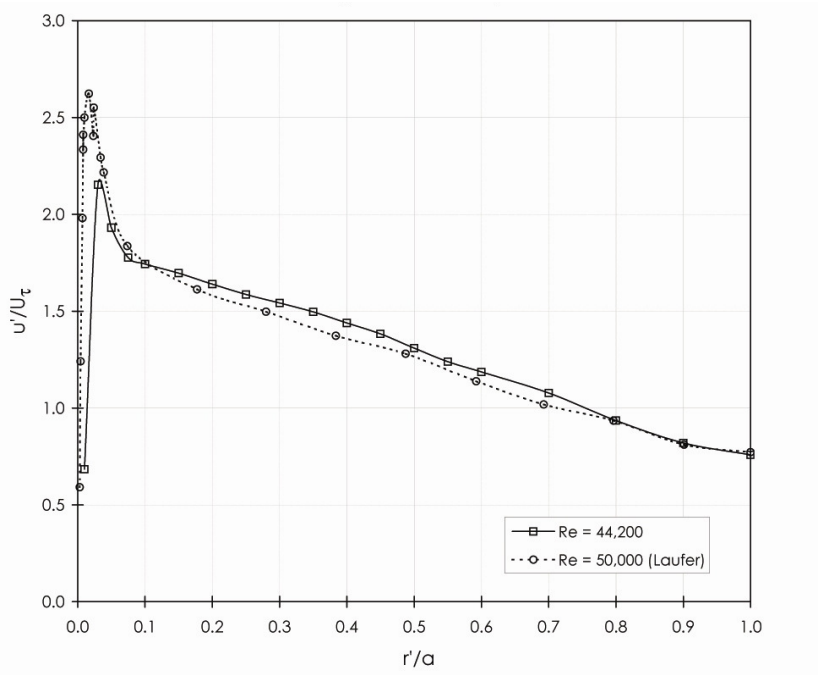

Figure 33. RMS of Turbulent Fluctuations in Fully-Developed Pipe Flow

It is observed that near-wall measurements of u'/U_τ are not in agreement with Laufer's data. A plausible argument may lie in the fact that Laufer's pipe was roughly 5 times larger in diameter than the one used in these measurements. As a result, the hotwire sensor takes up a significantly larger portion of the near-wall flow and may be measuring a lower DC component of the velocity fluctuations in that region. Additionally, near-wall spatial resolution becomes more important when using a smaller

pipe. With the current setup and scale it is not possible to reliably resolve the area between the first two near-wall readings. In the pipe's remaining exit area ($r'/a > 0.05$) the maximum difference in values is around 5%.

4.1.2 Pitot-Static Tube

In certain cases, velocity measurements using a Pitot-static probe are more convenient than by means of thermal anemometry. This method allows mean velocities to be deduced from pressure measurements under appropriate conditions. Details regarding pressure measurement devices are more completely covered in Section 4.3.

Ideal conditions for applying a Pitot-static probe occur when the flow may be assumed incompressible with negligible viscous effects. In this study, all velocities are observed to be in the Mach number range of $M \leq 0.12$ where compressibility effects can safely be assumed negligible. Similarly, viscous effects only appear to be significant when $\mathrm{Re}_D \leq 60$ based on the Pitot-static tube diameter according to Crowe et al. [39]. Using nominal approach flow velocities in this wind tunnel, a Pitot-static tube Reynolds number of $\mathrm{Re}_D \approx 1200$ is calculated. Since the flow satisfies these assumptions, both the Bernoulli equation and ideal gas law may be applied to understand Pitot-static tube measurements. Finally, a time-averaged local velocity $\overline{U}$ may be described by:

$$\overline{U} = \sqrt{\frac{2(\overline{P}_t - \overline{P}_s)}{\rho}} = \sqrt{\frac{2(\overline{P}_t - \overline{P}_s)RT}{\overline{P}_s\langle abs\rangle}} \qquad \text{(Eq. 4.3)}$$

where

$\overline{U}$	=	Velocity	$\overline{P}_t$	=	Total Pressure
$\overline{P}_s$	=	Static Pressure	ρ	=	Density
R	=	Gas Constant (Air)	T	=	Absolute Temperature
$\overline{P}_s\langle abs\rangle$	=	Absolute Static Pressure			

4.2 Turbulence Measurements

With the understanding that turbulence plays a significant role in both momentum and heat transfer, it is important to be able to characterize it. This is traditionally done by (1) measuring temporal fluctuations in velocity using a high sampling frequency to deduce spatial fluctuations (Taylor's frozen flow hypothesis), or (2) taking velocity readings separated in space at the same time and correlating the signals. For this study, only one-dimensional (longitudinal) velocity signals are analyzed making the first method most preferred. By analyzing velocity fluctuations over time, characteristics of the turbulent flow may be computed. These quantities include turbulence intensity (Tu), integral length scale (Λ), energy length scale (Lu), Taylor microscale (λ), and dissipation rate (ε).

4.2.1 Standard Deviation u' and Turbulence Intensity Tu

One means by which turbulent motion is often characterized was already alluded to in Section 4.1.1.3 by way of the RMS of velocity fluctuations. Formally defined in (Eq. 4.4), u' represents a magnitude (or intensity) of the velocity fluctuations at a specific spatial location. It is analogous to the standard deviation of $u(t)$ since $\overline{u(t)} = 0$ by definition. It is also worth noting that the sampling period of the velocity signal must be long enough so that u' is a repeatable quantity; otherwise it has no value.

$$u' = \sqrt{\overline{\left(U(t) - \overline{U}\right)^2}} = \sqrt{\overline{u(t)^2}} \qquad \text{(Eq. 4.4)}$$

Similar in nature to u', a relative, or more commonly used "turbulence intensity" may be defined as:

$$Tu = \frac{\sqrt{\overline{u(t)^2}}}{\frac{1}{N}\int_0^N U(t)dt} = \frac{u'}{\overline{U}} \qquad \text{(Eq. 4.5)}$$

These terms will be used later to quantify the level, or intensity, of turbulent motion within various flows.

4.2.2 The Energy Density Spectrum and Energy Spectral Distribution

While convenient to calculate, it is easy to imagine that Tu is not always sufficiently descriptive for a flow. When desired, it is possible to explore turbulent motion to a further extent by examining its distribution of kinetic energy over a broad range of fluctuation frequencies. These frequencies can then be related to length scales of turbulence (sizes of turbulent patterns) as they pass by the measurement device (Taylor's frozen flow hypothesis). This process gives rise to a velocity signal's Energy Density Spectrum (EDS) and its relative, the Energy Spectral Distribution (ESD).

The first step in obtaining an EDS is acquiring the velocity signal using a hotwire anemometer and data acquisition hardware/software. It is important to choose a sampling frequency that captures the smallest eddy scales of interest, low-pass filter the signal (satisfying the Nyquist criterion) to avoid aliasing, and sample for a long enough period that sufficient large scale data are obtained. Once a satisfactory velocity record has been obtained, the remaining work involves only signal processing. For these steps, mathematical software such as Mathcad, Matlab, or Mathematica is particularly useful.

The signal processing begins by converting the instantaneous velocity signal $U(t)$ into fluctuations about its time average ($u(t) = U(t) - \overline{U}$). This new signal $u(t)$ has a mean of zero and is comprised of both positive and negative values. A sample signal is shown in Figure 34.

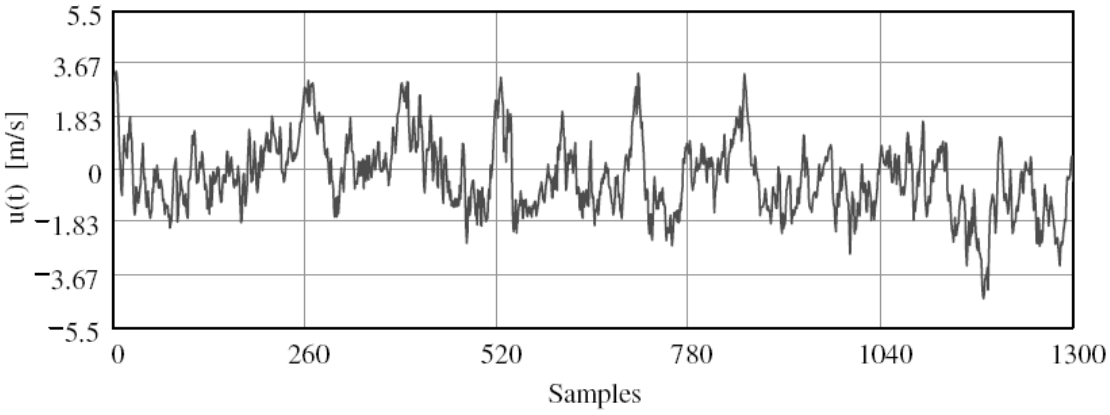

Figure 34. Sample Signal of Velocity Fluctuations about Mean ($u(t)$)

It is now necessary to transform the continuous velocity signal from the time domain to the frequency domain using a Fourier transform. For this study, a "canned" FFT function based on the Cooley-Tukey Fast Fourier Transform (FFT) algorithm is used. This version of the algorithm divides the total Discrete Fourier Transform (DFT) into two smaller DFT's to improve computational performance. The jth element of the DFT is given as (Eq. 4.6). It is important to understand what FFT algorithm is being used in a commercial software as various algorithms use different normalizing constants ($1/\sqrt{N}$ in (Eq. 4.6)). This function is shown in its discrete form as we are dealing with an array of data.

$$\Phi_j = \frac{1}{\sqrt{N}} \sum_k u(t)_k \, e^{i \cdot \left(\frac{2\pi \cdot j}{N}\right) \cdot k} \qquad \text{(Eq. 4.6)}$$

where

Φ	=	Transformed array from FFT	$u(t)$	=	Velocity fluctuations about mean
N	=	Sample size of $u(t)$	k	=	Index of $u(t)$ array (k=1..N)
j	=	Index of Φ array (j=1..N/2)			

The index j of Φ_j is actually related to frequencies found in the $u(t)$ signal. This relationship is given by (Eq. 4.7).

$$\omega_j = \omega_s \frac{j}{N} \qquad \text{(Eq. 4.7)}$$

where

ω_j = Array of actual frequencies

ω_s = Sampling frequency

What has now been created are two corresponding arrays of equal length, namely Φ_j (units of velocity) and ω_j. Several inherent properties of this transformation process are worth discussion. First, the bandwidth of the $\Phi(\omega)$ spectrum is directly determined by the sampling frequency ω_s. This is built into the mathematics of the FFT algorithm so that the maximum frequency of $\Phi(\omega)$ is $\omega_s/2$. Secondly, the resolution in the

frequency domain ($\Delta\omega$) is related to the total number of samples recorded by $\Delta\omega = \frac{\omega_s}{N}$. Thirdly, each Φ_j element is actually a complex number. The real part of this number represents an amplitude and the imaginary part represents a phase relative to the start of the $u(t)$ signal. Both of these components are used to construct an Energy Density Spectrum.

The Energy Density Spectrum ($E(\omega)$) is now defined from Hinze [40] as (Eq. 4.8). Further investigation reveals that this equation is a form of "Parseval's equality" (or theorem). The reader is referred to Logan [41] for a more strict mathematical definition of the equality and its properties.

$$\int_0^\infty E(\omega)d\omega = \overline{u(t)^2} = u'^2 \qquad \text{(Eq. 4.8)}$$

While (Eq. 4.8) may be sufficient in defining the Energy Density Spectrum's properties, it still does not reveal how to calculate the function directly. To do so, an EDS definition given by Stull [42] is adapted to account for the normalizing constants used in the Cooley-Tukey FFT algorithm. This definition is given as (Eq. 4.9) and has units of turbulence kinetic energy per frequency $\left[\frac{m^2}{s^2 Hz}\right]$.

$$\mathrm{E}(\omega) = \frac{[\Phi(\omega)_{real}]^2 + [\Phi(\omega)_{imag}]^2}{\Delta\omega \cdot N/2} \qquad \text{(Eq. 4.9)}$$

After calculating the EDS it is important to verify that it satisfies (Eq. 4.8). Once verified, the function can be plotted and analyzed as shown in an example from this study (Figure 35). The reader is referred to Hinze [40] and Tennekes and Lumley [43] for a more in depth look at the characteristics of the EDS.

During the signal processing it was found that calculating an EDS using just one $u(t)$ waveform produced a "noisy" result. Investigating the $E(\omega)$ data reveals that many neighboring frequency "bins" have very large differences in amplitude even though they

are separated by only $\Delta\omega$. This noise is believed to be erroneous by the investigator and is due to very high frequency resolution as determined by the sampling frequency and period. To reduce the variation of the $E(\omega)$ function, many $u(t)$ waveforms are taken, processed, and their individual $E(\omega)$ functions averaged. Such a process was used to produce the results in Figure 35, which shows reduced variability. Additionally, a smoothing of the data may be acceptable so long as coherent frequencies are not averaged out. This technique was also used in the study. The smoothed Energy Density Spectrum was found to still satisfy (Eq. 4.8) to within $0.03 \cdot u'^2$.

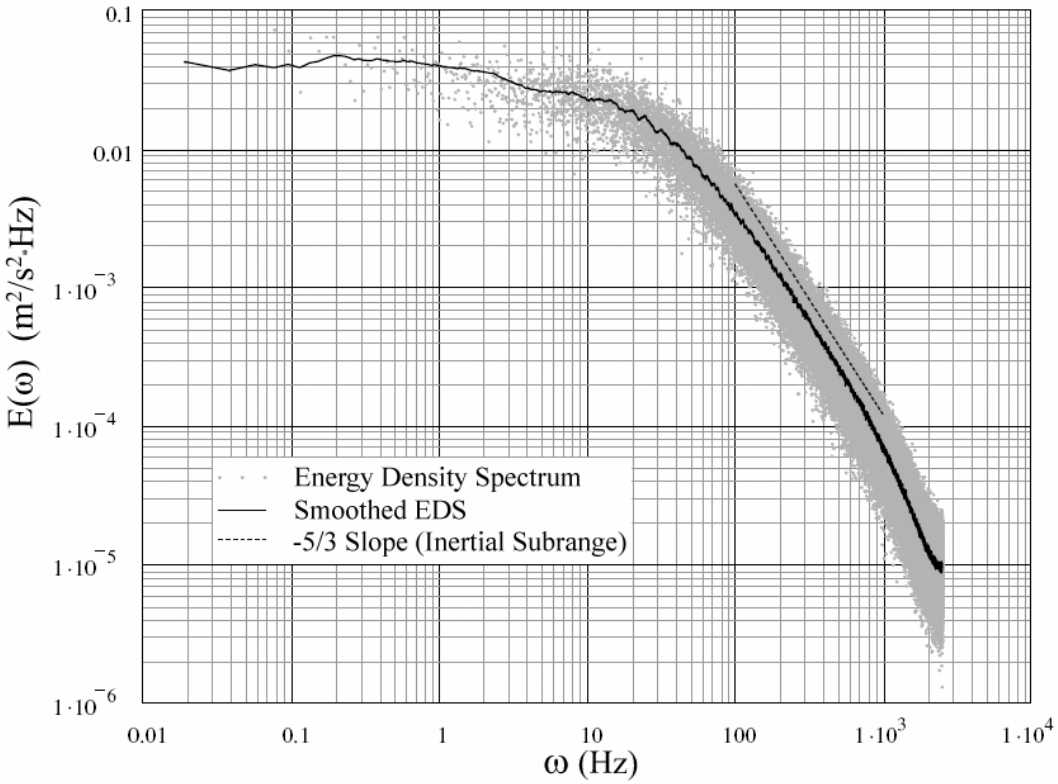

Figure 35. Example Energy Density Spectrum

In analyzing the above EDS, a linear region with a negative slope is identified roughly between 100 – 800 Hz for this example. This region, called the "inertial subrange," was first identified by Kolmogorov as a range of the spectrum which is completely dominated by the dissipation of kinetic energy. The inertial subrange was

later found to follow an empirical relationship at the smallest scales of the spectrum, called the "dissipation range," given in Ames and Moffat [44]:

$$\mathrm{E}(k) = \frac{18}{55} \cdot A \cdot \varepsilon^{2/3} \cdot k^{-5/3}$$

where:

k	=	Wavenumber
ε	=	dissipation of kinetic energy (Section 4.2.3)
A	=	Constant, taken as 1.62 (Ames and Moffat [44])

This relation, known as the "Kolmogorav Spectrum Law," can be reformulated as a function of frequency as in (Eq. 4.10). It will be used for comparison to measured data further on.

$$\mathrm{E}(\omega) = \frac{18}{55} \cdot A \cdot \varepsilon^{2/3} \cdot \omega^{-5/3} \cdot \left(\frac{2\pi}{\overline{U}} \right)^{-2/3} \qquad \text{(Eq. 4.10)}$$

Another convenient relationship to consider when looking at an EDS is the von Kármán interpolation formula (von Kármán's Spectrum). It is an expression which requires knowledge of various turbulence properties to calculate an idealized spectrum. It is defined in (Eq. 4.11) as taken from Ames and Moffat [44]. This expression is used later on for comparison with a measured EDS.

$$\mathrm{E}(\omega) = \frac{4 \cdot u'^2 \cdot \Lambda}{\overline{U} \left[1 + \left(\frac{8\pi \cdot \omega \cdot \Lambda}{3 \cdot \overline{U}} \right)^2 \right]^{5/6}} \qquad \text{(Eq. 4.11)}$$

From a measured Energy Density Spectrum such as the one shown in Figure 35, an Energy Spectral Distribution can easily be calculated by multiplying each $E(\omega_j)$ by its corresponding ω_j frequency. The ordinate of an Energy Spectral Distribution plot then has units of turbulence kinetic energy (i.e. m^2/s^2). An example is shown in Figure 36. This plot of energy shows at a glance the frequency range(s) over which the larger fraction(s) of the total energy reside.

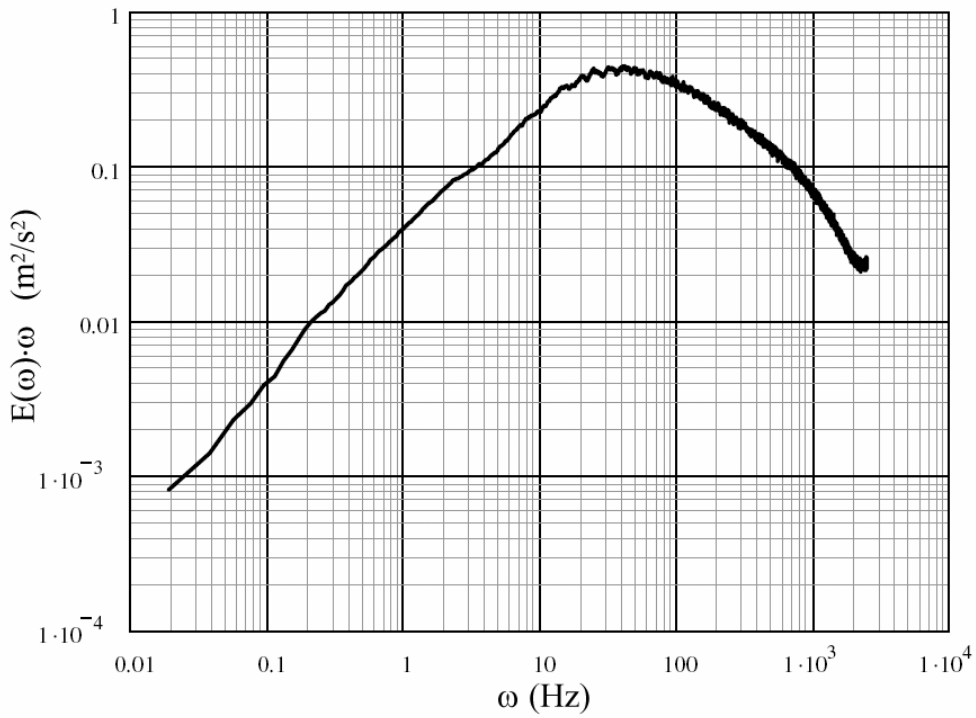

Figure 36. Example Energy Spectral Distribution

4.2.3 Integral Length Scale Λ, Energy Length Scale Lu, Dissipation ε, and Taylor Microscale λ

Several characteristics of turbulent motion may be quantified with the knowledge of a flow's Energy Density Spectrum. These characteristics allow for comparison to other turbulent flows as well as being key components within most, if not all, of the CFD turbulence models.

The first property of concern is the integral length scale, Λ. Physically, it represents a characteristic scale for the largest turbulent motions (eddies) found within a flow. Its computation from the EDS is described by Hinze [40] as:

$$\Lambda = \frac{\overline{U}}{4} \lim_{\omega \to 0} \frac{1}{u'^2} E(\omega) \qquad \text{(Eq. 4.12)}$$

Under certain conditions there may be a significant amount of error in calculating Λ from the EDS. This arises from an insufficient amount of data available as $E(\omega \to 0)$.

Therefore, it is very important (as stated previously) to sample the original signal for a long enough period to capture a sufficient number of waves at frequencies in this region. Hinze [40] recommends a cut-off frequency of 0.05 Hz or lower when evaluating this limit. The example EDS given above in Figure 35 appears to exhibit stable behavior for $\omega \to 0$ as displayed by a fairly flat line. It is noted, however, that there are very few data points below 1 Hz which introduces uncertainty into the calculation of Λ.

The second turbulence parameter to be calculated is the turbulence kinetic energy dissipation ε. This is physically the rate at which kinetic energy is converted to internal energy by means of viscous dissipation. Its approximation also requires an analysis of the EDS to identify the "inertial subrange" or "equilibrium range." This is the range of eddy sizes (wavenumbers) that Kolmogorov [45] first hypothesized to be in statistical equilibrium regarding energy transfer. The turbulence in this range is said to be isotropic with its eddy scales "cascading" down in size. This range of scales is identified in Figure 35 by the region which follows a $\omega^{-5/3}$ slope. With this region identified it is possible to approximate ε by (Eq. 4.13). This expression is simply a rearrangement of the Kolmogorov spectrum law (Eq. 4.10).

$$\varepsilon \approx 16.2 \frac{E(\omega_1)^{3/2} \cdot \omega_1^{5/2}}{\overline{U}} \qquad \text{(Eq. 4.13)}$$

where

ω_1 = Any single frequency chosen within the inertial subrange

$E(\omega_1)$ = The value of EDS which corresponds to ω_1

The next characteristic to be identified is the energy length scale, Lu. This property is an approximation of the mean energy-containing eddy size in a turbulent flow. It is defined by Ames and Moffat [44] as:

$$Lu = 1.5 \cdot \frac{u'^3}{\varepsilon} \qquad \text{(Eq. 4.14)}$$

Finally, a turbulence parameter referred to as the Taylor microscale, λ, is determined. This quantity approximates the eddy size at which viscosity begins to

dissipate kinetic energy. This is essentially where the inertial subrange ends and the viscous dissipation range begins. From Hinze [40]:

$$\lambda = \sqrt{\frac{15\nu \cdot u'^2}{\varepsilon}} \qquad \text{(Eq. 4.15)}$$

4.3 Pressure Measurements

Pressure measurements are important in many areas of this study including aerodynamic losses, blade pressure distributions, leakage flow documentation, and general qualification of the test section. The two types of pressure gages used fall under the categories of manometers and transducers. In conjunction with the pressure gages, instruments such as impact tubes, static tubes, and static pressure taps allow for pressure measurements to be made anywhere within the test section.

4.3.1 Manometry

In cases where a steady or mean pressure is to be measured, a simple differential manometer is used. These devices are liquid filled and operate on the principle of hydrostatic pressure due to changes in fluid column elevation. The two manometers used will be distinguished as a U-tube manometer and inclined manometer.

4.3.1.1 U-Tube Manometer

For differential pressures in the range of 0-500 Pa (0-2" H_2O) a Dwyer Microtector® Model 1430 Electronic Point Gage is used. Such applications in this study include the calibration of hotwire sensors and pressure transducers.

The device operates with a distilled water/Dwyer A126 fluorescein mixture as its gage fluid. A NIST traceable micrometer is mounted on one of the U-tube legs to read ½ of the displaced pressure as shown in Figure 37. When the micrometer point contacts the gage fluid surface, a D.C. signal is produced by the device's circuitry and displays on the

---

Microtector® is a Registered Trademark of Dwyer Instruments, Inc.

front panel ammeter. Thus, the ammeter display and circuitry are useful in improving repeatability and resolution.

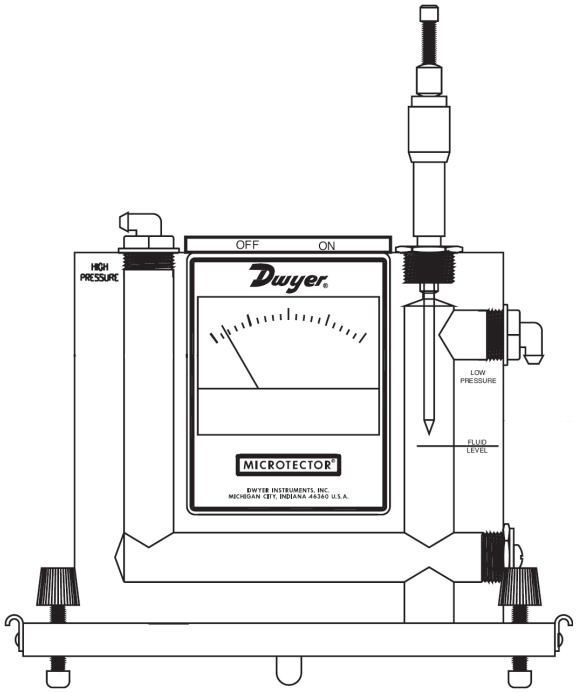

Figure 37. Dwyer Microtector® adapted from Dwyer[46]

According to Bulletin D-57 [46], Dwyer reports the device has an "accuracy and repeatability within ±0.00025 inches water column throughout its 0 to 2 inches w.c. range." Through experimental use, however, it is observed that these values are likely higher. A more conservative magnitude of ±0.25 Pa (±0.001" H_2O) is recommended.

It should also be noted that the device was designed according to the density of the gage fluid at 277 K (4°C). Considering the thermal expansion characteristics of water, this fact adds little error when measuring at room temperatures. For example, at a laboratory temperature of 300 K, the error due to density variation with temperature would be around 0.7%. If desired, a temperature correction may be made to the differential pressure measurement. This is done in the data reduction process when calibrating hotwire sensors.

4.3.1.2 Inclined Tube Manometer

For measuring differential pressures in the range of 0-1500 Pa (0-6" H_2O) a Dwyer inclined manometer model 246 is used. Such applications in this study include pressure measurement across the leakage flow meter, transducer calibration, and adjustment of the diffuser tailboards according to blade static pressure magnitudes.

The inclined manometer as shown in Figure 38 uses Dwyer red gage oil as its working fluid. Readings are taken at the location of the gage oil's meniscus along the inclined tube. The reported accuracy of this device is ±2.5 Pa (±0.01" H_2O).

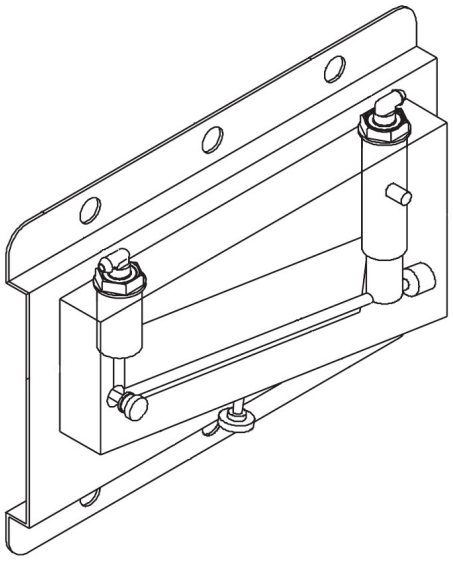

Figure 38. Dwyer Inclined Manometer adapted from Dwyer[46]

4.3.2 Pressure Transducers

Since the test section's flow field is highly unsteady, pressure transducers with high frequency response are required for most measurements. The transducers used are of the variable reluctance type (Model DP15) made by the Validyne Engineering Corporation. Each transducer has a replaceable stainless steel diaphragm as its sensing element which must be designed to operate within the applicable pressure range. In all cases, a Validyne model 3-22 diaphragm with a full scale range of ±1400 Pa (±5.5" H_2O) is sufficiently large for this study. Diaphragms with smaller pressure ranges may be used for specific applications as necessary.

Connected to each transducer is a bridge circuit provided by a Validyne Model CD15 Carrier Demodulator. This circuit senses inductance variations (caused by pressure changes) within the transducer's inductance coil and outputs a rectified DC signal. The voltage output amplitude is within the ±10 volt range which must be calibrated to represent the pressure's polarity and magnitude.

The reported accuracy of the DP15 is 0.25% of the full scale pressure range as reported by the manufacturer. This is specified to include effects of non-linearity, hysteresis, and non-repeatability. For further details regarding the DP15 pressure transducer or CD15 carrier demodulator consult Validyne [47].

4.3.2.1 Transducer Calibration Process

The calibration process is required to correlate each transducer's relationship between differential pressure and output voltage. The pressure source used for calibration is the same apparatus used for hotwire calibration described in Section 4.1.1.1. In addition to the calibration jet, other equipment required includes a voltmeter, plastic tubing, inclined manometer (Section 4.3.1.2), data acquisition software and hardware, 4-pin transducer cable, and BNC-to-terminal cables. Using this equipment, the general connections are made as shown in Figure 39 and the calibration procedure is as follows:

Using equal lengths of plastic tubing, connect the calibration jet's inner chamber static pressure tap (see Figure 29) to both the inclined manometer and pressure transducer's high pressure ports. Electrically connect both the transducer to the carrier demodulator using Validyne's 4-pin transducer cable, and the voltmeter to the CD15's output terminals. With the transducer open to atmosphere on both sides of its diaphragm adjust the CD15's ZERO potentiometer until the voltmeter reads 0 volts DC. The next step is to open the calibration jet's throttling valves until a ΔP of 1400 Pa (5.5" H_2O) is read on the inclined manometer. Then using the CD15's SPAN potentiometer, adjust until the voltmeter output reads nearly +10 volts. The calibration jet may then be turned off and the voltmeter must be used to recheck that a $\Delta P = 0$ produces 0 volts. If not, use the ZERO potentiometer to make the appropriate adjustments.

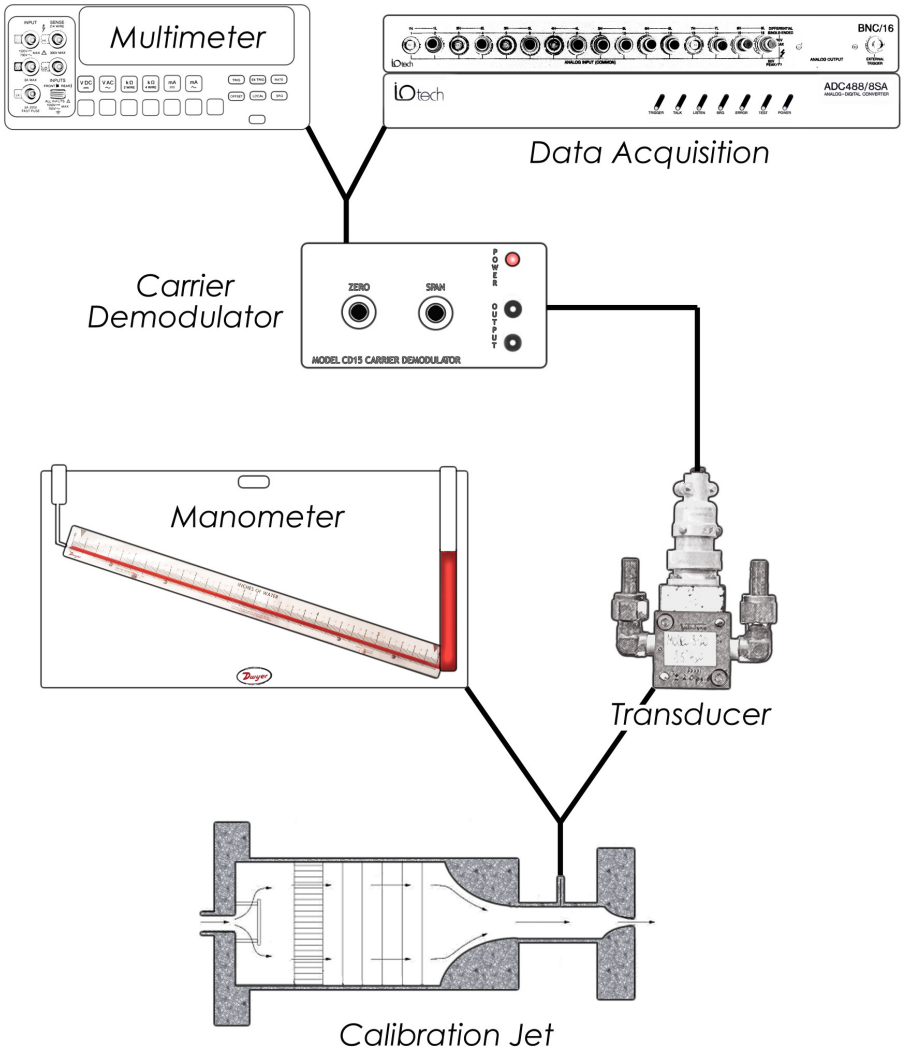

Figure 39. Pressure Transducer Calibration Setup

Now that the carrier demodulator has been configured for the appropriate dynamic range, connect the CD15's output terminals to the data acquisition hardware using the BNC-to-terminal cables. Again using the calibration jet's throttling valves and the inclined manometer, record various values of ΔP within the appropriate pressure range by hand and sample the CD15's output voltage using data acquisition software for a period of 30 seconds. When a sufficient number of ΔP values have been sampled in the 0-1400 Pa (0-5.5" H_2O) range, reverse the plastic tubing connection on the transducer from the high to low pressure port. The process in this paragraph is then repeated noting that the diaphragm should be flexing in the opposite direction as a result of $-\Delta P$ values. If the $+\Delta P$ and $-\Delta P$ lines do not extend linearly through the origin, a hysteresis exists

indicating that the diaphragm has been stretched and must be replaced. Sample transducer calibration data is given in the next section.

4.3.2.2 Transducer Calibration Results

After completing the calibration procedure in the previous section, resulting pressure and voltage data must be analyzed. Since transducer voltage was sampled at a given frequency for a 30 second period, the values from each reading are averaged. This process yields one pressure reading and an average voltage for each calibration point. The data are then plotted as in Figure 40 and a least squares fit is performed to produce a cubic polynomial. In general the transducer's voltage versus ΔP response is quite linear; however, a higher order function results in lower residuals. As an example, the least squares fit performed on the data in Figure 40 resulted in the function $\Delta P = 0.0296 \cdot E^3 + 0.0005 \cdot E^2 + 143.59 \cdot E - 2.4922$.

It should also be noted that the transducer/carrier demodulator's DC voltage will drift with time and temperature changes. For this reason, it is important to use the CD15's ZERO potentiometer and adjust the output to 0 volts at $\Delta P = 0$ before each measurement cycle.

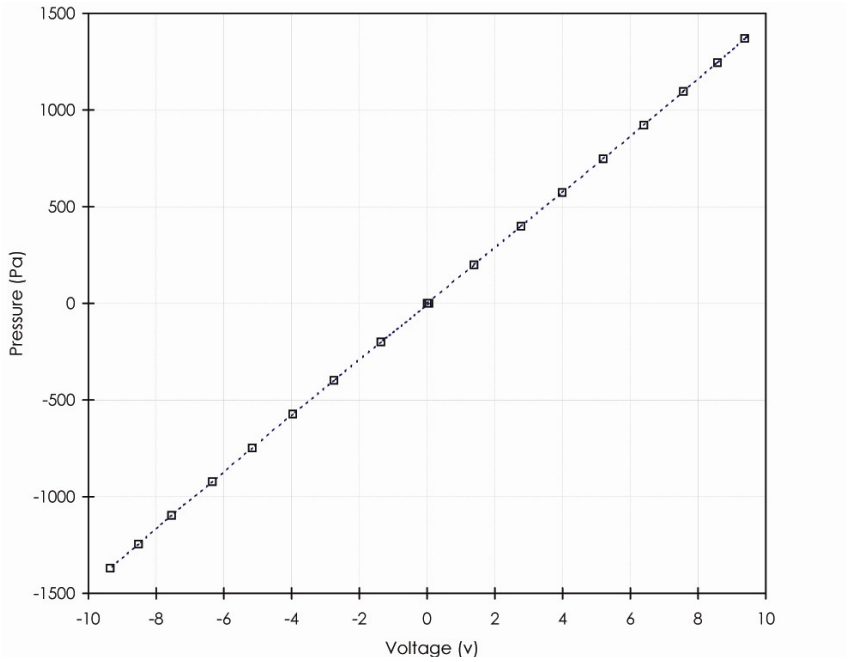

Figure 40. Typical Pressure Transducer Calibration Data

4.3.3 Static/Total Pressure Tubes and Taps

Various pressure tubes are used within the test section to survey both total and static pressures. In all cases, these instruments are connected to pressure transducers by means of plastic tubing for measurement. Also used in this facility are static pressure taps at the midspan of each blade. The taps are fully described in Section 3.2.1.2. When using these instruments, it is worth noting that compressibility and viscous effects were found to be of negligible importance as briefly described in Section 4.1.2.

According to Goldstein [29], measurement errors using these instruments are mainly caused through misalignment, turbulence, wall proximity effects, tap hole geometry, probe nose geometry, probe support influence, and probe size. The design of probes and taps used in this study is significant enough to minimize many of these errors. Where corrections can be made as in measuring total pressure near a wall, they are performed based on the recommendations in Goldstein [29].

4.4 Flow Rate Measurements

The measurement and documentation of volumetric and mass flow rates are important in studying effects of leakage flow. A commercial laminar flow meter used to make these measurements is described below.

4.4.1 Laminar Flow Meter

Installed inline with the auxiliary leakage flow (Section 3.1.2.3) is a Meriam Instrument "Laminar Flow Element," Model 50MC2-4. This particular flow meter has a range of 0-0.19 m^3/s (0-400 CFM) and is calibrated against a National Institute of Standards and Technology (NIST) traceable master flowmeter by the manufacturer. The reported calibration uncertainty is ±0.72% at a 95% confidence level. The manufacturer provides calibration constants which are used within (Eq. 4.16) to calculate actual volumetric flow rates. These flow rates are termed "actual" as they are not converted to standard temperature and pressure conditions. It is noted that (Eq. 4.16) includes a viscosity

correction in the form of μ_{std}/μ which accounts for temperature and relative humidity effects relative to calibration conditions.

$$Q = \left(50.0651 \cdot \Delta P - 0.0692834 \cdot \Delta P^2\right) \cdot \frac{\mu_{std}}{\mu_f} \qquad \text{(Eq. 4.16)}$$

where

Q = Actual flow rate (ft^3/min)
ΔP = Pressure Gradient across flow meter (in H_2O)
μ_{std} = Dynamic viscosity of air at 70ºF
μ_f = Dynamic viscosity of air at test temperature and R.H.

In order to calculate the actual volumetric flow rate, properties such as differential pressure, flow temperature, and relative humidity are needed. The differential pressure is measured across the flow meter using equal lengths of ¼" plastic tubing and a inclined tube manometer. Both the flow temperature and relative humidity are measured using an HH311 Humidity Temperature Meter made by Omega Engineering, Inc.

4.5 Temperatures Measurements

All temperature measurements are made with chromel-constantan (Type E) thermocouples and an Agilent 34970A data acquisition unit. The thermocouple operates on a phenomenon known as the "Seebeck effect"— where temperature gradients produce changes in a circuit's electrical potential. This is achieved by joining two dissimilar metals to create a "junction." Since thermocouples only measure temperature differences, a circuit needs two junctions to obtain absolute temperatures. One junction must be held at a known constant temperature ("Reference junction"), while the other is used to measure the relative temperature of interest.

In this study, relative temperature (ΔT) is the desired property. This fact allows for the use of a simple thermistor-based reference junction compensation method. This method would not be advised for precision absolute temperature measurements as it introduces additional uncertainty; however, it will contribute no such error in the measurement of ΔT. Additionally, this method is simple to apply as it is built into the data acquisition unit used.

4.5.1 Thermocouple Calibration Check

As stated previously, the choice was made to measure temperatures with the Agilent 34970A data acquisition unit. This hardware includes both internal electrical cold-junction compensation and voltage-to-temperature conversion based upon N.I.S.T. data from Burns et al. [48]. For these reasons, it was decided to use the hardware's internal functionality and perform a "calibration check." If the calibration check's results were deemed acceptable, no further calibration would be needed.

The calibration check is performed in an insulated water bath containing roughly 10 liters of water. The water is heated with a Polytemp model 73 heater/mixer assembly (Polyscience Corporation) mounted on the bath's cylindrical lid. The lid also holds four glass tubes into which thermocouple junction's are placed. The junction at the bottom of each glass tube is submerged in silicon oil to provide electrical isolation while maintaining thermal conductivity with the surrounding water. Finally, a precision mercury thermometer (0.1°C increments) is placed at the center of the water bath to serve as the calibration standard. The water bath facility is depicted in Figure 41 (with the cover removed).

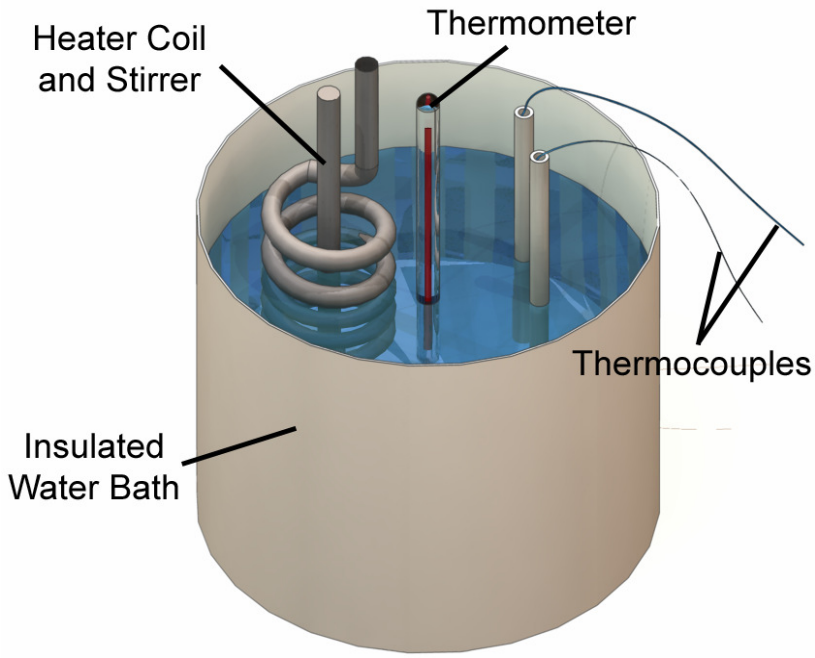

Figure 41. Water Bath Facility used in Thermocouple Calibration Check

The calibration check begins by heating up the water bath to the maximum temperature desired. Once obtained, the heater is turned off while leaving the stirrer on. The water is allowed to slowly cool down to room temperature over the period of hours while the stirrer evens out any temperature gradients which may exist. During the cool down process, thermocouple readings are taken periodically and compared to thermometer temperatures.

4.5.2 Thermocouple Calibration Check Results

Results from the calibration check of four Type E thermocouples are given in Figure 42 showing thermocouple versus thermometer temperatures. From these data, a maximum deviation between thermocouple and thermometer temperatures is calculated to be 0.1°C. Absolute temperature, however, is not the desired quantity. To see how accurately the thermocouples reproduce incremental changes in temperature (ΔT), the temperature change between each measurement point is calculated. Data from the thermometer and thermocouples are again compared and found to have a maximum deviation of 0.024°C in ΔT. This value is well below the uncertainty of reading a thermometer with 0.1°C increments (±0.05°C). Also as a visual comparison using Figure 42, it is seen that the thermocouple data have a linear trend with the slope of 1. These findings suggest that using the current measurement setup is sufficient in measuring ΔT as long as all thermocouples are initially normalized to one common temperature.

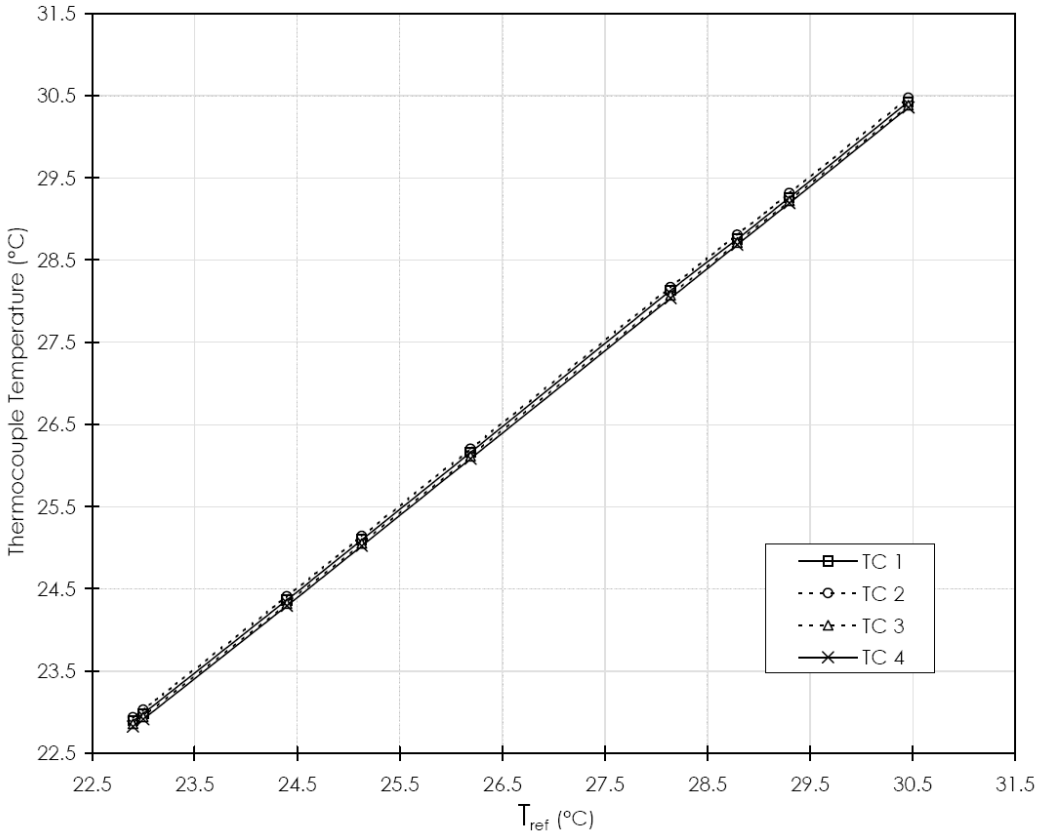

Figure 42. Thermocouple Calibration Check Results

Chapter 5

Experimental Procedure

With the measurement techniques explained, it is now necessary to describe each type of experiment and the respective procedures. This chapter provides details of how experiments measuring passage aerodynamic loss, endwall adiabatic film cooling effectiveness, and passage temperature fields are performed.

5.1 Passage Aerodynamic Loss

5.1.1 Background

Aerodynamic loss measurements are used to document irreversibility within the passage flow. Loss sources include boundary layers, secondary flows, turbulent mixing, and leakage flow injection. Since losses decrease stage efficiency, it is important to understand how they are affected by leakage flow injection and endwall contouring. To capture these effects, six experiments are performed. Losses are measured at the passage exit plane ($x/C_{ax}=1$) for both the dolphin nose and shark nose endwall contour geometries at leakage MFR's of 0.5%, 1.0%, and 1.5%.

The quantity used to describe aerodynamic loss is the loss coefficient, $C_{p,Loss}$, defined in (Eq. 5.1). This coefficient helps identify areas where higher-entropy fluid has migrated and to what extent the entropy has increased through the passage. It is comprised of three local pressures – the passage inlet total pressure $P_{t,0}$, local exit total pressure $P_{t,1}$, and passage exit static pressure $P_{s,1}$. The locations of these pressure measurements with respect to the passage are shown in Figure 43.

$$C_{p,Loss}=\frac{P_{t,0}-P_{t,1}(x,y)}{P_{t,0}-P_{s,1}} \qquad \text{(Eq. 5.1)}$$

The numerator of (Eq. 5.1) represents a change in total (stagnation) pressure between the passage inlet and exit planes. An ideal fluid would have a numerator of zero. The denominator represents the dynamic head an ideal fluid would have at the exit plane (lossless flow between stations 0 and 1).

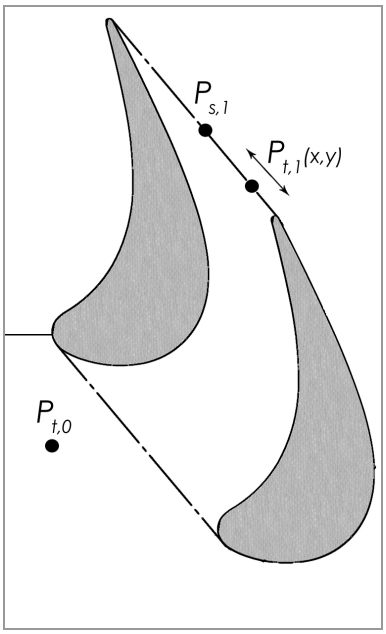

Figure 43. Locations of Pressure Measurements Relative to Blade Passage

5.1.2 Procedure

In order to calculate a loss coefficient, three pressures (shown in Figure 43) must be measured simultaneously. The first pressure, $P_{t,0}$, is measured with an impact tube slightly upstream of the inlet plane ($x/C_{ax} = 0$) at mid-span and mid-pitch. The exit plane static pressure, $P_{s,1}$, is taken with a static tube at mid-pitch and approximately 40% span. Lastly, the passage exit total pressure, $P_{t,1}(x, y)$, is taken at 256 locations on the exit plane ($x/C_{ax} = 1$) with a traversing total pressure tube. These measurement locations are shown in Figure 44. The measurement grid is more dense near the walls and coarsens upon moving outward.

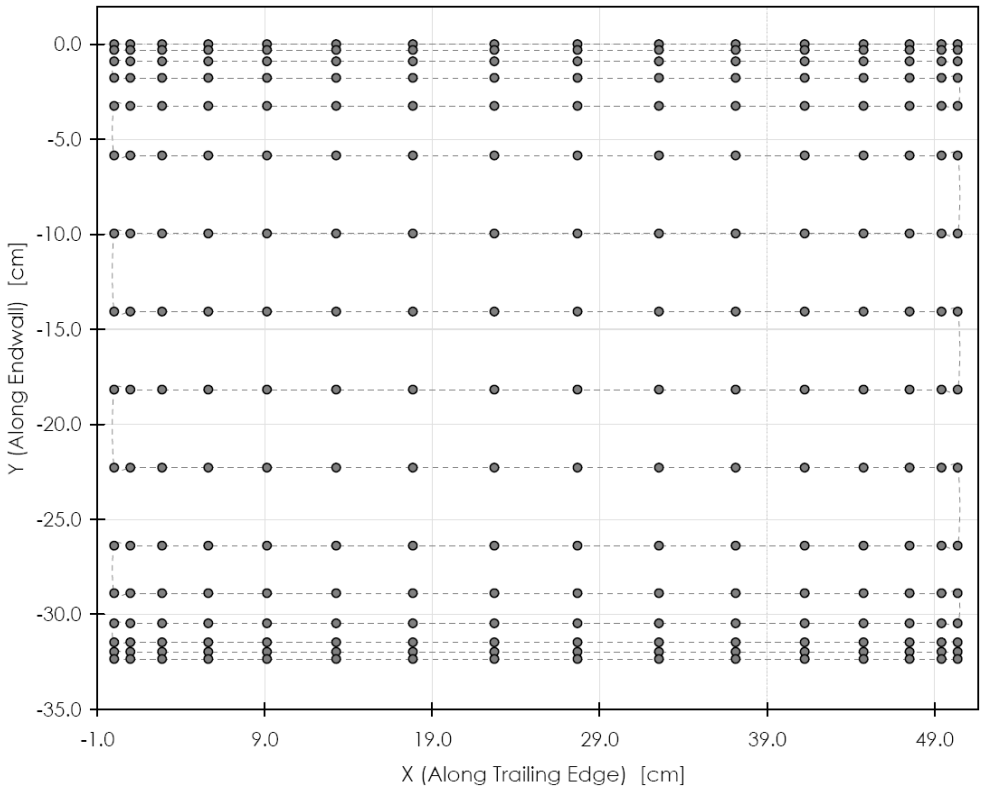

Figure 44. Location of Total Pressure Measurements at the Passage Exit Plane

During the experiment, the three pressure tubes are connected to differential pressure transducers (Section 4.3.2) via plastic tubing. The transducers are electrically connected to the IOtech ADC488 for signal acquisition. The *ME DAQ* software program (Section **Error! Reference source not found.**) is used to control the data acquisition hardware and motor traversing system (Section 3.4.3). This setup enables automated probe movement, signal acquisition, and data reduction.

One other important aspect of aerodynamic loss measurements is pressure tube-to-flow alignment. This is achieved by rotating the pressure tube while monitoring the pressure transducer's output voltage. Since a total pressure tube having a 0° angle of incidence would produce the highest (most accurate) total pressure, impact tubes are rotated until a maximum transducer voltage is obtained. Similarly the static tube is rotated until a minimum transducer voltage is obtained. This process is very important in reducing measurement error.

Finally, pressure measurements are taken and loss coefficients calculated for all 256 exit plane measurement locations. Each pressure measurement is sampled at a rate of 100 Hz for 30 seconds to obtain an average.

5.2 Passage Temperature Fields

5.2.1 Background

Measurements of flow field temperature are made to trace the leakage flow through the blade passage. This information is useful in understanding the leakage flow's utility, as well as endwall secondary flow behavior. Since temperature is a scalar property, it also gives information on other flow characteristics, such as dispersion. Several experiments are carried out to capture these effects under different flow conditions. A total of six data sets are created consisting of the dolphin nose and shark nose endwall contour geometries at leakage MFR's of 0.5%, 1.0%, and 1.5%.

Flow field measurements are scaled in the form of dimensionless recovery temperatures, θ, as shown in (Eq. 5.2). Since the flow is of low velocity, kinetic energy has little effect making static and recovery temperatures essentially equal. The local variable $T(x, y, z)$ is measured at different locations within the passage. For calculation of θ, approach flow (T_0) and leakage flow (T_ℓ) temperatures are also measured. T_ℓ is defined as the average fluid temperature being delivered through the rim seal gap within the leakage plenum (Refer to Section 3.2.3.1). This definition is important as in some cases mainstream fluid can flow into the leakage plenum, changing the fluid temperature delivered at the leakage flow slot. Also, since differences in temperature (ΔT) are used in computing θ, uncertainty values are low (typically less than 5%).

$$\theta(x, y, z) = \frac{T(x, y, z) - T_0}{T_\ell - T_0} \qquad \text{(Eq. 5.2)}$$

5.2.2 Procedure

Before measurements begin, regions within the blade passage where temperatures are desired must be identified. These measurements occur on endwall-normal planes and are displayed in Figure 45 at locations of constant x/C_{ax} (-0.296, 0, 0.247, 0.44, and 0.92). Within each plane, filled circles identify temperature sampling locations. It is seen that measurements are more concentrated near the contoured endwall surface (bottom wall). In total, each passage temperature field data set is comprised of 837 sampling locations.

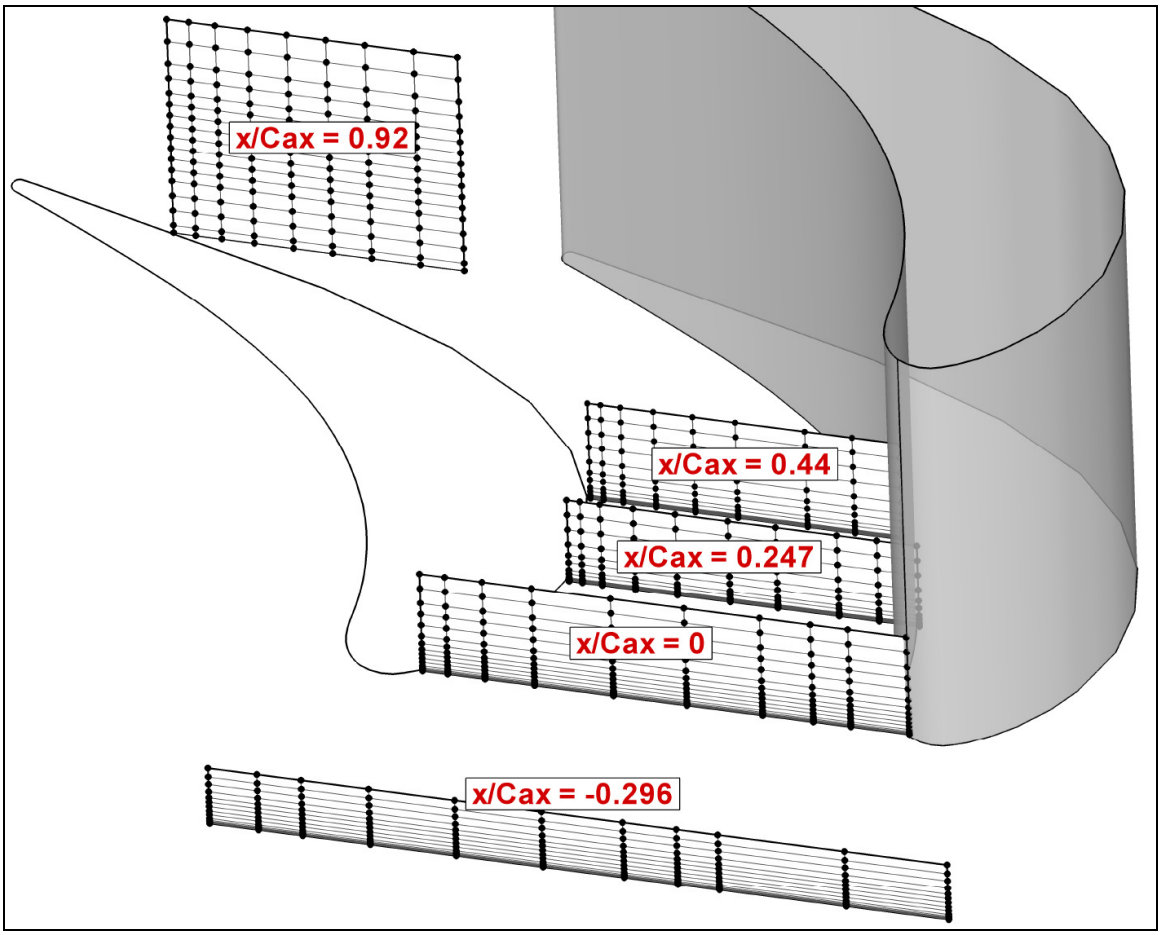

Figure 45. Flow Field Temperature Measurement Locations

Also before each experiment begins, a test section warm-up period of about 2 hours is required to attain steady state. During this time, a resistance heater delivers energy to the auxiliary leakage flow at a rate of approximately 750 Watts. This produces an increase in leakage flow temperature of 8-10ºC above the approach flow temperature

(varies with flow rate). The main flow is at room temperature, typically in the vicinity of 24ºC.

During the experiment, temperatures are measured by seven Type-E (chromel-constantan) thermocouples. Five of the thermocouples are used to measure fluid temperature at the rim seal gap. These temperatures are averaged to obtain T_ℓ. The approach flow temperature is recorded with a single thermocouple placed slightly upstream of the inlet plane ($x/C_{ax} = 0$) at mid-span and mid-pitch. The final thermocouple has a mild bend to allow the near-tip region to be aligned with the flow. It is used to measure local temperatures within the passage ($T(x, y, z)$). This probe is mounted onto the motor traversing system (Section 3.4.3) for movement within the blade passage.

Signal acquisition is handled using the Agilent 34970A unit. Both the data acquisition hardware and motor traversing system are controlled using the *ME DAQ* software program (Section **Error! Reference source not found.**). All thermocouples are sampled at a rate of 1 Hz for 20 seconds at each measurement location shown in Figure 45. The samples are then averaged to obtain one temperature for each of the seven thermocouples.

5.3 Endwall Adiabatic Film Cooling Effectiveness

5.3.1 Background

A practical consideration in the study of leakage flow is its ability to provide cooling to the endwall surface. The leakage flow's cooling potential is described herein as adiabatic film cooling effectiveness. To calculate such a quantity, one must be able to accurately measure the endwall surface temperature, as well as verify that the adiabatic boundary condition ($dT/dy\big|_{y=0}$) is satisfied there. In this study, the endwall is made of a low thermal conductivity material (Refer to Section 3.2.2) and the test section is heated until it attains steady-state operation. These conditions give rise to an endwall that very

closely approximates an adiabatic surface. Near-wall temperature gradients are measured to verify that this is true.

Adiabatic film cooling effectiveness (η) is calculated in an identical fashion as dimensionless recovery temperature, θ, in (Eq. 5.2). The difference is that surface temperature, not fluid temperature, is the desired property. It is defined in (Eq. 5.3), showing its relation to θ.

$$\eta(x,y) = \theta(x,y)\big|_{z=0} = \frac{T(x,y)_{z=0} - T_0}{T_\ell - T_0} \qquad \text{(Eq. 5.3)}$$

A total of six endwall adiabatic film cooling effectiveness data sets are created consisting of the dolphin nose and shark nose endwall contour geometries at leakage MFR's of 0.5%, 1.0%, and 1.5%. These six cases give insight into the effects of varying leakage flow rate and changing endwall contouring. Additionally, the six cases are then repeated with the wind tunnel approach flow being heated (as detailed in Section 6.2.3). The difference in results between unheated and heated approach flows allows for some insight into mixing of the leakage flow and near-wall approach flow.

5.3.2 Procedure

Most aspects of the adiabatic film cooling effectiveness measurement procedure are analogous to the passage temperature field procedure listed in Section 5.2.2. These include the test section warm-up period, use of thermocouples, data acquisition settings, and use of the motor traverse system. These topics are not repeated here, for brevity. The differences lie in the location of surface temperature measurements.

A total of 131 spatial locations (shown in Figure 46) are visited on the endwall with the traversing thermocouple probe. At each measurement location, the probe begins resting on the endwall surface. Readings are taken and the probe is incrementally moved outward normal to the surface at steps of 0.25, 0.5, and 1 mm until a distance of 5 mm has been traveled. Temperatures at each step are sampled at a frequency of 1 Hz for 20 seconds. This process is repeated for all 131 endwall measurement locations.

An example of several measured endwall-normal temperature profiles is given in Figure 47. These were selected randomly from a data set. Of particular importance is the

near-wall temperature gradient. All sample profiles shown exhibit either no gradient, or very small gradients within 1mm of the endwall. This observation agrees quite well with the assumed adiabatic wall boundary condition.

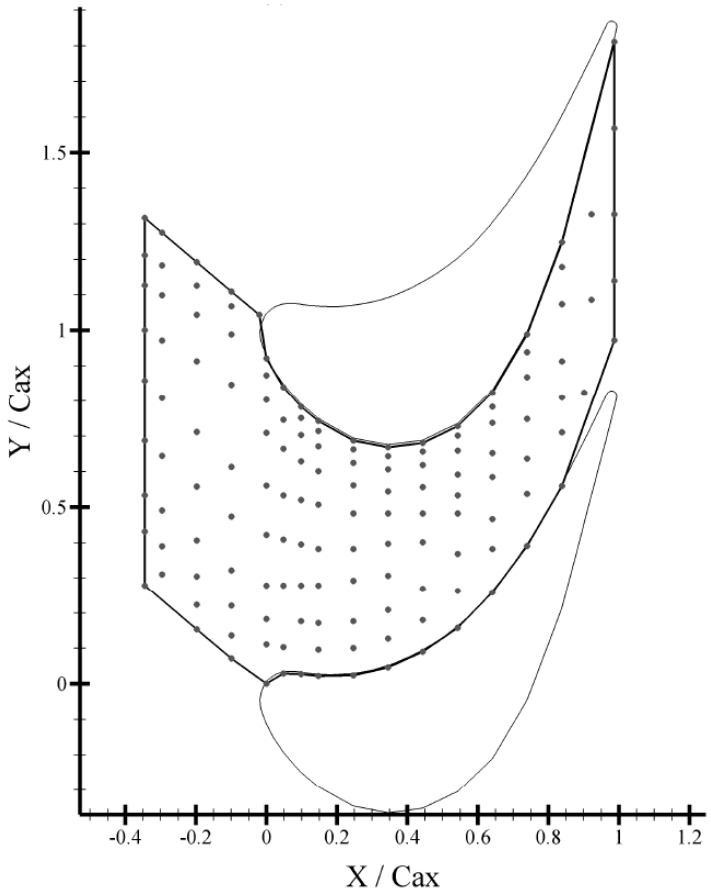

Figure 46. Endwall Adiabatic Film Cooling Effectiveness Measurement Locations

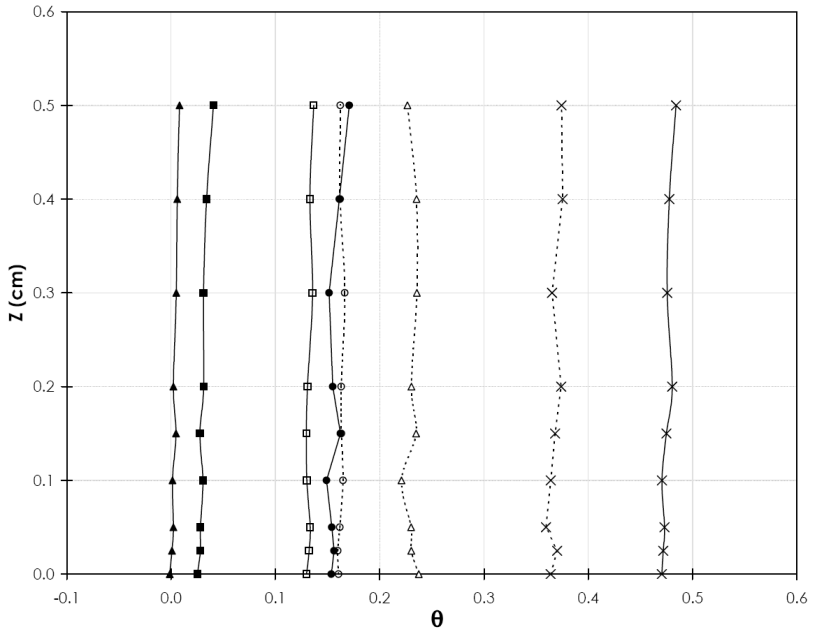

Figure 47. Randomly Selected Endwall-Normal Temperature Profiles

Chapter 6

Qualification of Experimental Flow

This chapter outlines the measurements made to qualify the test section. Most documentation pertains to the approach flow, including the velocity field, turbulence field, turbulence spectra, and temperature field. Also documented are the midspan blade static pressure profiles for the two passages.

6.1 Blade Static Pressure Profiles

Prior to qualification of the test section approach flow, measurements of blade static pressure profiles are made. Based upon these measurements, the diffuser walls are adjusted to "match" the amount of flow moving through each of the two blade passages (periodicity). This measurement and adjustment process is repeated until the blade pressure profiles are satisfactorily matched.

Measurements are made using pressure taps located at the midspan around each blade. Each tap (described fully in Section 3.2.1.2) is connected to a switchboard via plastic tubing, which then connects to a common pressure transducer (Section 4.3.2). Static pressures are measured at each tap for 30 seconds at a rate of 1 kHz using an IOtech ADC488 and *ME DAQ* software. Simultaneously, the passage inlet total and static pressures are measured with a pitot-static tube and transducer for comparison.

The resulting pressure profiles are reported in Figure 48 scaled as a pressure coefficient, C_p, as defined in (Eq. 6.1). The abscissa parameter x/C is the surface distance relative to the blade's leading edge, scaled on the chord length. The region to the left of x/C=0 represents the blade's pressure side, and to the right is the suction side. The passage labeled "Passage 1" is where the experiments are conducted.

$$C_p = \frac{P_s - P_{s,0}}{\frac{1}{2}\rho U_0^2} = \frac{P_s - P_{s,0}}{P_{t,0} - P_{s,0}} \qquad \text{(Eq. 6.1)}$$

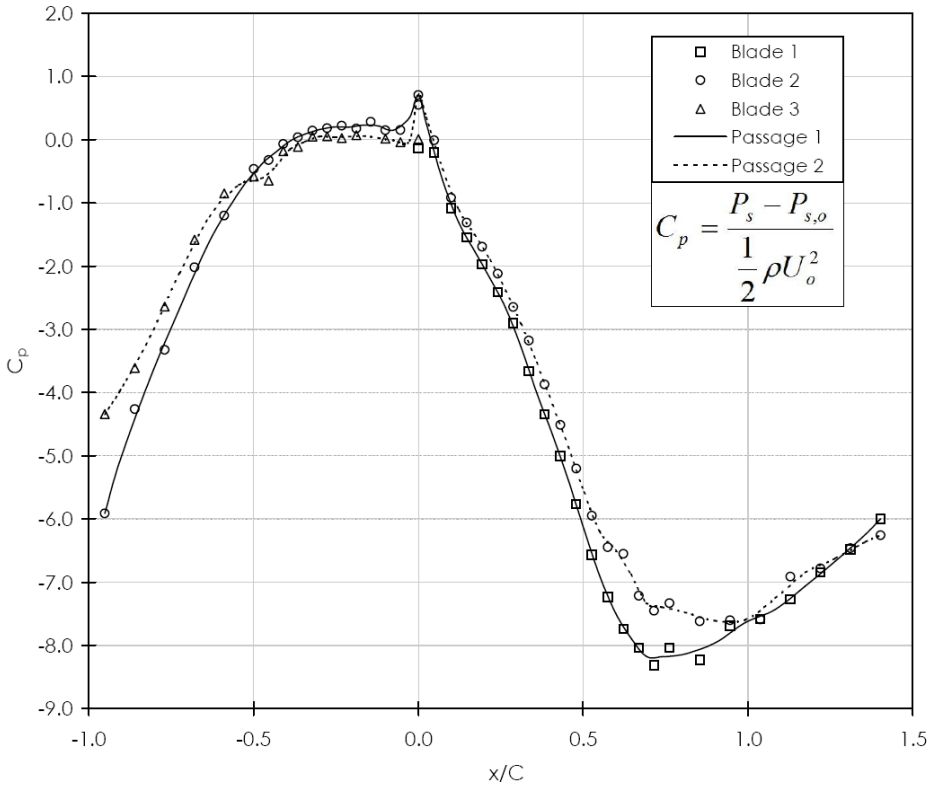

Figure 48. Blade Midspan Static Pressure Profiles

Difficulty in perfectly matching both passage pressure profiles is apparent in the above figure. The largest differences are seen on each blade's suction side near the passage throat. Adjustment of the diffuser (tailboard) walls had little to no effect in this region. Additionally, small differences are seen on the pressure surfaces alluding to slightly higher velocities in the Passage 1. At this point the blade static pressure profiles were deemed satisfactory with the understanding that small differences in periodicity still exist.

6.2 Approach Flow Velocity, Turbulence, and Temperature Fields

To document the approach flow, an inlet plane is defined at a constant distance ($x/C = -0.58$) upstream of the blade leading edge line. This plane accounts for the inlet flow angle of 40° and ensures that the probe is always a constant axial distance from the blades. Measurement probes are traversed along this plane to resolve the distribution of velocity, turbulence, and temperature.

6.2.1 Velocity Field

The approach flow velocity field for the upper passage is documented using thermal anemometry (Section 4.1.1). A hotwire probe is traversed along the inlet plane and velocities are recorded at a total of 164 locations. Data acquisition is controlled with the *ME DAQ* software program and IOtech ADC488 hardware. At each measurement location, voltages are recorded at a frequency of 5 kHz and period of 30 seconds. Raw voltages are converted to velocities within the software based upon calibration constants and (Eq. 4.1). Post-processing of the velocity data is done with the *Tecplot 360* software program. Data are interpolated between measurement locations to arrive at the contour plot shown in Figure 49.

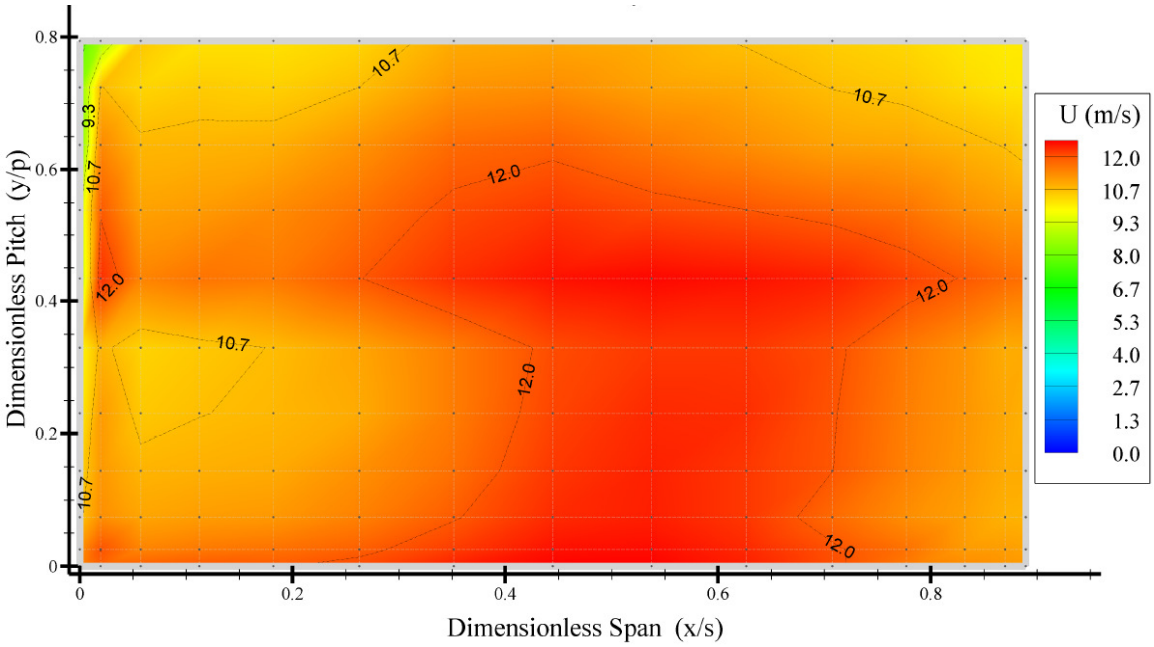

Figure 49. Approach Flow Velocity Field (x/C_{ax}=-0.58)

In general, the velocity field is uniformly distributed with a variation of ±10% from the mean ($U_0 = 11.5 m/s$). This uniformity is considered adequate for the study and is largely attributable to the large-scale mixing of the flow. Large eddy length scales also cause the wall-damping effect to extend further out into the flow. This results in a "core" region in the center of the tunnel where velocities are higher, and a slightly damped region surrounding it which extends approximately $0.2 \cdot C$ away from all walls. Also

noted is a region of lower velocity that exists as a result of a corner in the upper left hand side of Figure 49. This low momentum fluid is not considered significant, and much of it is let out of the test section before it enters the passage through downstream bleed slots.

6.2.2 Turbulence Field

The approach flow turbulence field for the upper passage is calculated by analyzing each 30 second velocity waveform from measurements in the previous section. Values for the standard deviation (u') and turbulence intensity (Tu) are calculated according to (Eq. 4.4) and (Eq. 4.5), respectively. Results are given as contour plots in Figure 50 and Figure 51.

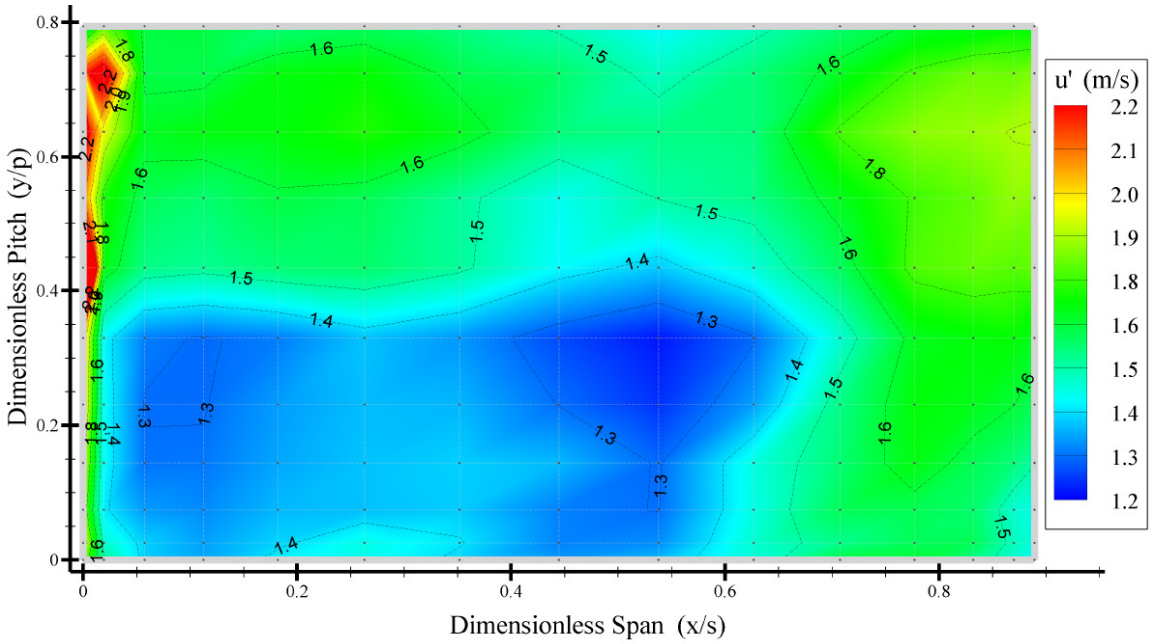

Figure 50. Approach Flow Distribution of u' (x/C_{ax}=-0.58)

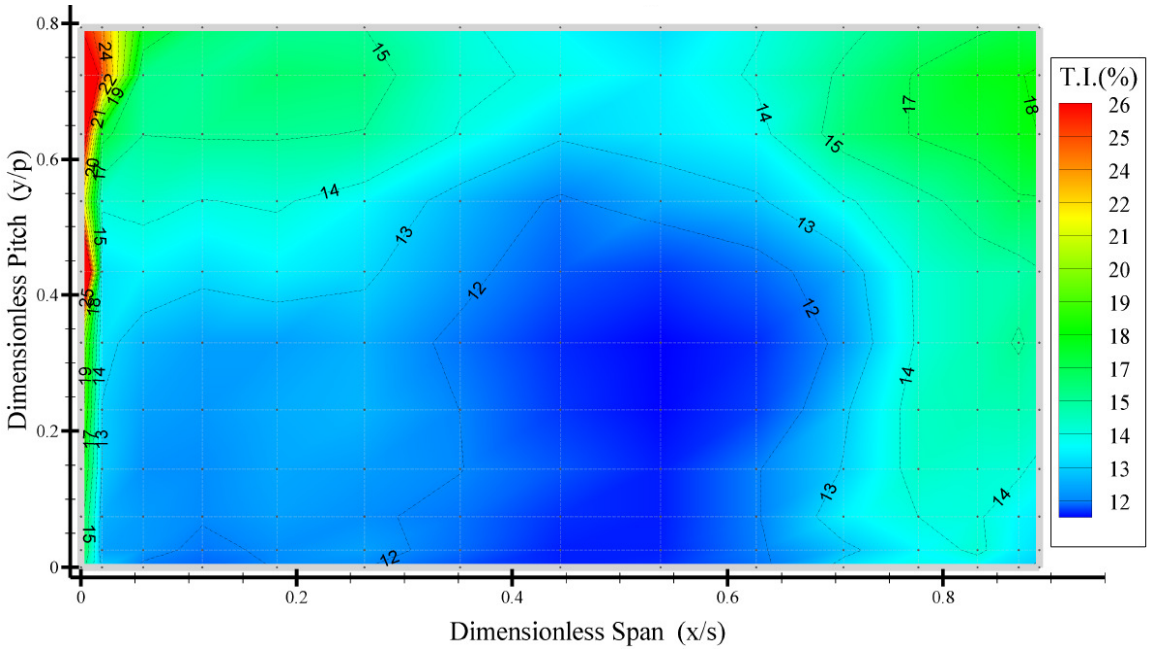

Figure 51. Approach Flow Distribution of *Tu* (x/C_{ax}=-0.58)

The previous contour plots show that turbulence is being generated in a fairly uniform fashion with a mean around $Tu = 14\%$. This uniformity is desired as it mimics the well-mixed highly turbulent flow leaving a gas turbine combustor.

6.2.2.1 Turbulence Characteristics

Additional measurements of turbulence are performed using thermal anemometry to resolve spectral characteristics in the main flow direction. A total of 10 velocity waveforms are captured at a single freestream location with a sampling frequency of 5 kHz and period of 60 seconds. Data processing is carried out according to the methods described in Section 4.2.2. The resulting energy density spectrum is plotted in Figure 52 to show the distribution of turbulence kinetic energy over a broad range of fluctuation frequencies.

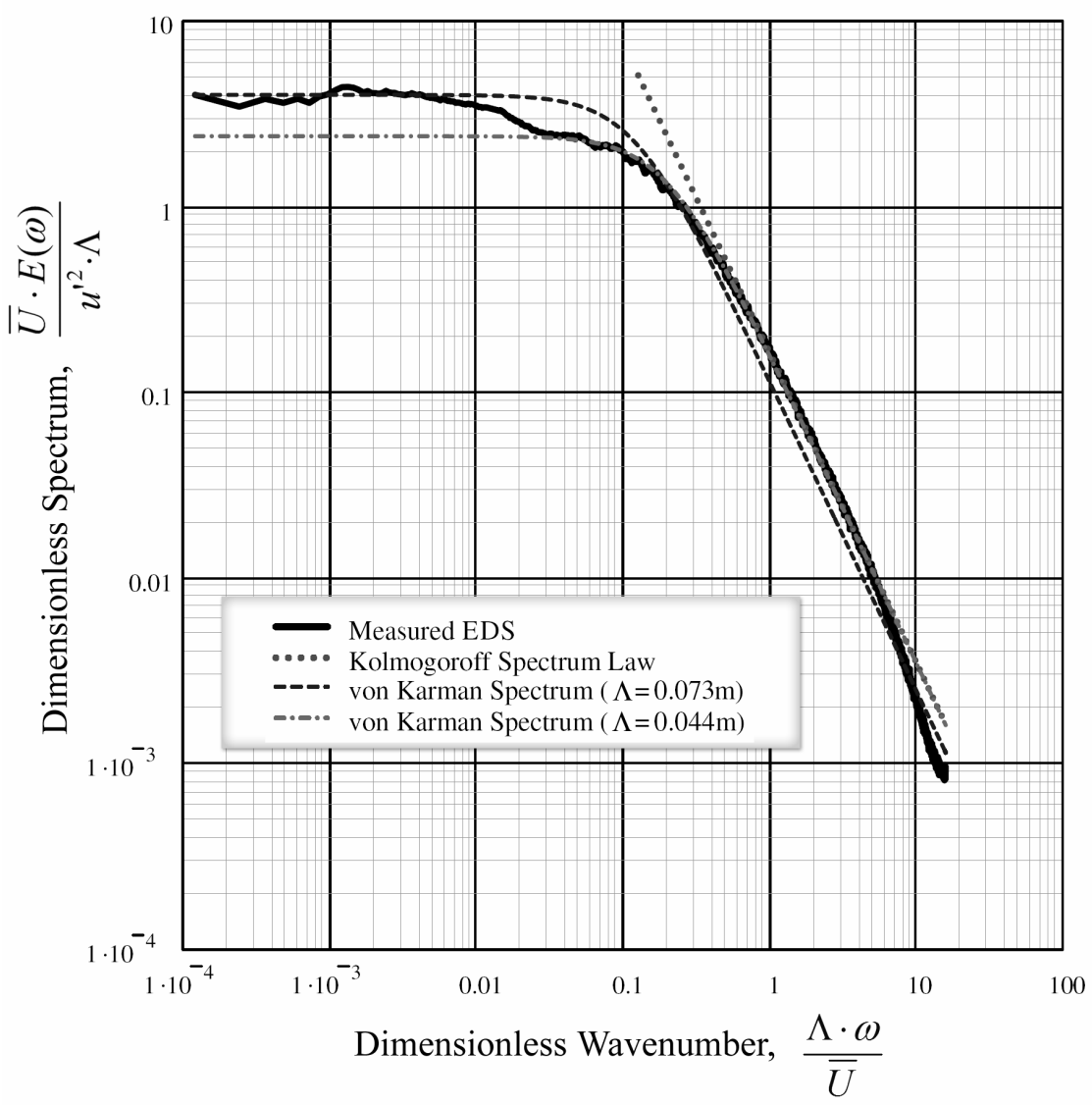

Figure 52. Approach Flow Energy Density Spectrum (x/C_{ax}=-0.58)

The approach flow EDS follows the Kolmogorov spectrum law (Eq. 4.10) fairly well in the higher frequency (wavenumber) range suggesting that an inertial subrange exists. Its existence is also confirmed through criteria given in Hinze [40] as $\mathrm{Re}_{Lu}^{3/8} >>> 1$ and $\mathrm{Re}_{\lambda}^{3/4} >>> 1$. These turbulence Reynolds numbers are based on the energy length scale and the dissipation rate and are tabulated below in Table 4.

The EDS is also compared with two cases of von Kármán's interpolation formula (Eq. 4.11). The first case uses an integral length scale $(\Lambda = 0.073m)$ calculated from (Eq. 4.12) to evaluate the von Kármán spectrum. This Λ value forces the curve and data to

match as $\omega \to 0$ by definition. Beyond the very low wavenumbers however, the curve maintains a negative offset from the data. This disagreement is thought to be attributed to uncertainty in the calculation of Λ as data are scarce in the very low wavenumber range. This condition causes an increase in uncertainty of $E(\omega)$ as $\omega \to 0$. Further investigation would be required to improve understanding and verify repeatability of low frequency spectrum information. The second curve of the von Kármán spectrum is a "best fit" version which uses an integral length scale arrived at iteratively. Due to a smaller Λ value (0.044m) there is a deviation of the EDS at low wavenumbers. There is, however, a significant improvement seen from wavenumbers beyond 0.03. This finding suggests that the integral length scale may be lower than the one calculated using (Eq. 4.12). Again, this is likely due to the amount of data available as $\omega \to 0$.

Given the approach flow EDS, several turbulence properties can be approximated through calculation as outlined in Section 4.2.3. These quantities are given in Table 4. In general, the integral and energy length scales calculated corroborate the assumption that large eddies exist in the approach flow. The largest of which appear to be around 10% of the blade chord length. Values of the integral length scale Λ are given as a range in Table 4 due to the findings described above pertaining to the energy density spectrum. The ratio of Lu/Λ appears to be reasonable as the theoretical ratio equals 2.37 according to Ames and Moffat [44].

Table 4. Approach Flow Turbulence Properties

Bulk Properties		**Turbulence Properties**			
Re_c:	430,000	Λ / C:	0.08 - 0.13	Re_{Lu}:	11,300
u':	1.6 m/s	Lu / C:	0.190	Re_λ:	340
Tu:	14%	ε:	32 m^2/s^3	Lu / Λ :	1.46 - 2.37

The turbulence information given within this section is useful in comparison to other turbulent flows, as well as Computational Fluid Dynamics turbulence models. It is applied as a computational boundary condition as described later in Chapter 8.

6.2.3 Temperature Field

Within this study there are two different approach flow temperature conditions. The base condition is simply that of a uniform temperature approach flow. The wind tunnel draws in ambient air which is not heated or cooled (beyond what is done by the fans) prior to entering the test section. This condition is used during all tests except where noted. Measurements made to verify the uniformity of the approach flow temperatures revealed maximum variations about the mean of ±0.2ºC.

The second approach flow temperature condition will be referred to as the "Heated Approach Flow" condition when referenced. This condition allows for the investigation of near-wall approach flow and leakage flow mixing effects. For all such cases, a small portion of the near-wall approach flow is heated prior to reaching the leakage flow slot. The transition duct (or stator lip) wall temperature, T_w, is controlled to be equal to the leakage flow temperature, T_ℓ. The locations of temperature measurement for T_w and T_ℓ are shown in Figure 53.

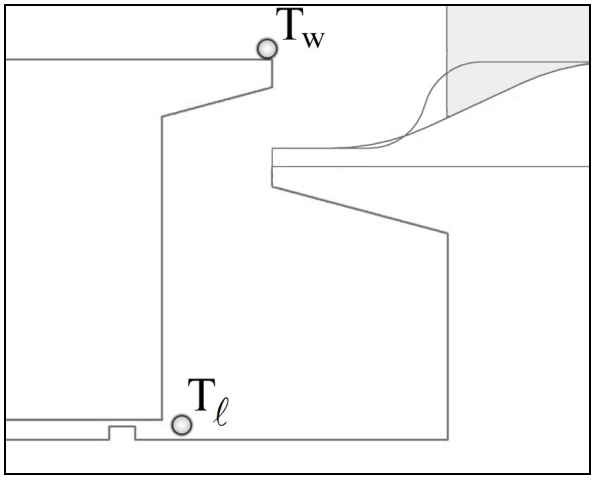

Figure 53. Approach Flow Wall and Leakage Temperature Measurement Locations

The leakage flow temperature (T_ℓ) is measured with several thermocouples and averaged at the leakage plenum's inlet (rim seal slot). The approach flow wall temperature is measured just upstream of the leakage exit flow slot (stator lip) at approximately $x/C_{ax} = -0.3$. Figure 54 shows the specific temperature profile created under this condition which is measured at mid-pitch and $x/C_{ax} = -0.4$. In this figure, the

referenced temperature T_∞ is "freestream" temperature located at mid-span and mid-pitch within the transition duct. The temperature profile is seen to be roughly uniform except for Span < 0.10. Within this region a thin layer of heated flow exists with the peak temperature (in the heated experiment case) located at the wall.

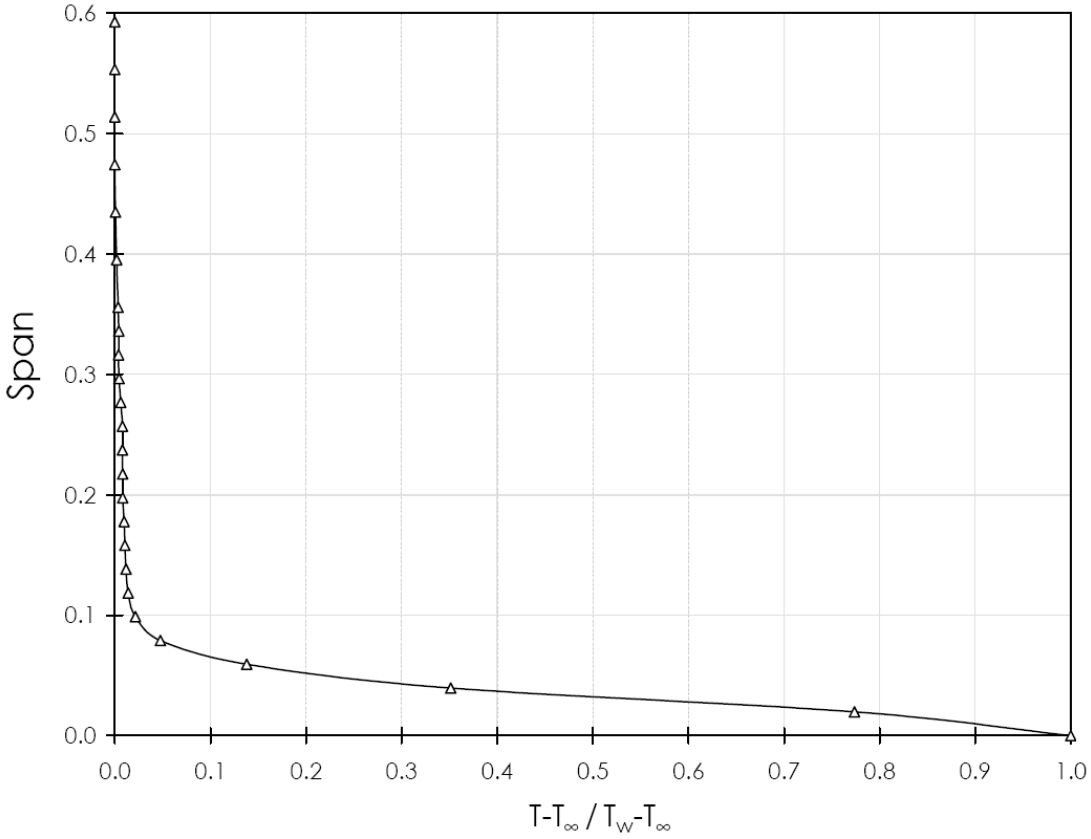

Figure 54. Approach Flow Spanwise Temperature Distribution

Chapter 7

Experimental Results and Discussion

7.1 Passage Aerodynamic Loss Results

7.1.1 Dolphin Nose Endwall Geometry at Three Leakage MFRs

Loss coefficient results for the dolphin nose endwall geometry are shown in Figure 55 through Figure 57. The presence of a boundary layer can be seen along the contoured endwall ($x/s = 0$). In all cases, the boundary layer appears to slightly thicken while traversing from the pressure wall to the suction wall. This is possibly due to cross-stream pressure gradients as well as the further streamwise distance traveled when nearer the suction wall. Blade pressure and suction surface boundary layers are seen in this plane ($y/p = 0$ and 1, respectively).

Two large loss cores may be seen near the suction surface at the exit plane for all three MFR cases. The lossy region near the flat endwall (right) appears higher in $C_{p,Loss}$ magnitude and remains closer to the endwall than its counterpart on the contoured endwall (left). This region, which is centered at (0.82, 0.85) is smallest for the case of 0.5% MFR and noticeably increases for the 1.0% and 1.5% MFR cases. The latter two cases appear to be nearly identical in this region. The loss core on the left (suction surface on the contoured endwall side) extends out into the passage to approximately 40% of span and appears slightly larger than the core on the right (nearer the flat endwall). It is difficult to distinguish any significant differences in this region between the three cases of differing MFR. It was initially thought that this region would increase in size with increasing leakage flow, due to entrainment. This appears not to be the case, or the change in leakage flow is too small to show significant differences. This finding suggests that there are not substantial differences in the aerodynamic penalty attributed to injecting leakage flow over the range 0.5%-1.5% MFR for the dolphin nose endwall geometry.

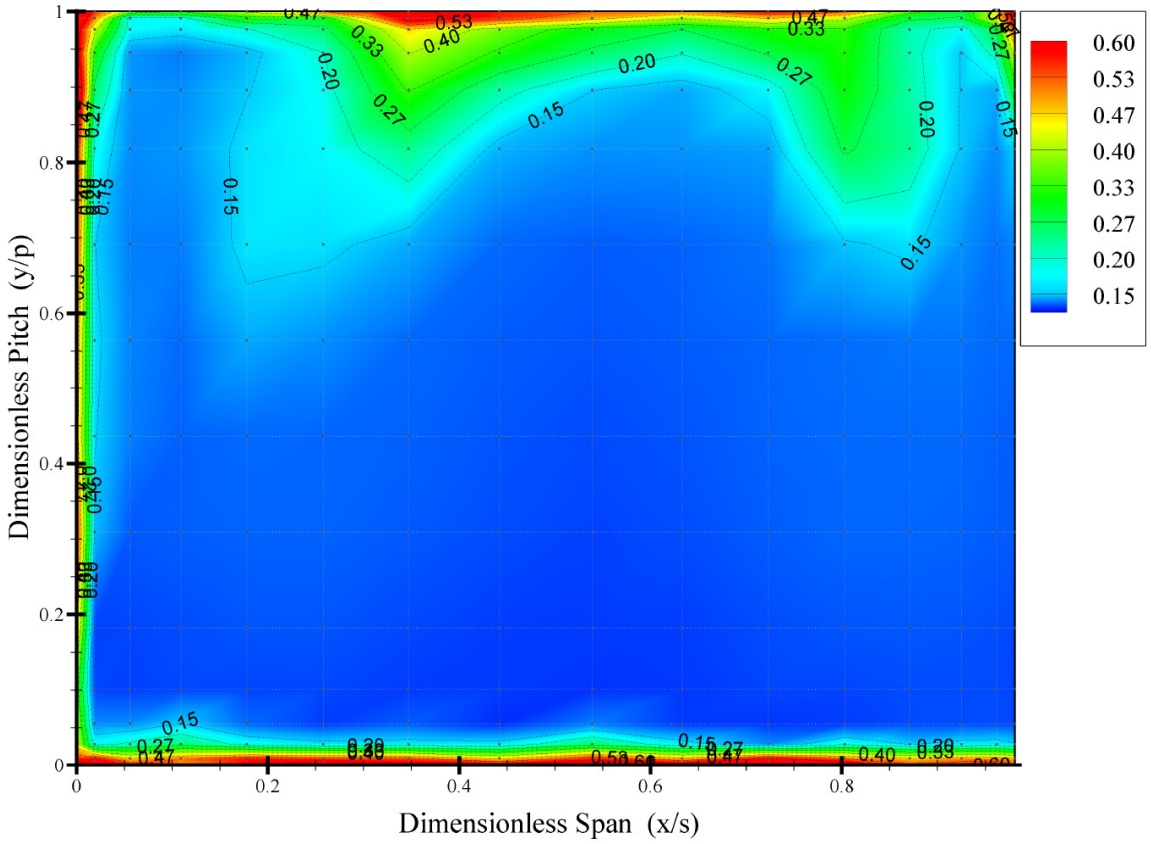

Figure 55. Passage Exit Plane Loss Coefficients for Dolphin Nose Endwall with 0.5% Leakage MFR. Contoured Endwall, x/s=0; Pressure Surface, y/p=0; Suction Surface, z/p=1.

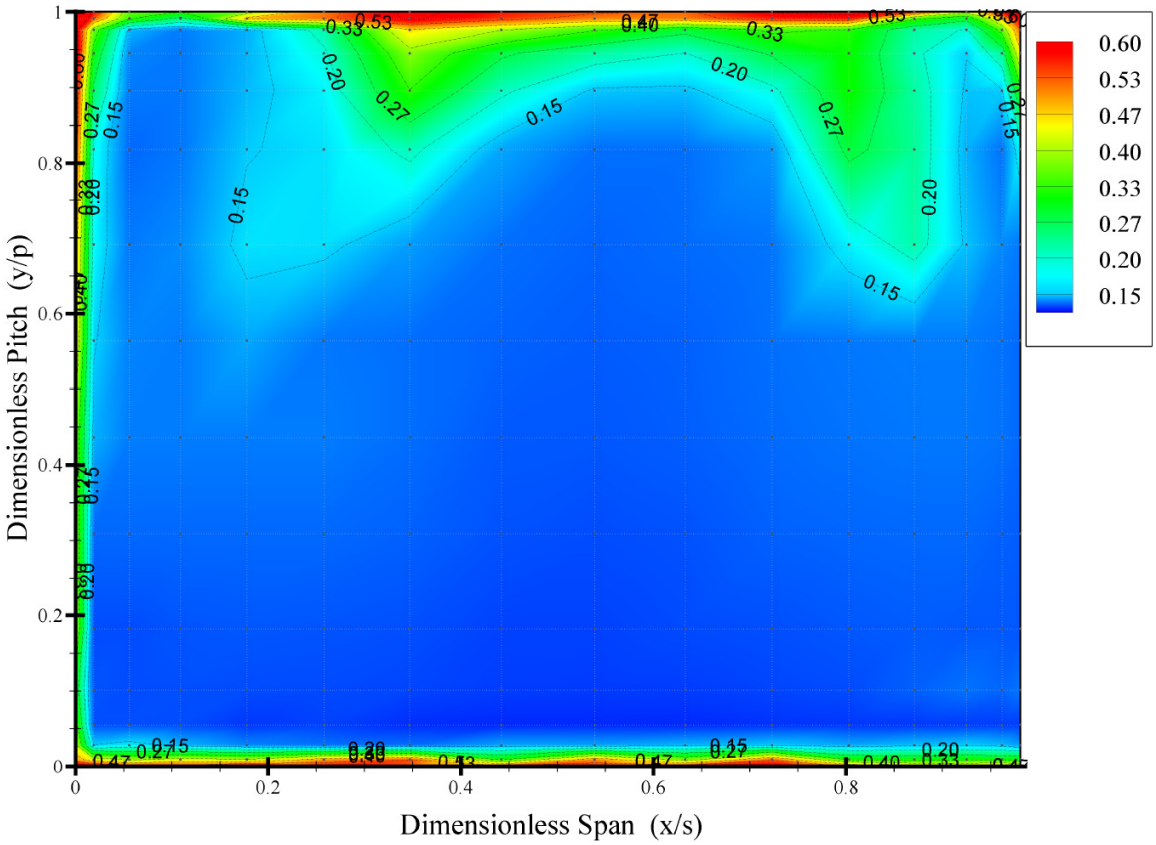

Figure 56. Passage Exit Plane Loss Coefficients for Dolphin Nose Endwall with 1.0% Leakage MFR. Contoured Endwall, x/s=0; Pressure Surface, y/p=0; Suction Surface, z/p=1.

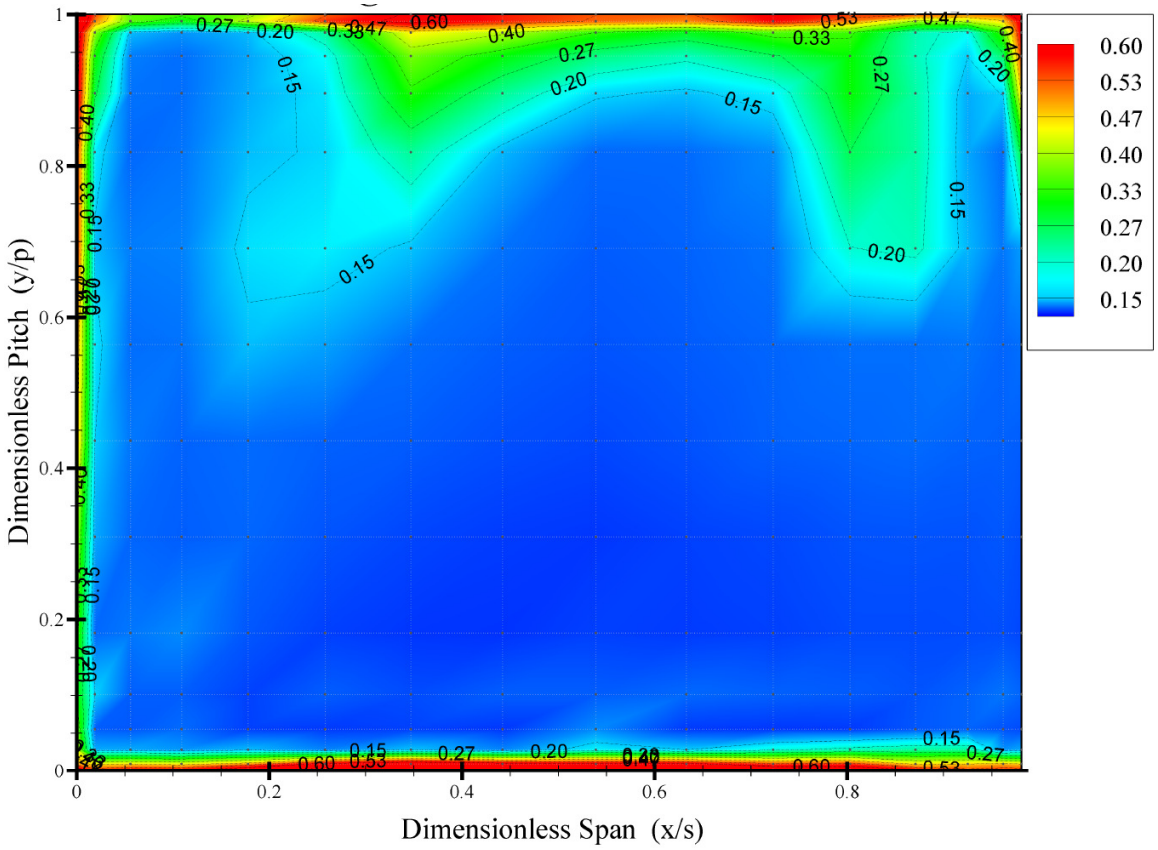

Figure 57. Passage Exit Plane Loss Coefficients for Dolphin Nose Endwall with 1.5% Leakage MFR. Contoured Endwall, x/s=0; Pressure Surface, y/p=0; Suction Surface, z/p=1.

7.1.2 Shark Nose Endwall Geometry at Three Leakage MFRs

Loss coefficient results for the shark nose endwall geometry are shown in Figure 58 through Figure 60 for leakage mass flow ratios of 0.5%, 1.0%, and 1.5%, respectively. These results display very similar features to one another and many areas are indistinguishable between leakage flow rate cases. This revelation allows for the cases to be discussed in a generalized manor.

As was the case with the dolphin nose results, boundary layers are viewable near the contoured endwall ($x/s = 0$) and blade trailing edges ($y/p =$ 0 and 1) for all cases. Another important feature is a loss core centered around (0.82, 0.85). This region of higher loss magnitudes is roughly the same size for all three leakage flow rate cases. Magnitudes seen within this loss core also show little variation between cases alluding to

independence of leakage flow rate. Both the location and magnitudes within this loss core appear indistinguishable from those seen in the dolphin nose endwall results.

A second loss core is present on the opposite side of the passage near the contoured endwall. This region is spread over a larger area than the loss core on the flat endwall side of the passage. It extends from 15 to 40% of span which is similar to that seen with the dolphin nose endwall geometry. The loss core also extends outward from the top blade's trailing edge to approximately $y/p = 0.5$. This distance is further out into the passage than the comparable loss core with the dolphin nose endwall geometry. These findings, along with the dolphin nose endwall results, suggest that there are not substantial differences in the aerodynamic penalty attributed to injecting leakage flow over the range 0.5%-1.5% MFR whether the endwall geometry be the dolphin nose or shark nose.

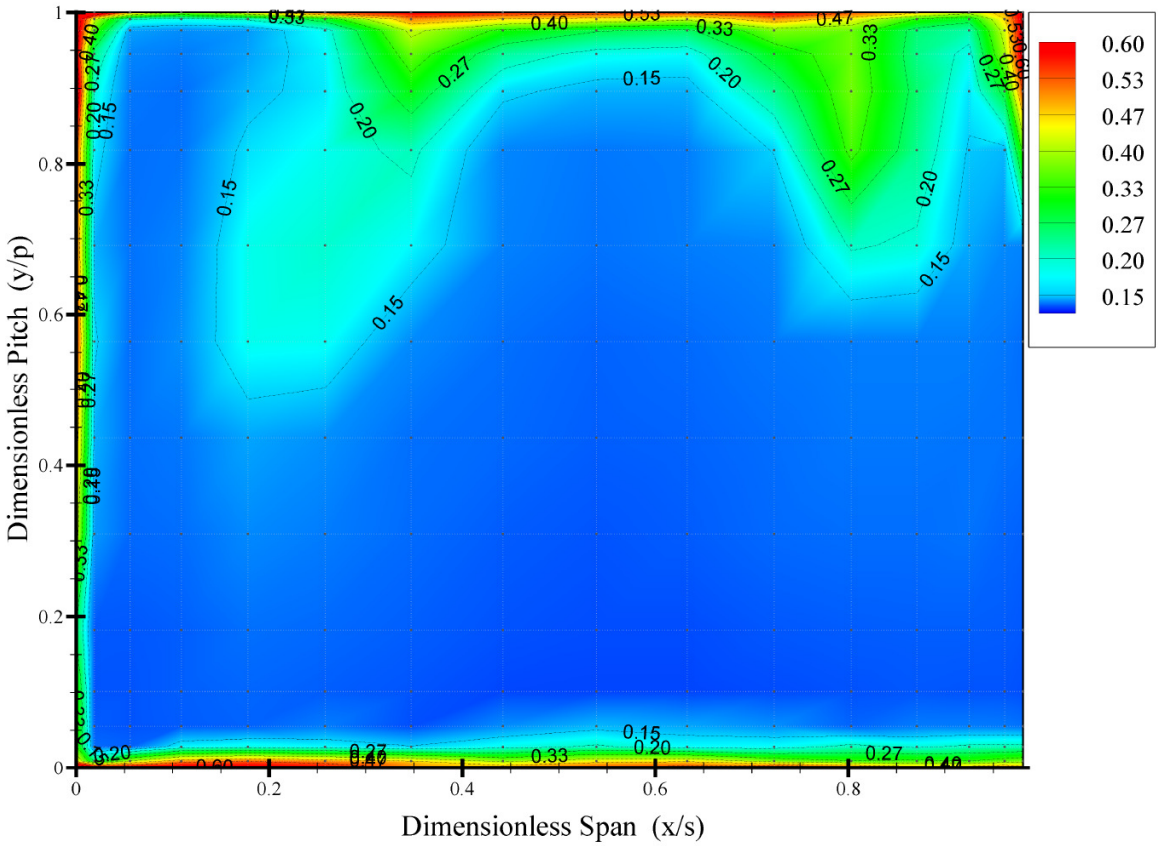

Figure 58. Passage Exit Plane Loss Coefficients for Shark Nose Endwall with 0.5% Leakage MFR. Contoured Endwall, x/s=0; Pressure Surface, y/p=0; Suction Surface, z/p=1.

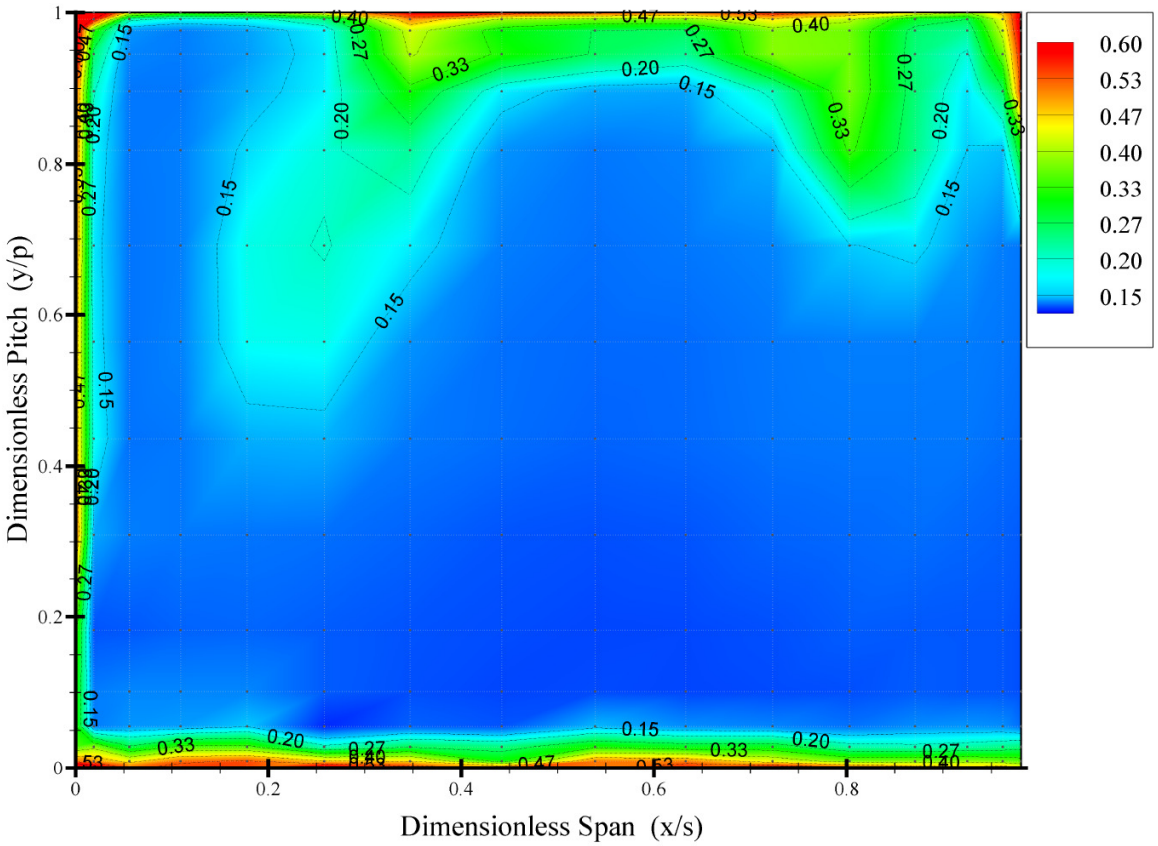

Figure 59. Passage Exit Plane Loss Coefficients for Shark Nose Endwall with 1.0% Leakage MFR. Contoured Endwall, x/s=0; Pressure Surface, y/p=0; Suction Surface, z/p=1.

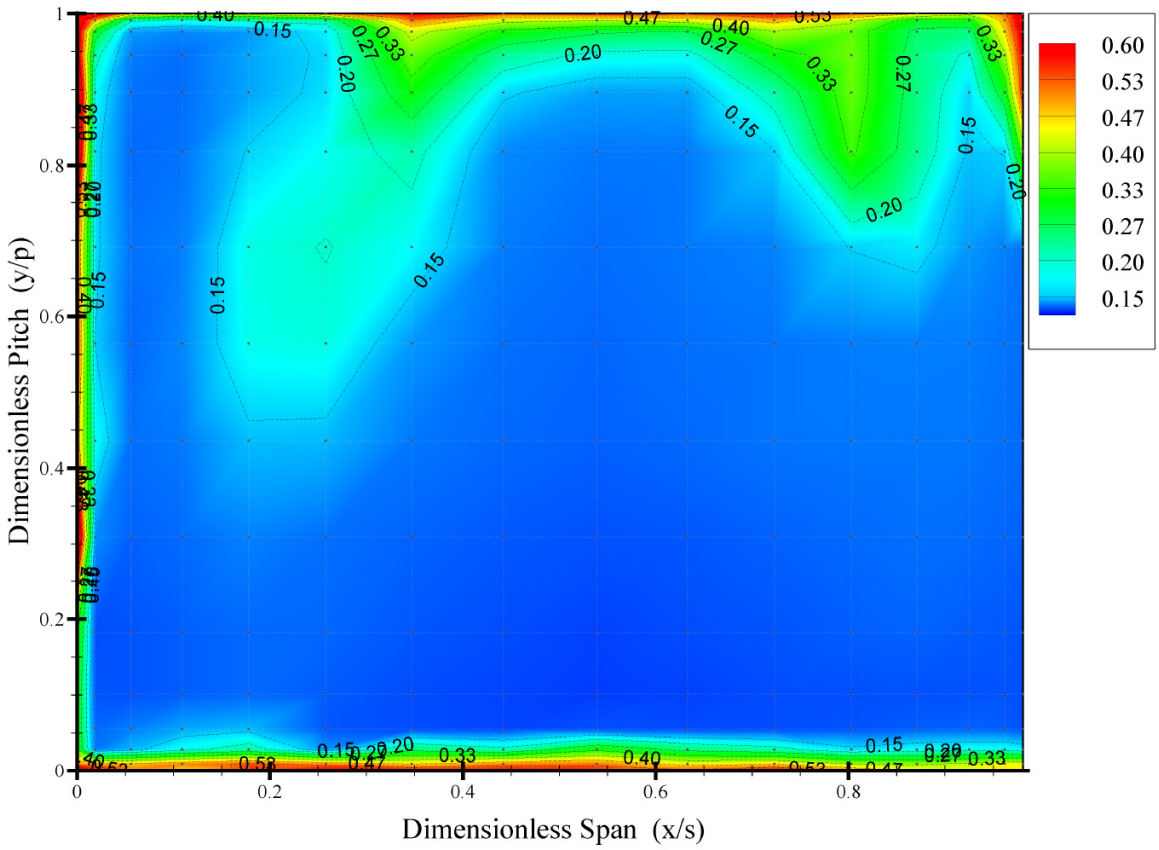

Figure 60. Passage Exit Plane Loss Coefficients for Shark Nose Endwall with 1.5% Leakage MFR. Contoured Endwall, x/s=0; Pressure Surface, y/p=0; Suction Surface, z/p=1.

7.1.3 Comparison of Dolphin Nose and Shark Nose Results

The purpose of this section is to build upon the comparisons between shark and dolphin nose endwall loss coefficient results previously made. As already stated, many pressure loss features appear independent of endwall contour and leakage flow rate. These include areas near blade trailing edges and endwall boundary layers. Small deviations in loss coefficient ($C_{p,Loss}$) do exist within these areas between test cases; however, they are likely attributable to small spatial errors in probe position compounded by strong gradients in total pressure. For this reason, the case-to-case variations in these areas should not be given significant focus. Some regions in the passage exit plane which show slight differences in $C_{p,Loss}$ magnitude between dolphin and shark nose cases can be identified, however. The first is part of the passage vortex system centered at

approximately $\left(\frac{x}{s},\frac{y}{p}\right)=(0.25,0.57)$ which has lifted off of the contoured endwall and up the blade's suction side. When comparing this area between shark and dolphin nose endwall results, it is seen that loss coefficients are approximately 0.05 higher for the shark nose cases (regardless of leakage flow rate). As a practical consideration, however, this difference in loss coefficient between cases of different endwalls is very small and likely not of considerable importance.

Other regions on the exit plane exist where there are small but noticeable differences in loss coefficient results between cases. Interestingly, these areas do not represent consistent trends with respect to endwall contour over the range of leakage flow rates investigated. One region, for example, is centered at approximately $\left(\frac{x}{s},\frac{y}{p}\right)=(0.45,0.92)$ which is close to the passage's suction side. For the cases of leakage flow rate equal to 0.5% and 1.5%, small but noticeably higher loss coefficients exist in this area when the dolphin nose endwall contour is tested. Maximum deviations between the shark nose and dolphin nose cases appear to be around 0.08 in this region. For a leakage flow rate of 1.0%, however, there appear to be no discernable differences due to endwall shape. This lack of coherent trends between test results prevents one from making concrete conclusions regarding losses in this region and the effect of leakage flow rate and endwall contour. Another one of the regions that displays mild differences with endwall shape is centered at $\left(\frac{x}{s},\frac{y}{p}\right)=(0.8,0.82)$. Loss coefficient values in this area are as much as 0.08 higher in the shark nose endwall contour cases for 0.5% and 1.5% leakage MFR. Smaller sensitivity to contour is seen for the 1.0% leakage MFR case. It may be that many of these areas arise simply due to measurement variability. The prevailing conclusion, however, is that differences in loss coefficients between endwall contours and leakage flow rates are small. The uncertainty in loss coefficient reported is 5%.

7.1.4 Mass Averaged Loss Coefficients at Exit Plane

Mass averaged loss coefficients are calculated from pressure loss data in the previous sections. This process of mass averaging gives greater importance to pressure losses in areas of high mass flux. The mass averaged loss coefficient, $\overline{C}_{p,Loss}$, is defined in (Eq. 7.1).

$$\overline{C}_{p,Loss} = \frac{\int_0^{Span}\int_{S-side}^{P-side} C_{p,l} \cdot u \cdot dzdy}{\int_0^{Span}\int_{S-side}^{P-side} u \cdot dzdy} \qquad \text{(Eq. 7.1)}$$

Mass averaged coefficients for the six measured cases at the exit plane are reported in Table 5. It is again stated that these measurements are made in the exit plane between $0 \le x/s \le 0.98$, and therefore do not include boundary layer losses on the flat endwall ($x/s = 1$). By referring to Table 5, one can see that the endwall contour shape appears to have an effect on the $\overline{C}_{p,Loss}$ coefficient. The average $\overline{C}_{p,Loss}$ value measured with the dolphin nose contour in place is 0.1309, while the average shark nose value is slightly higher at 0.1399. This amounts to a 7% average increase in $\overline{C}_{p,Loss}$ when changing from the dolphin nose endwall contour to the shark nose contour. Another parameter to consider is the effect of leakage mass flow rate on $\overline{C}_{p,Loss}$ values. In general, variations in leakage mass flow rate between 0.5-1.5% MFR appear to have little effect on the $\overline{C}_{p,Loss}$ coefficient. Dolphin nose endwall cases vary between ±0.5% of the mean, while shark nose endwall cases vary within ±1.5% of the mean. These variations due to leakage mass flow rate should not be considered significant.

Table 5. Mass Averaged Loss Coefficient at Exit Plane for Cases Tested

Endwall Contour	Leakage Mass Flow Ratio 0.5%	1.0%	1.5%
Dolphin	0.1313	0.1304	0.1311
Shark	0.1391	0.1420	0.1387

Another way to look at the mass averaged loss coefficient results is to consider the exit plane to be made up of different imaginary "segments." In the case considered here,

one segment which contains all of the losses which arise in the "contoured endwall side" of the passage, and those in the "flat endwall side" of the passage. The exit plane area defined to be the "contoured endwall side" is $0 \le x/s \le 0.58$. It extends past the blade midspan because the loss core on this side of the passage has lifted off from the contoured endwall more than the loss core on the other side of the passage. The remaining area, $0.58 < x/s \le 0.98$, is then defined to be the "flat endwall side" of the exit plane. The mass averaged loss coefficients are calculated the same as before, however, the integral limits are now changed to account for the different areas considered. The $\overline{C}_{p,Loss}$ coefficient results for these two exit plane "segments" are reported in Table 6.

Table 6. Mass Averaged Loss Coefficients for Separated Exit Plane

Endwall Contour	Contoured Endwall Side 0 ≤ x/s ≤ 0.58			Flat Endwall Side 0.58 < x/s ≤ 0.98		
	Leakage Mass Flow Ratio			Leakage Mass Flow Ratio		
	0.5%	1.0%	1.5%	0.5%	1.0%	1.5%
Dolphin	0.1339	0.1298	0.1315	0.1275	0.1312	0.1305
Shark	0.1371	0.1426	0.1384	0.1421	0.1411	0.1392

By reviewing the data in Table 6, one can see that for a given endwall contour, $\overline{C}_{p,Loss}$ values remain fairly consistent between exit plane segments. In fact, neither the results on the contoured side nor the flat endwall side are consistently higher or lower than the other. This reveals that any variations in loss coefficient due to changes in flow parameters are occurring fairly uniformly across the exit plane. The same conclusion as stated earlier, that the shark nose endwall contour results in slightly higher loss coefficients, is still shown to hold true regardless of the exit plane segment considered.

7.2 Passage Temperature Field Results

Results of passage thermal field measurements are given in the following sections. Both the dolphin nose and shark nose endwall contour geometries were measured with leakage mass flow ratios (MFR) of 0.5%, 1.0%, and 1.5% for a total of six cases. Further details regarding the measurements and procedure are given in Section 5.2.

7.2.1 Dolphin Nose Endwall Geometry at Three Leakage MFRs

Results for passage temperature fields with the dolphin nose endwall geometry are shown in Figure 61, Figure 62, and Figure 63. All three plots exhibit similar features which will be discussed herein. Firstly, the most upstream plane ($x/C_{ax} = -0.296$) displays a maldistribution in temperature for all cases. The highest temperatures are seen at the left side of this plane and steadily decrease moving rightward. The maldistribution reduces as the leakage flow rate is increased. The occurrence of lower temperatures near the leakage slot suggests that mainstream fluid may be entering the leakage plenum and mixing with the heated leakage flow. Additionally, the pressure field near the stagnation region of the right blade already appears to be skewing the leakage flow towards the suction side of the passage. These two discussion points possibly explain why the leakage slot experiences this maldistribution.

Another similarity in the three data sets is the path and measured profile shape of the leakage fluid as it is traced through the passage. Changing the leakage flow rate in the range of 0.5-1.5% MFR appears to have no major effect on the fluid mechanics; thus position within passage. Dispersion effects are not noticeably different. At all three flow rates, the leakage fluid is quickly swept across the endwall and upwards on the suction side of the passage. These observations suggest that the momentum of the leakage flow exiting the slot is simply too small to compete with the cross-stream passage gradient in the endwall region. This is also related to the low pressure of the passage vortex as it sweeps across the endwall; effectively creating a boundary where leakage flow cannot pass. One important observation of the leakage flow path, is that as the fluid is swept across the passage it remains directly above the endwall. The contact between leakage fluid and the endwall reveals that it does provide cooling coverage.

Although the leakage flow path does not appear to be affected by flow rate, the recovery temperature magnitude is affected. Simply stated, a higher flow rate provides an increase in endwall cooling coverage magnitude just by virtue of more cooling fluid being delivered. This is seen as a gradual increase in temperature on all planes when comparing results of leakage MFR's 0.5%-1.5% in order.

At a location just slightly downstream of the $x/C_{ax} = 0.44$ plane, the leakage flow completely lifts off of the endwall surface providing cooling value only on the blade suction side surface. This "lifting" action is apparent in the $x/C_{ax} = 0.44$ plane already as the location of highest temperature begins to rise off of the endwall. At the final passage measurement plane $(x/C_{ax} = 0.92)$, dispersion due to the mainstream turbulence level and passage vortices has caused much of the leakage flow to mix out, leaving very low concentrations. The maxima at this location lies on the blade suction side surface at approximately 30% span. This corresponds quite well with the exit plane pressure loss measurements for the dolphin nose endwall geometry given in Figure 55, Figure 56, and Figure 57. A large loss core is seen in all three data sets to be centered at approximately z/s=0.3. It can be concluded from the two types of measurements that this is the location of passage vortices which entrain much of the leakage flow.

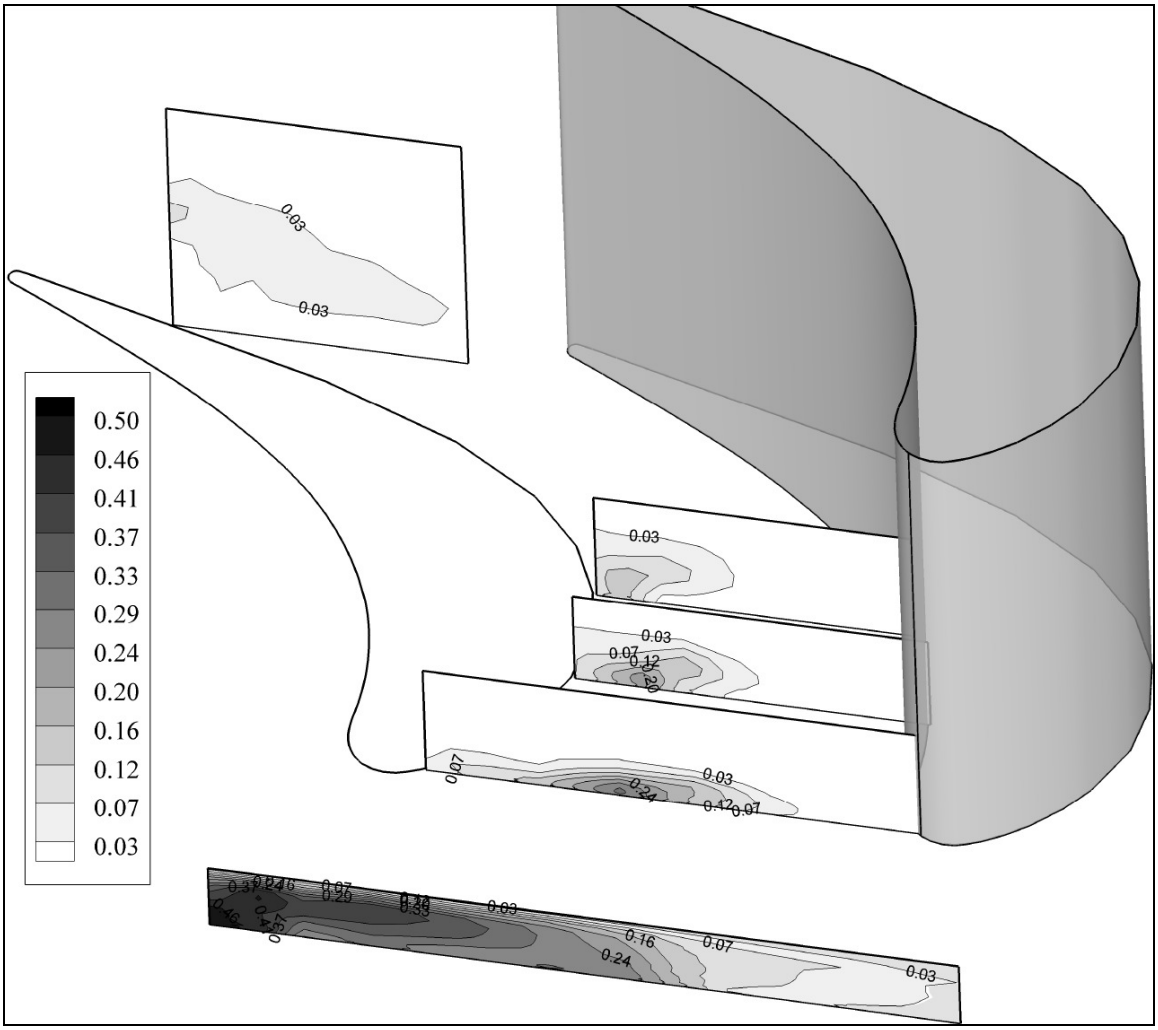

Figure 61. Passage Temperature Fields for Dolphin Nose Endwall at 0.5% Leakage MFR

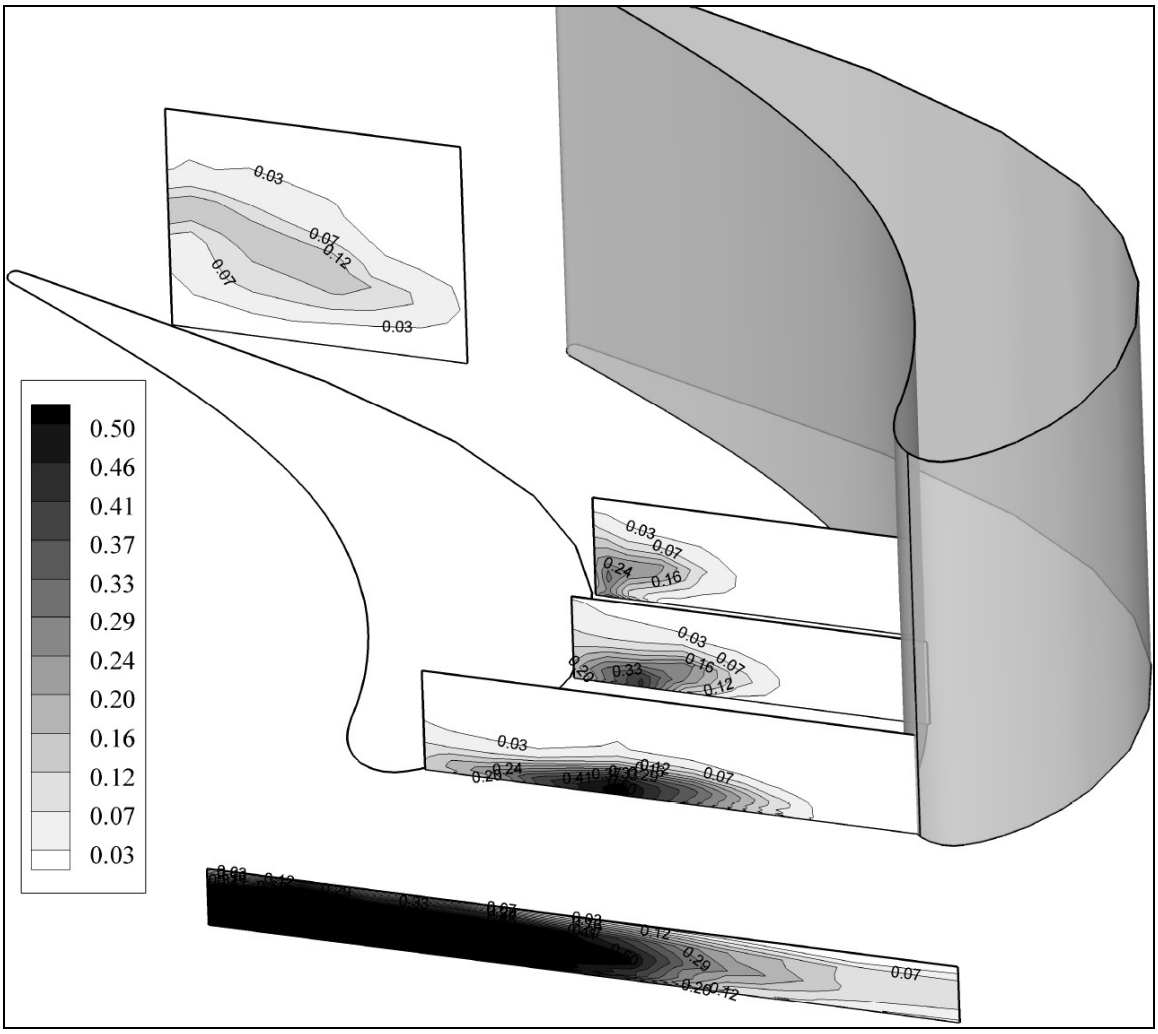

Figure 62. Passage Temperature Fields for Dolphin Nose Endwall at 1.0% Leakage MFR

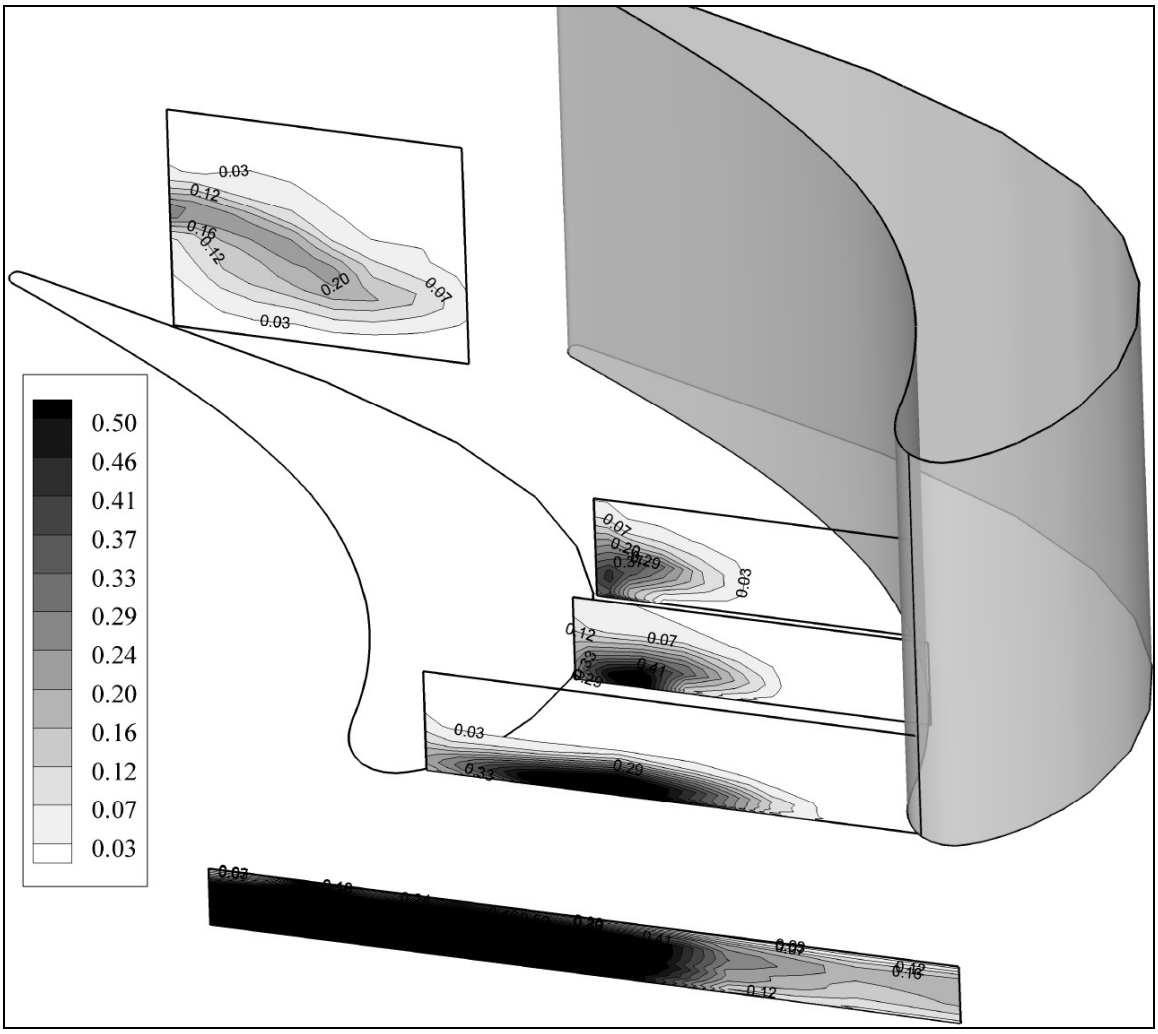

Figure 63. Passage Temperature Fields for Dolphin Nose Endwall at 1.5% Leakage MFR

7.2.2 Shark Nose Endwall Geometry at Three Leakage MFRs

Results for passage temperature fields with the shark nose endwall geometry are shown in Figure 64, Figure 65, and Figure 66 for leakage mass flow ratios of 0.5%, 1.0%, and 1.5%, respectively. Many of the flow features exhibited in the shark nose endwall data are similar to those with the dolphin nose endwall. Again present is a temperature maldistribution at the leakage flow slot $(x/C_{ax} = -0.296)$. As the leakage flow rate is increased the distribution at this slot improves; although a uniform distribution is never

achieved. The leading edge plane $(x/C_{ax} = 0)$ for the shark nose endwall data is at a lower elevation than that of the dolphin nose. This is due to the difference in surface contours. The maximum temperature at this plane occurs at approximately $y/C_{ax} = 0.56$ for the case of leakage MFR=0.5%. As the leakage flow rate is increased, the area of maximum temperature extends horizontally over the endwall surface. As this area of high temperature extends, it favors the suction side of the passage. One observation of importance is that the area of highest temperatures appears to be slightly elevated off of the endwall surface for all three leakage flow rates cases. This results in decreased cooling coverage of the endwall by the leakage fluid.

The measurement plane at $x/C_{ax} = 0.247$ shows leakage fluid migrating toward the passage suction side and diminishing in temperature. At this passage location, the temperature maximum is very near the corner formed by the blade and endwall. Moving slightly downstream to $x/C_{ax} = 0.44$, the area of maximum temperature appears to begin moving up the blade's suction side surface. This movement leaves very little endwall cooling coverage at the $x/C_{ax} = 0.44$ plane. The final measurement plane at $x/C_{ax} = 0.92$ reveals that most of the leakage fluid has been mixed out to a point where it cannot be detected. This is the case with the lowest leakage flow rate. As the leakage flow rate is increased, the fluid may be identified on this plane. The fluid appears to have mixed out within the passage and exists in a horizontal band between 10-30% span.

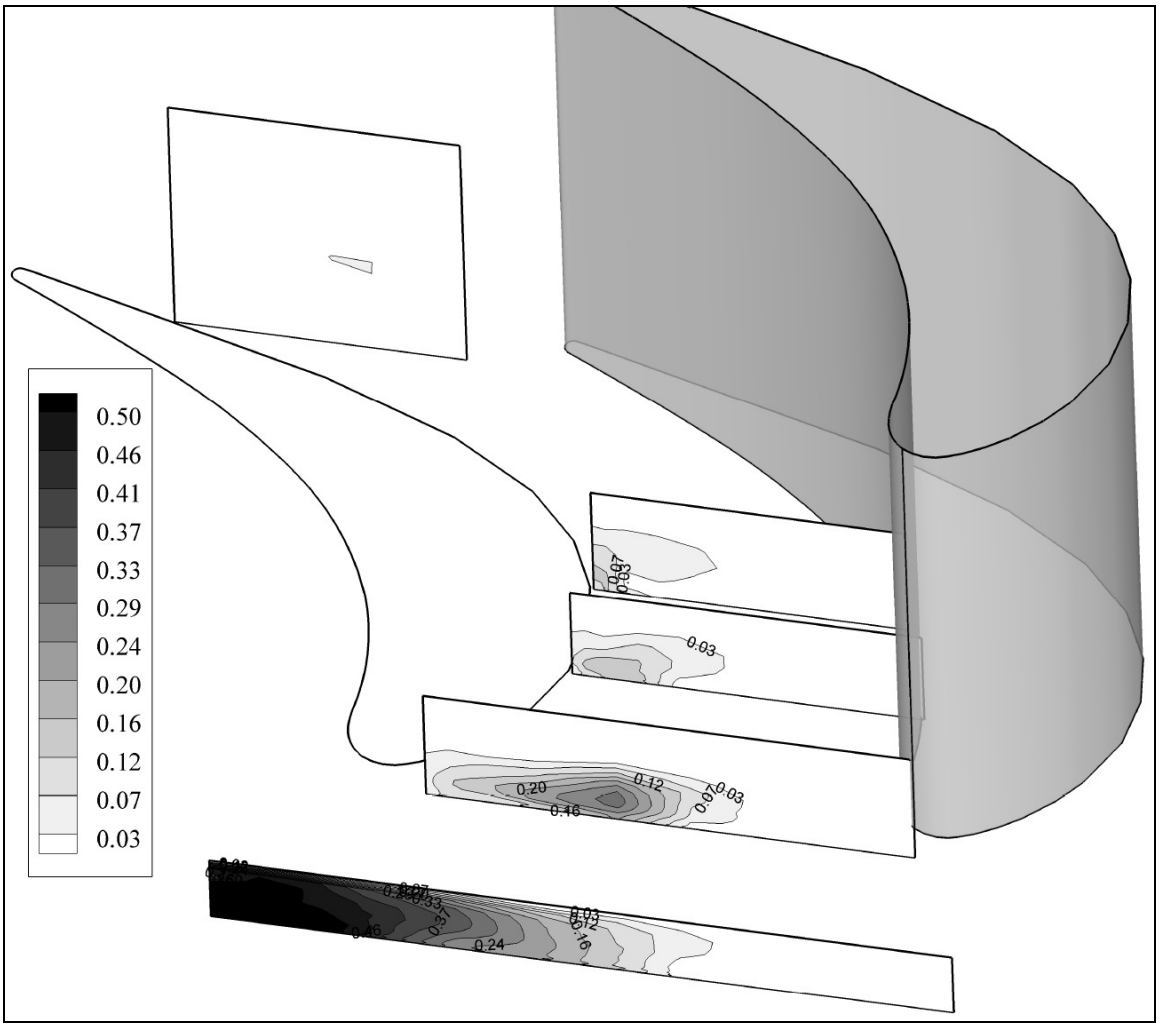

Figure 64. Passage Temperature Fields for Shark Nose Endwall at 0.5% Leakage MFR

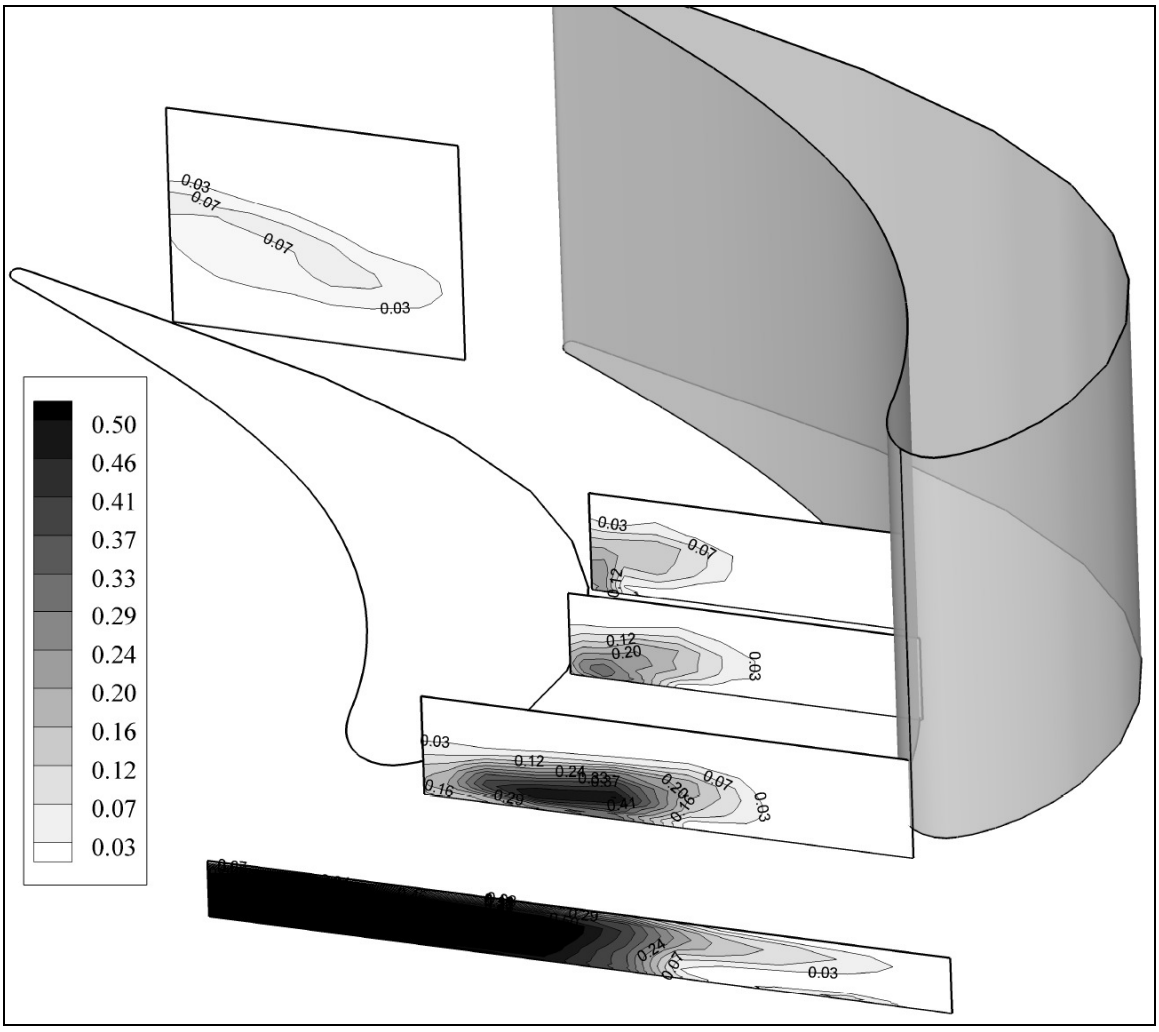

Figure 65. Passage Temperature Fields for Shark Nose Endwall at 1.0% Leakage MFR

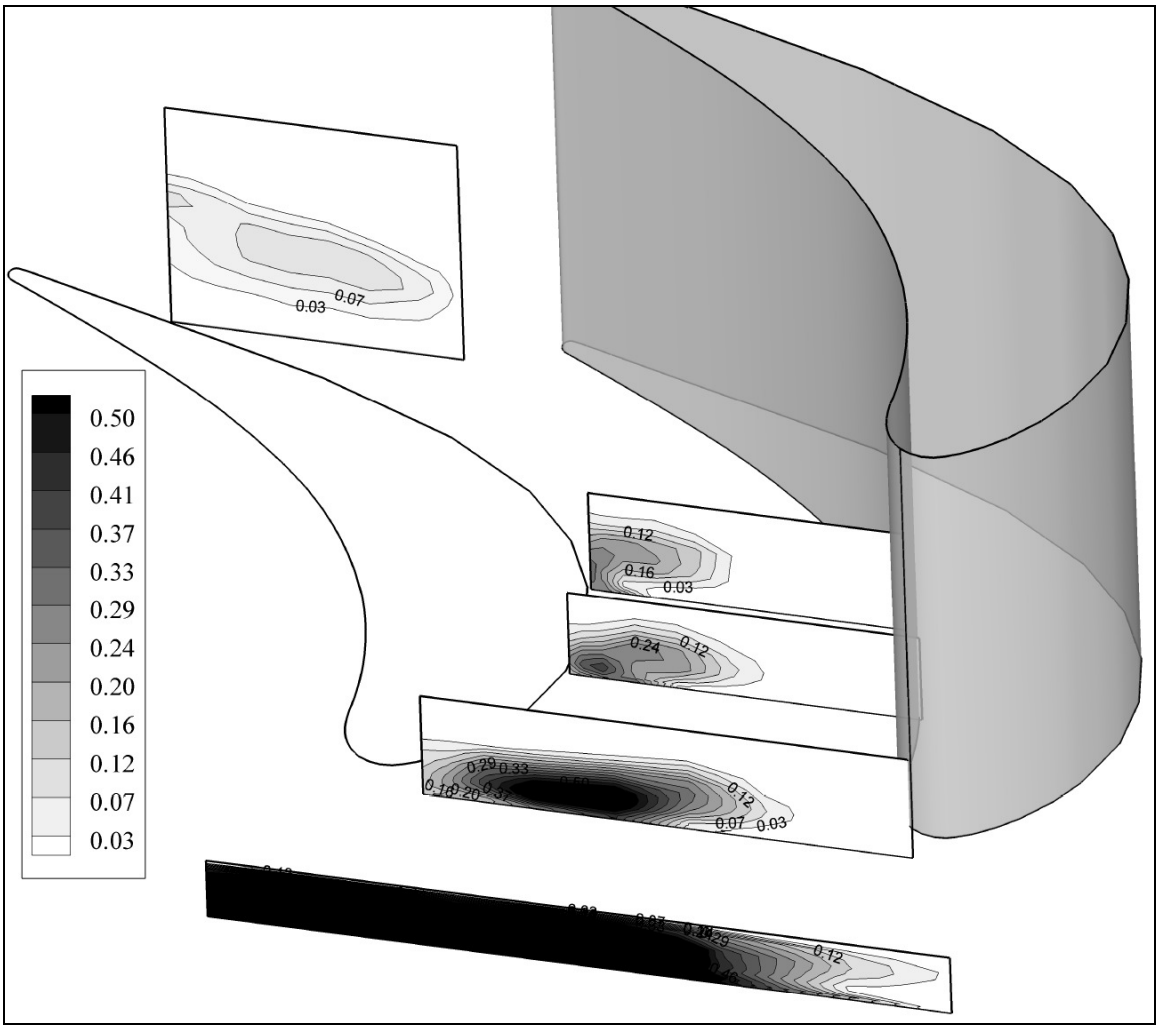

Figure 66. Passage Temperature Fields for Shark Nose Endwall at 1.5% Leakage MFR

7.2.3 Comparison of Dolphin Nose and Shark Nose Endwall Results

When comparing passage thermal field data for both the dolphin and shark nose endwalls, there are a few observations that can be discussed. The first finding is independent of endwall contouring considerations and relates to the leakage flow slot temperature distribution and the possibility of mainstream flow ingression. It was initially found that a lower temperature fluid was being delivered through the leakage cavity slot near the center blade stagnation region than at other locations along the slot. Monitoring the temperatures at several locations within the leakage plenum, as well as reviewing the passage temperature field data sets revealed this trend for all leakage flow cases. Since a

fairly uniform temperature is being injected into the leakage plenum along the rim seal slot (as monitored by measurements), the only reason a drop in recovery temperature should occur within the plenum is due to mainstream flow ingression (recall that the leakage flow is heated in the test). The driving force behind the suspected ingression is possibly the presence of the downstream blade and its effects on the local pressure field. This is not evident at the same relative location near the upper blade, indicating a less than ideal periodicity from one passage to the next. This is the product of having only two passages and having a flow delivery passage that is so sensitive to downstream conditions. If the leakage slot velocity were higher in the mixing zone, this would not be so aperiodic. The film cooling coverage upstream of the center blade leading edge is more reliable than the values upstream of the upper blade leading edge.

Another important observation which is contour dependent relates to endwall cooling coverage provided by the leakage fluid. It appears that for the shark nose endwall cases, leakage fluid is slightly displaced away from the endwall surface at the leading edge plane. By displacing the leakage flow away from the endwall surface, its utility has been significantly diminished. This "leakage flow displacement" behavior is not visible in any of the dolphin nose endwall results. The cause for this discrepancy is unknown, however, speculated to be due to the surface contour itself. The dolphin nose endwall incorporates strong curvature, thus acceleration profile. The shark nose curvature, however, should lead to a relatively weaker acceleration of its boundary layer. This boundary layer could be assumed thicker than its dolphin nose counterpart due to less acceleration, thus displacing the leakage flow away from the endwall surface more. If the cause of this discrepancy is indeed geometry dependent, it suggests that the dolphin nose endwall contour is superior with respect to heat transfer considerations on the endwall.

Another noticeable difference between the data sets are the temperature magnitudes. The dolphin nose endwall data appears to have higher peak temperatures on planes $x/C_{ax} = 0.247,\ 0.44,\ and\ 0.92$. This possibly reveals that the leakage flow is being mixed out faster, thus diminishing the temperature, with the shark nose endwall geometry. In general, however, temperature profiles on these measurement planes do not differ significantly in shape and size. This may suggest that dispersion of the leakage

flow is affected little by the endwall contour. These two arguments focusing on temperature magnitudes and profile shapes seem to disagree with eachother.

7.3 Endwall Adiabatic Film Cooling Effectiveness Results

Results of endwall adiabatic film cooling effectiveness measurements are given in the following sections. Measurements were made with both the dolphin nose and shark nose endwall contour geometries at leakage mass flow ratios (MFR) of 0.5%, 1.0%, and 1.5% for a total of six cases. These six cases are considered the baseline measurements as they were made with a uniform wind tunnel approach flow temperature. Also included in this section are measurement results which incorporate a non-uniform, or "heated" approach flow temperature distribution. This temperature distribution is fully described in Section 6.2.3. Essentially, it is a thermal boundary layer in the flow which is approaching the test endwall. The two types of data sets are compared, yielding information on how the approach flow temperature profile can affect endwall adiabatic film cooling effectiveness values. Complete details regarding the measurement procedures are given in Section 5.3.

7.3.1 Dolphin Nose Endwall Geometry at Three Leakage MFRs

Dolphin nose endwall adiabatic effectiveness values in cases with a uniform temperature approach flow are reported in Figure 67, Figure 68, and Figure 69 for leakage mass flow ratios of 0.5, 1.0, and 1.5%. In analyzing the three data sets, one sees the improved cooling coverage provided by increasing the leakage flow rate. That is, effectiveness magnitudes increase as leakage flow rate increases, though the cooling "pattern" does not differ strongly. Another general observation is that near-zero effectiveness values exist within the passage beyond the streamwise position of $x/C_{ax} = 0.6$. This finding reveals that all of the leakage flow has been removed from the endwall by mechanisms likely related to endwall secondary flows (i.e. passage vortex entrainment and cross-stream pressure gradient) regardless of leakage flow rate. The effect of cross-stream pressure gradient is also quite apparent upstream of the leading edge plane as leakage flow is

skewed toward the passage suction side. These general observations are expected and agree with results of many other studies on the topic [e.g. Pau et al. 2008].

Additionally, in all three data sets a local peak increase in endwall adiabatic effectiveness occurs at approximately $x/C_{ax} = 0$ and $y/C_{ax} = 0.6$. This rise in effectiveness is quite apparent in reviewing the contour plots as it stands out within the surrounding data which, in general, decreases with streamwise distance. This region of increased effectiveness appears to be dependent on leakage flow rate as the peak-to-trough difference becomes larger when the flow rate is increased from 0.5% to 1.5% MFR. The dependence of this feature on endwall contouring cannot be established from these data sets alone as they share the same endwall geometry. The fact that it increases with leakage flow rate does, however, suggest that it may depend on boundary layer thickness, acceleration, or impingement. Further measurements with the shark nose endwall geometry will provide more information on differences caused by contouring.

A third observation, valid for all three leakage MFR's is the lower cooling coverage near the blade suction side-to-endwall corner in the first half of the passage. This is seen as lower effectiveness values from the airfoil leading edge on downstream in the airfoil-to-endwall corner. The feature is difficult to see at a leakage MFR of 0.5% as there is little cooling coverage in neighboring areas. One plausible explanation for the ineffective cooling coverage in this region for all three flow rates is that the suction-side leg of a horseshoe vortex is preventing leakage flow from entering this area. At some downstream location, the horseshoe vortex and endwall boundary layer flow tend to rise off the endwall, in which case leakage flow would be able to reach the corner. This may be, since the effectiveness does increase in the suction side-to-endwall corner further downstream at approximately $x/C_{ax} = 0.4$.

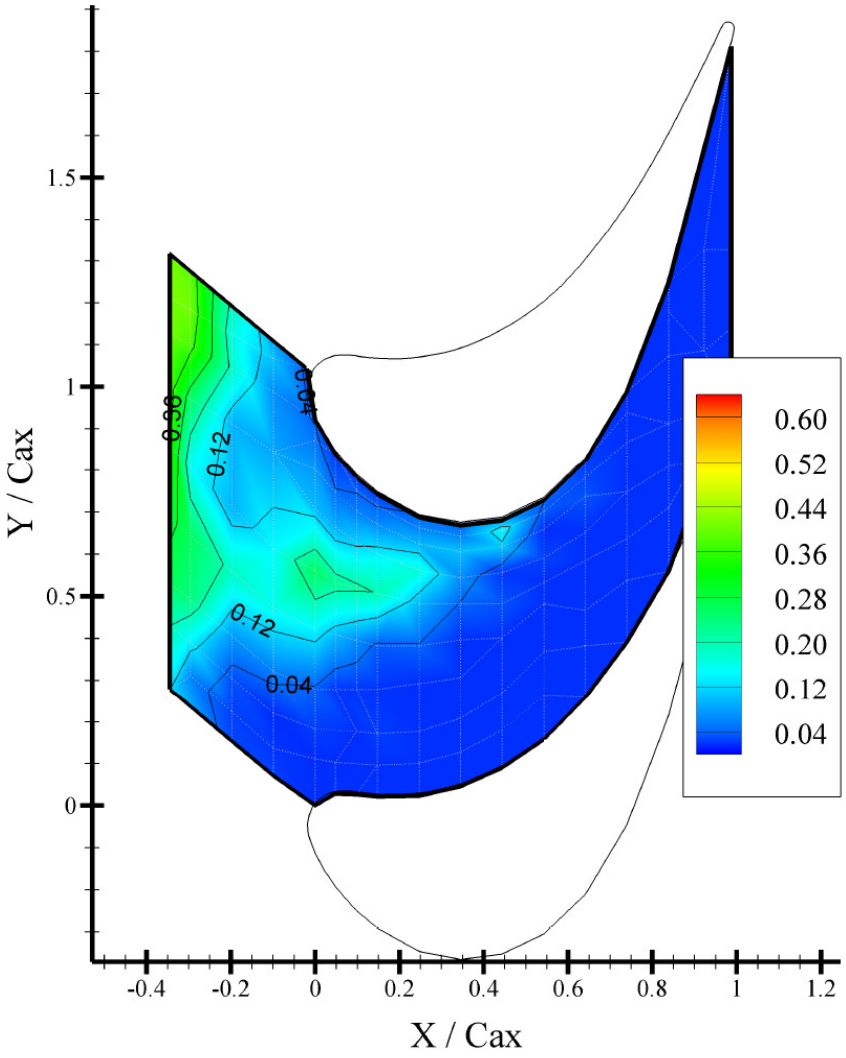

Figure 67. Endwall Adiabatic Film Cooling Effectiveness Contours for Dolphin Nose Endwall with 0.5% Leakage MFR

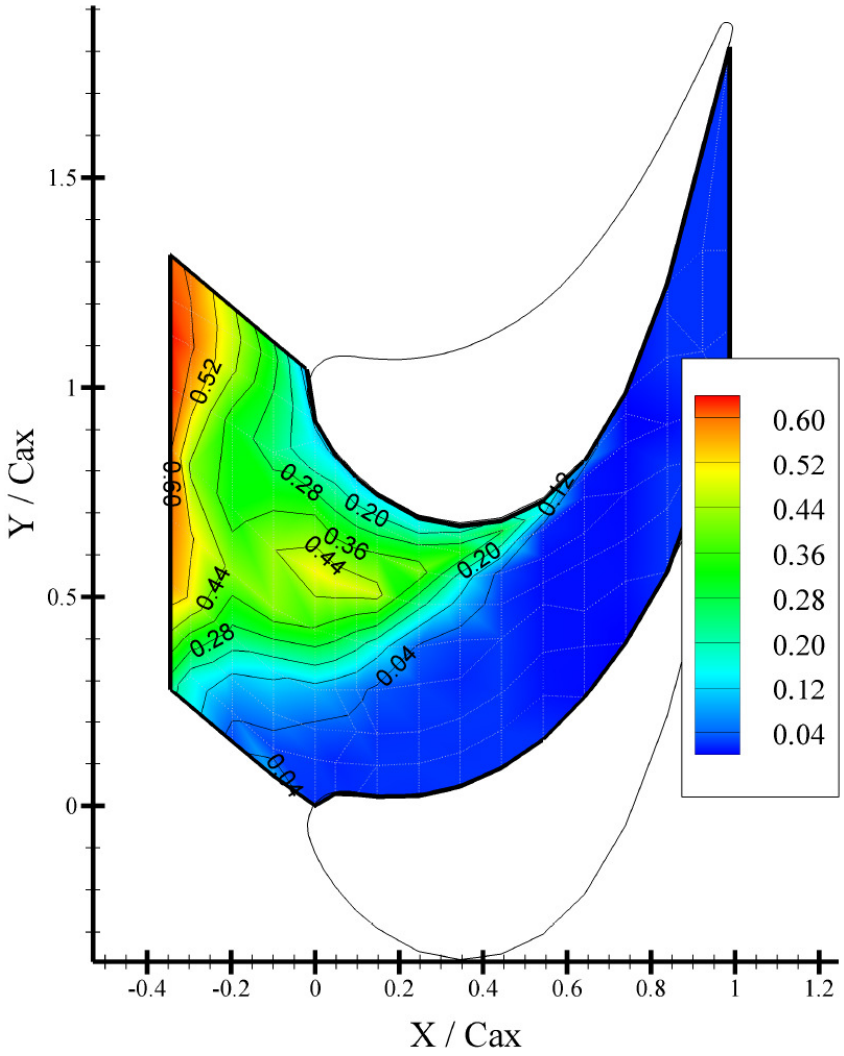

Figure 68. Endwall Adiabatic Film Cooling Effectiveness Contours for Dolphin Nose Endwall with 1.0% Leakage MFR

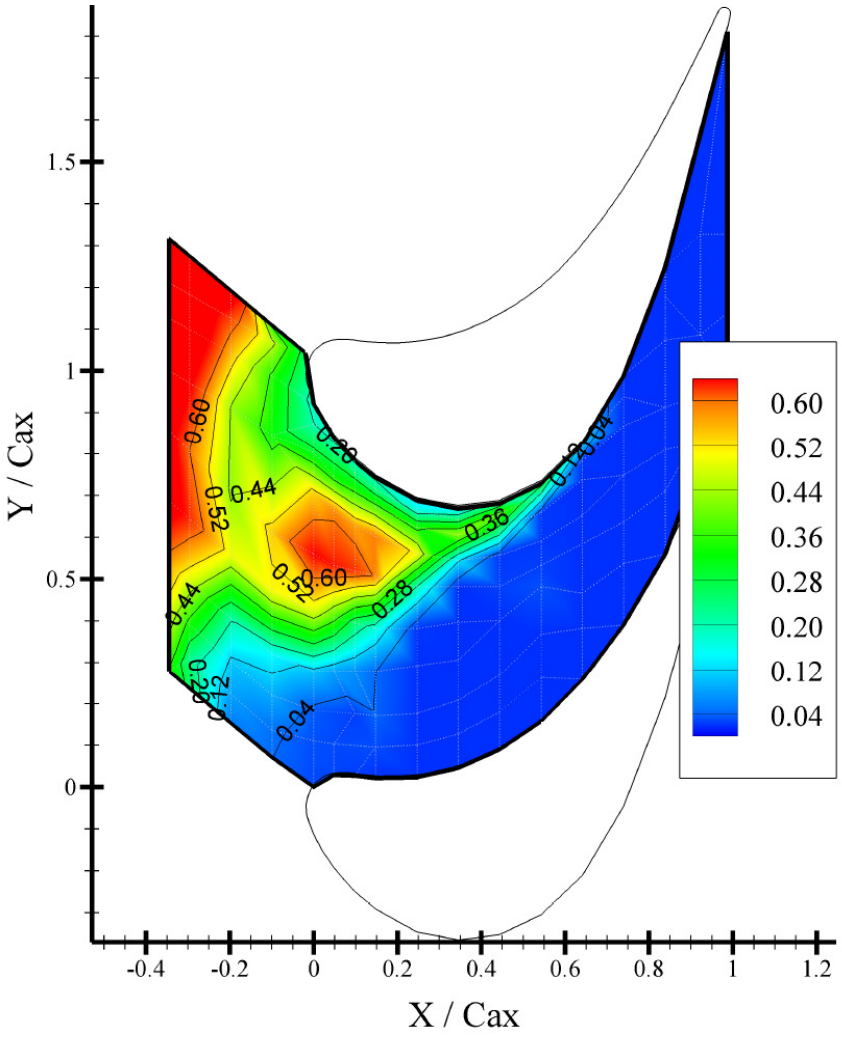

Figure 69. Endwall Adiabatic Film Cooling Effectiveness Contours for Dolphin Nose Endwall with 1.5% Leakage MFR

7.3.1.1 Effect of Heated Approach Flow at Three Leakage MFRs

Results for adiabatic film cooling effectiveness measurements on the dolphin nose endwall with a heated approach flow are given in Figure 70, Figure 71, and Figure 72 for leakage mass flow ratios of 0.5, 1.0, and 1.5%, respectively. Under these conditions, endwall adiabatic effectiveness values reveal the combined cooling effect of the leakage flow and approach flow in which there is a thermal boundary contained in a region of roughly 0-9% of the blade chord (0-10% of the approach flow channel height). In general, the heated approach flow "evens out" some of endwall temperature gradients

seen in the previous uniform-temperature approach flow results. Effectiveness values are spread out more uniformly with a bias towards the suction side. The overall effectiveness "patterns" seen in previous contour plots (i.e. Figures 67, 68, and 69) do not differ significantly with these. Additionally, changes in leakage flow rate appear to only cause variations in effectiveness magnitudes as the patterns remain similar (see Figures 70, 71, and 72). The most notable differences between the heated and uniform approach flow cases occur near blade stagnation points and the suction side-to-endwall corners. The approach flow is shown to penetrate these areas more effectively than did the leakage flow alone. This feature is significant as these areas are known to have high heat loads within an engine.

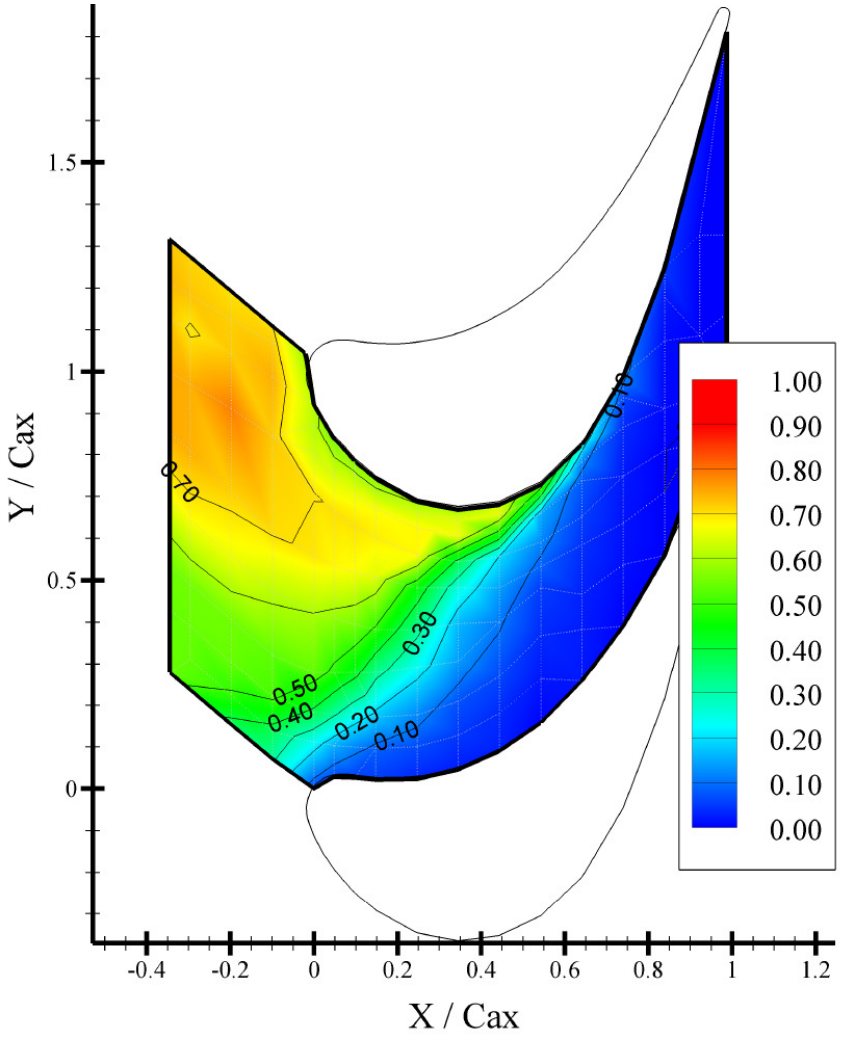

Figure 70. Endwall Adiabatic Film Cooling Effectiveness Contours for Dolphin Nose Endwall with 0.5% Leakage MFR and Heated Approach Flow

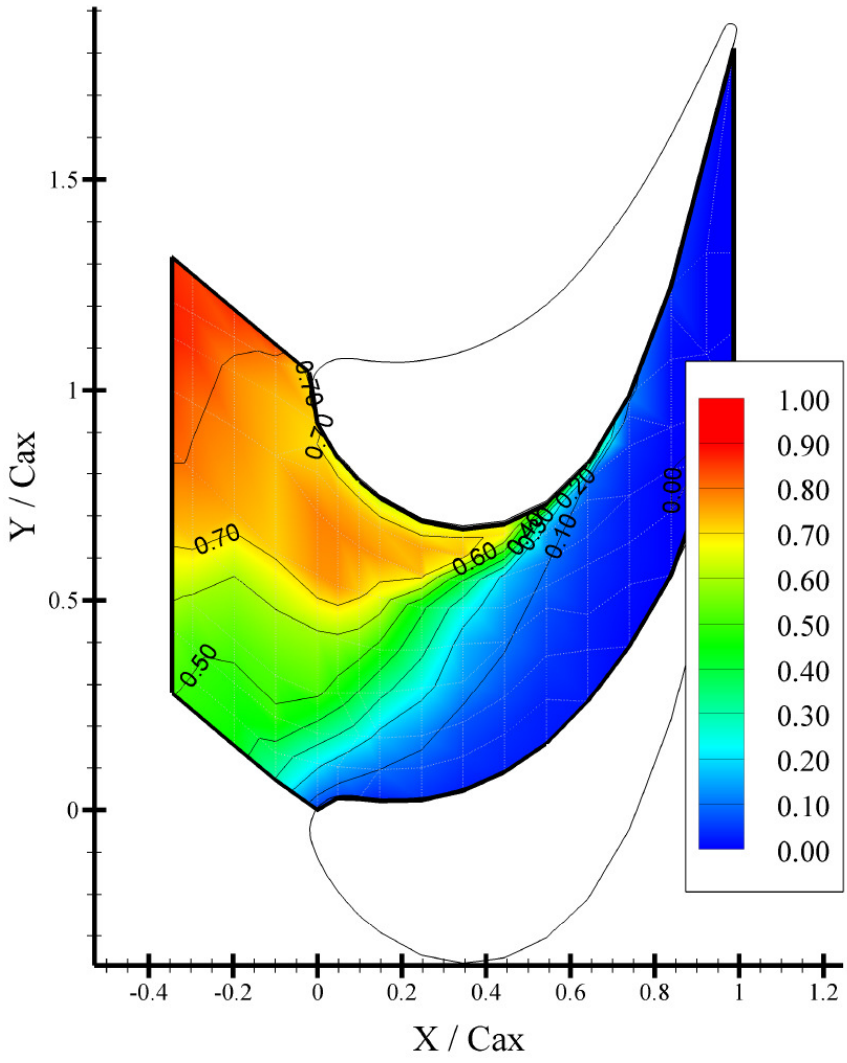

Figure 71. Endwall Adiabatic Film Cooling Effectiveness Contours for Dolphin Nose Endwall with 1.0% Leakage MFR and Heated Approach Flow

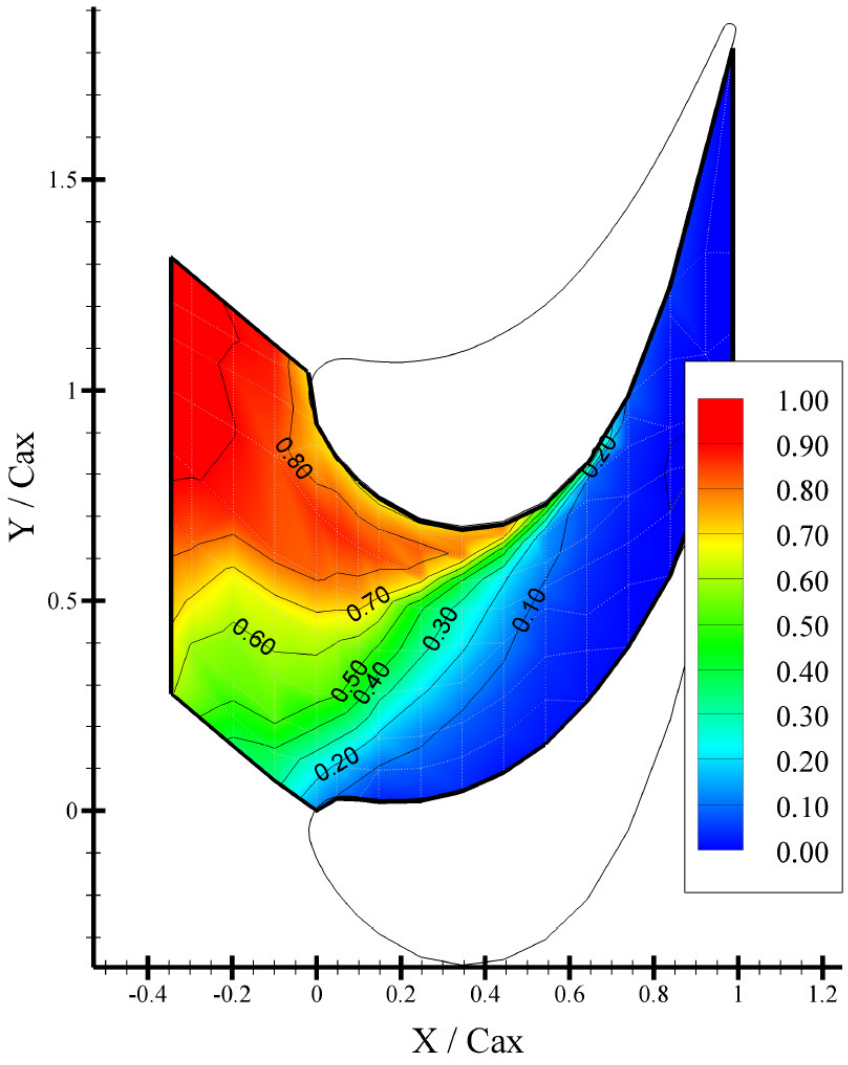

Figure 72. Endwall Adiabatic Film Cooling Effectiveness Contours for Dolphin Nose Endwall with 1.5% Leakage MFR and Heated Approach Flow

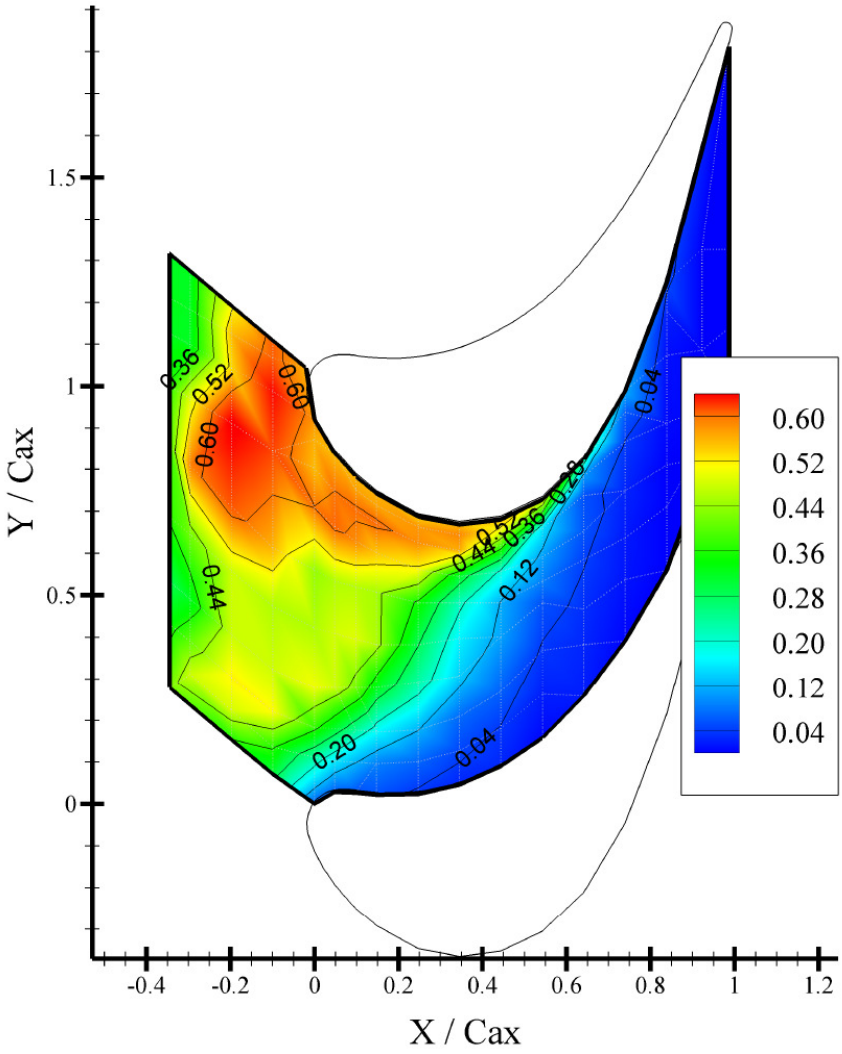

Figure 73. Endwall Adiabatic Effectiveness Contours for Dolphin Nose Endwall showing Augmentation Due to Heated Approach Flow at 0.5% Leakage MFR

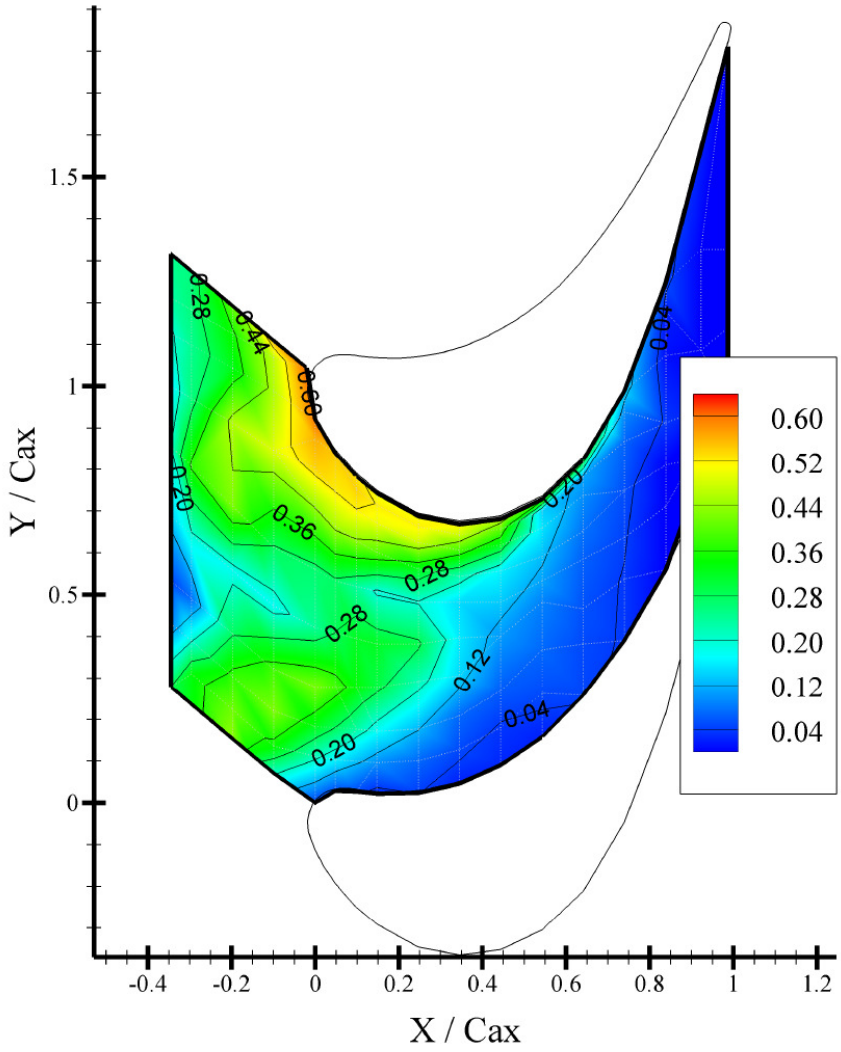

Figure 74. Endwall Adiabatic Effectiveness Contours for Dolphin Nose Endwall showing Augmentation Due to Heated Approach Flow at 1.0% Leakage MFR

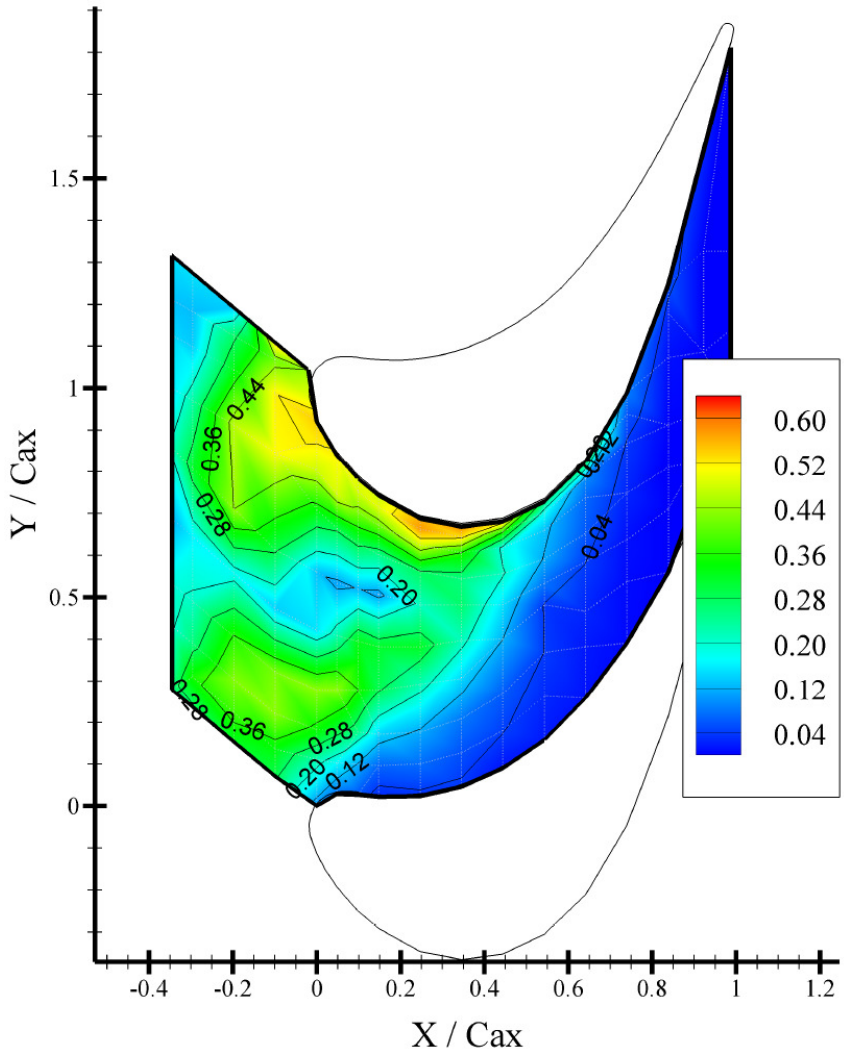

Figure 75. Endwall Adiabatic Effectiveness Contours for Dolphin Nose Endwall showing Augmentation Due to Heated Approach Flow at 1.5% Leakage MFR

The concept of superposition is implemented in an attempt to separate out the effects of the heated approach flow fluid on cooling effectiveness. This is done while assuming the fluid mechanics remains unchanged between the two approach flow cases excluding density effects (which should be minimal). This is only approximately true. For each of the three leakage flow rates, the uniform approach flow case is subtracted from its corresponding heated approach flow case and the results are plotted in Figure 73, Figure 74, and Figure 75. These data, which represent cooling effectiveness augmentation, show that the near-wall approach fluid has a strong interaction with the leakage fluid even near the disc cavity ejection (leakage) slot. More explicitly, the effectiveness patterns show

that the approaching near-wall fluid is able to penetrate into the "gutter" region of the endwall (upstream of the endwall contouring), thus affecting surface temperatures. For the case of a leakage MFR=0.5% in Figure 73, the heated approach flow dominates the endwall cooling patterns. This was previously expected as the heated approach flow fluid represents a significant increase in blowing ratio over that of the leakage flow. For leakage MFR's of 1.0 and 1.5%, a more complicated cooling augmentation pattern appears to reveal itself as shown in Figure 74 and Figure 75. At these leakage flow rates, the approach flow does not appear to have a strong influence in a narrow horizontal band located along $y/C_{ax} \approx 0.5$. This region of decreased influence seems to extend all the way from the disc cavity ejection slot ($x/C_{ax} = -0.345$) to where the pressure leg of the horseshoe vortex entrains all of the leakage flow ($x/C_{ax} \approx 0.45$). These patterns may reveal the existence of a leakage flow "Venturi" effect where the approach flow constricts the leakage flow coming from the disc cavity ejection slot. This "constriction" accelerates the leakage flow through this horizontal region of the plot where it contributes to high effectiveness values over the endwall surface. The acceleration of the leakage flow also tends to decrease mixing between the two fluids in this region. Another separate observation is that the heated approach flow appears to not extend cooling effectiveness further downstream within the passage than observed with the uniform temperature approach flow cases. This suggests that the pressure leg of the horseshoe vortex also entrains or lifts the heated approach fluid away from the endwall. This speaks to the size and strength (low pressure) of this vortex as it sweeps across the endwall.

7.3.2 Shark Nose Endwall Geometry at Three Leakage MFRs

Shark nose endwall adiabatic effectiveness values with a uniform temperature approach flow are reported in Figure 76, Figure 77, and Figure 78 for leakage mass flow ratios of 0.5, 1.0, and 1.5% respectively. In general, there is an improvement seen in effectiveness magnitude as the leakage flow increases. The affected surface area does not significantly change with leakage flow rate. Several other observations can be made without regard to leakage flow rate. Firstly, endwall cooling effectiveness is concentrated to the suction side of the passage. Regions very close to the leakage slot provided fairly uniform

coverage; however, the effectiveness patterns are quickly skewed by, most likey, the passage pressure gradient. A second observation is that the leakage flow does not provide much coverage near the upper blade's stagnation point or suction side-to-endwall corner. Performance does improve with an increased leakage MFR; however, these regions are still covered less effectively than seen in the mid passage areas. It is worth noting that remnants of the leakage flow on the endwall entirely disappear at a downstream position of $x/C_{ax} = 0.6$. This corresponds well with the dolphin nose endwall results. Also, the shark nose endwall results do not appear to exhibit any localized peaks in effectiveness magnitude, contrary to the results with the dolphin nose (e.g. Figure 68 [x/Cax=0, y/Cax=0.55]). This suggests that the occurrences of these localized peaks are related to wall contouring.

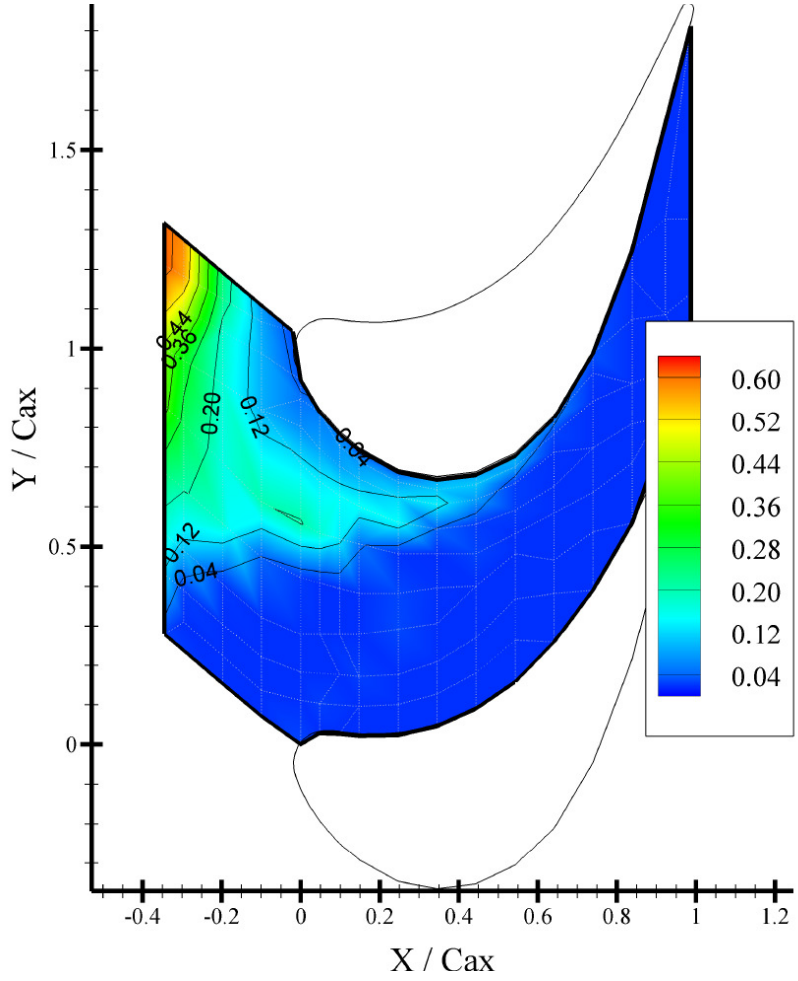

Figure 76. Endwall Adiabatic Film Cooling Effectiveness Contours for Shark Nose Endwall with 0.5% Leakage MFR

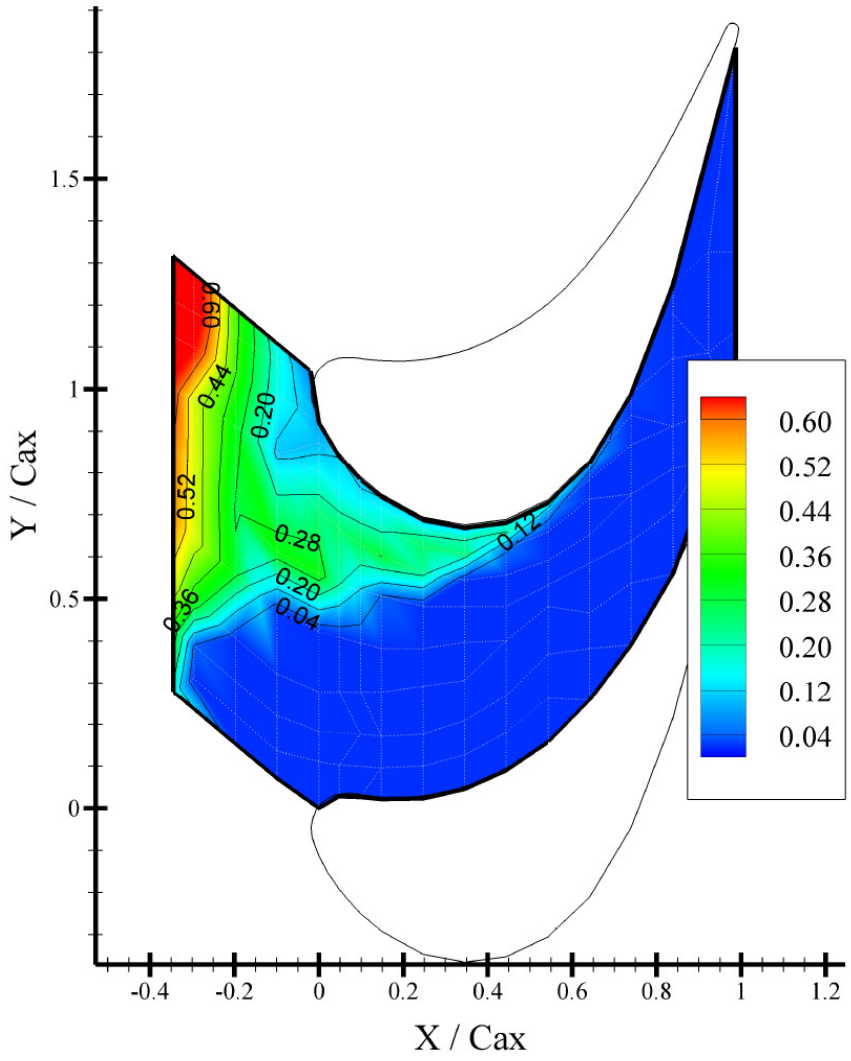

Figure 77. Endwall Adiabatic Film Cooling Effectiveness Contours for Shark Nose Endwall with 1.0% Leakage MFR

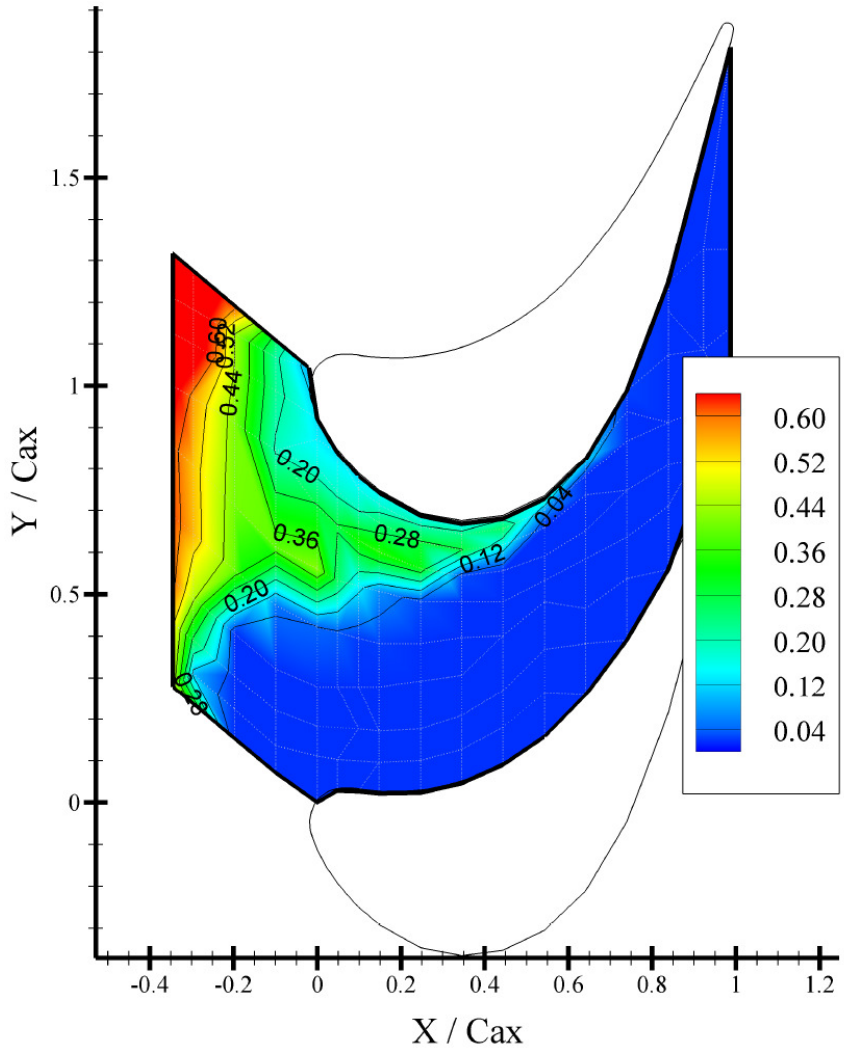

Figure 78. Endwall Adiabatic Film Cooling Effectiveness Contours for Shark Nose Endwall with 1.5% Leakage MFR

7.3.2.1 Effect of Heated Approach Flow at Three Leakage MFRs

Results for adiabatic film cooling effectiveness measurements on the shark nose endwall with a heated approach flow are given in Figure 79, Figure 80, and Figure 81 for leakage mass flow ratios of 0.5, 1.0, and 1.5%, respectively. As described for the corresponding dolphin nose endwall measurements, these data reveal the combined cooling effects of leakage flow and approach flow fluid contained in the boundary layer region which is roughly $y/C = 0.09$ in thickness (10% of the approach flow channel height). In general, significant improvements in both effectiveness magnitude and coverage area are seen.

This is as a result of the heated approach flow. Like the dolphin nose endwall results, the shark nose endwall is well cooled upstream of the leading edge plane. There is again a bias in η magnitudes with larger values towards the upper blade. Moving downstream, the cooling coverage skews toward the passage suction side. A demarcation line extends from the bottom blade's leading edge to approximately $x/C_{ax} = 0.75$ on the top blade's suction side. This quite possibly traces the passage vortex path as it sweeps across the endwall surface. No evidence of endwall cooling coverage is seen to extend downstream of this line.

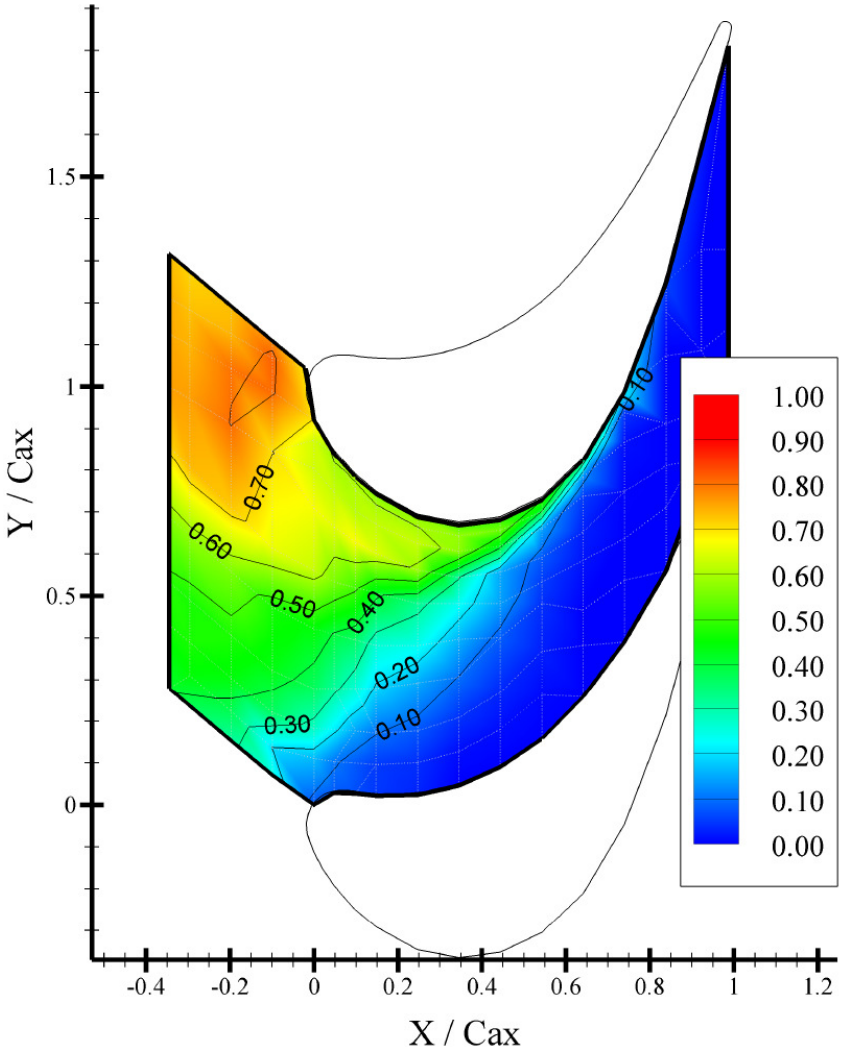

Figure 79. Endwall Adiabatic Film Cooling Effectiveness Contours for Shark Nose Endwall with 0.5% Leakage MFR and Heated Approach Flow

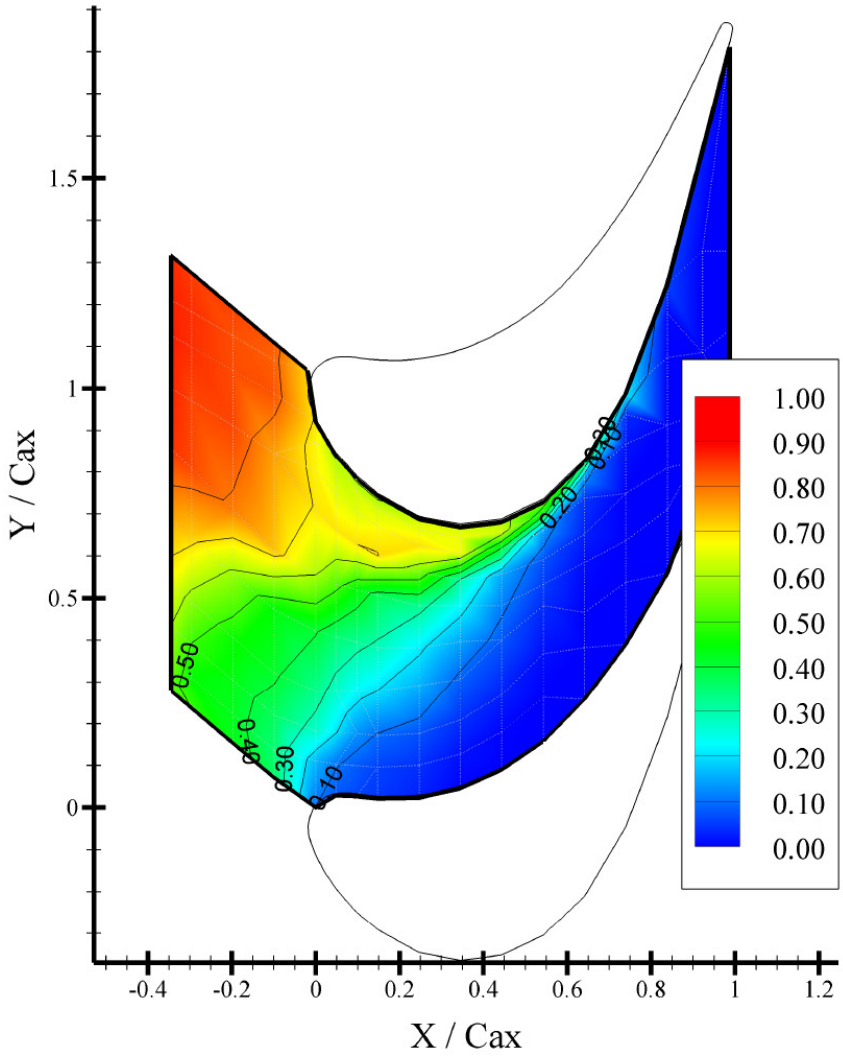

Figure 80. Endwall Adiabatic Film Cooling Effec tiveness Contours for Shark Nose Endwall with 1.0% Leakage MFR and Heated Approach Flow

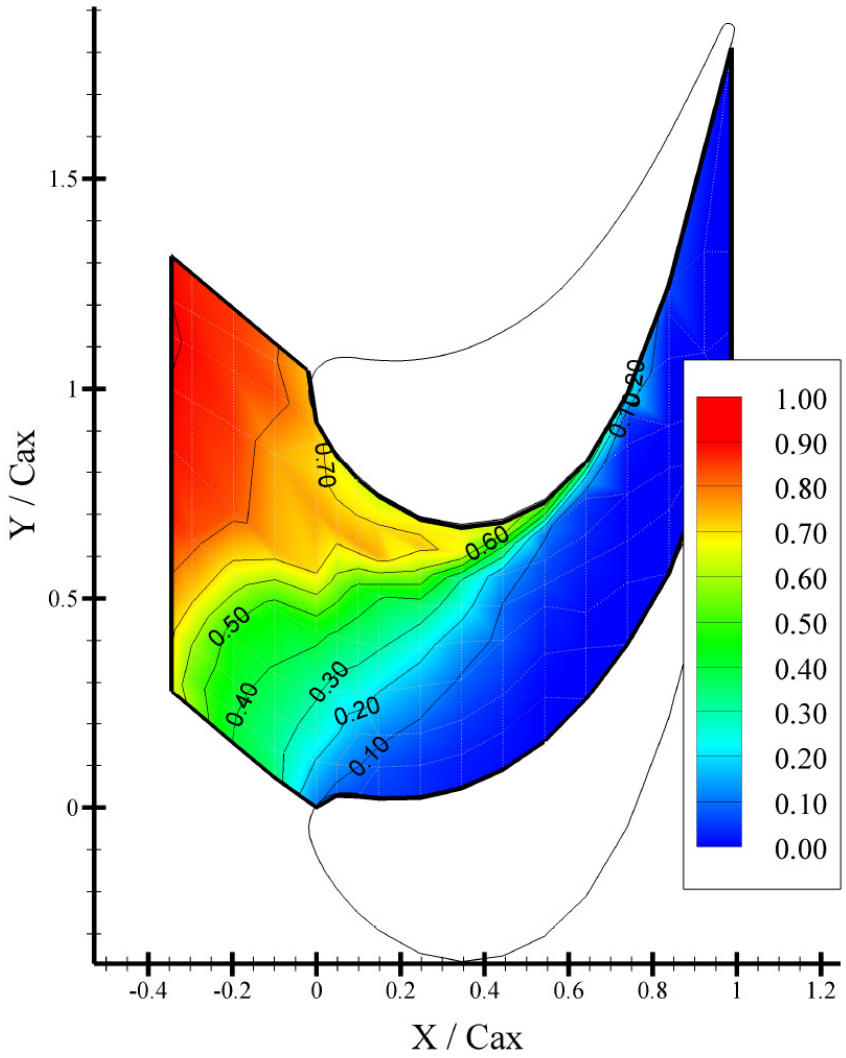

Figure 81. Endwall Adiabatic Film Cooling Effectiveness Contours for Shark Nose Endwall with 1.5% Leakage MFR and Heated Approach Flow

To attempt to isolate the effects of the heated approach flow on endwall cooling effectiveness, the heated approach flow and uniform temperature approach flow cases are differenced. This is identical to the operation which was performed with the dolphin nose endwall adiabatic effectiveness augmentation cases. Results for the shark nose endwall cases which are plotted in Figure 82 through Figure 84 reveal that the heated approach flow has a significant effect on endwall cooling upstream of the leading edge plane. It also produces major improvements in areas where the leakage flow, alone, was not effective. These include the regions around blade stagnation points and the upper blade's suction side-to-endwall corner. The consequence of increasing leakage flow rate

appears to be a decrease in the augmentation attributed to the heated approach flow. In other words, increases in leakage flow reduce the dominance of near-wall approach fluid. This agrees with findings from the dolphin nose data set. The shark nose geometry, however, seems to be slightly less affected by leakage flow rate. This may also be a reason why the shark nose augmentation results appear more uniform than equivalent dolphin nose cases (e.g. Figure 83 compared with Figure 74 around mid-pitch area).

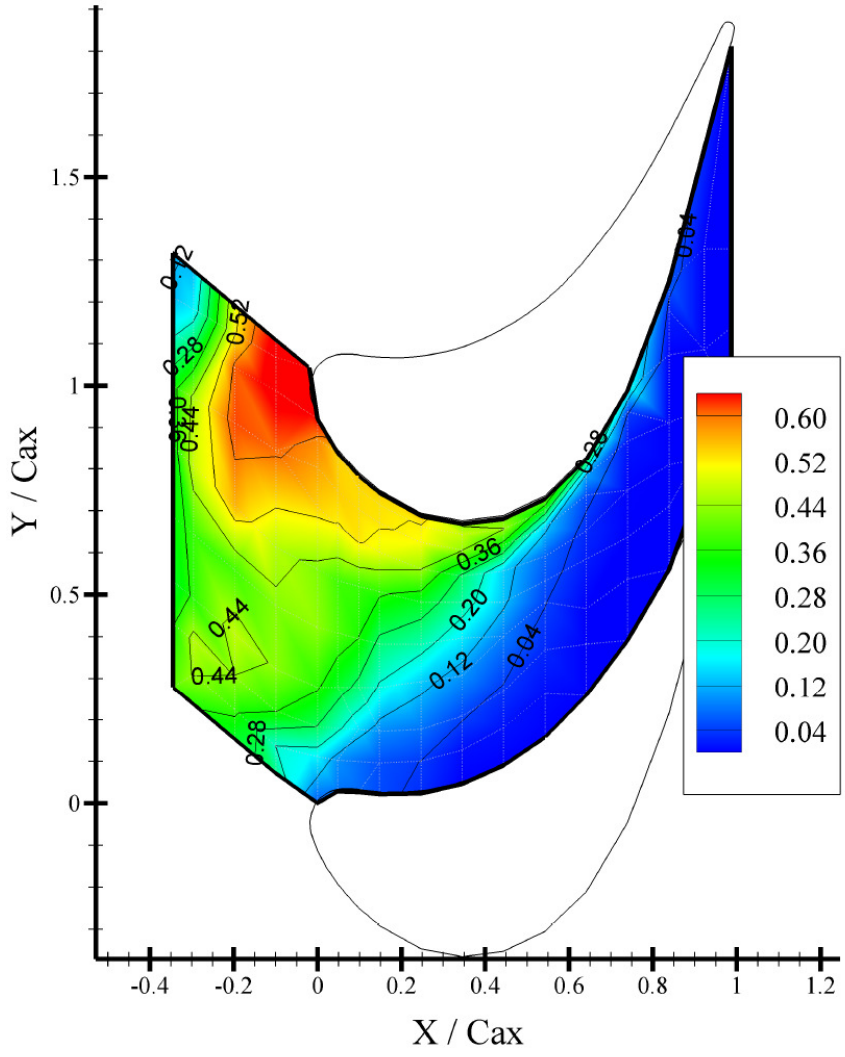

Figure 82. Endwall Adiabatic Film Cooling Effectiveness Contours for Shark Nose Endwall showing Augmentation Due to Heated Approach Flow at 0.5% Leakage MFR

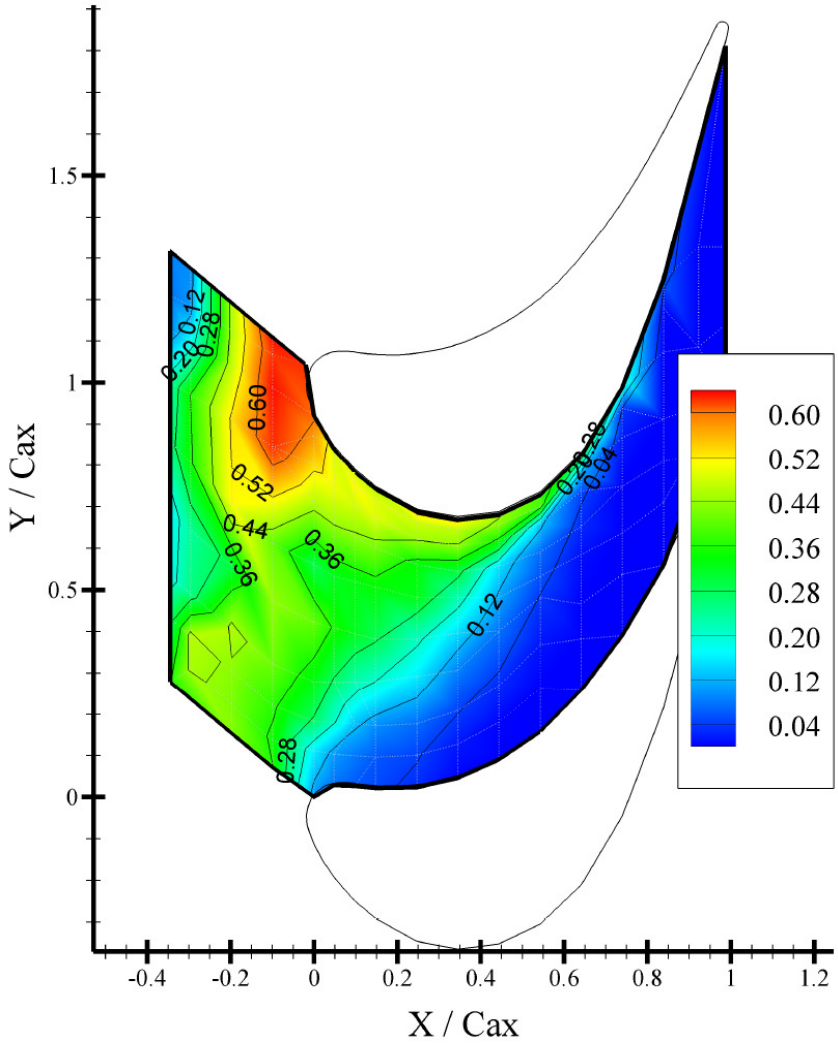

Figure 83. Endwall Adiabatic Film Cooling Effectiveness Contours for Shark Nose Endwall showing Augmentation Due to Heated Approach Flow at 1.0% Leakage MFR

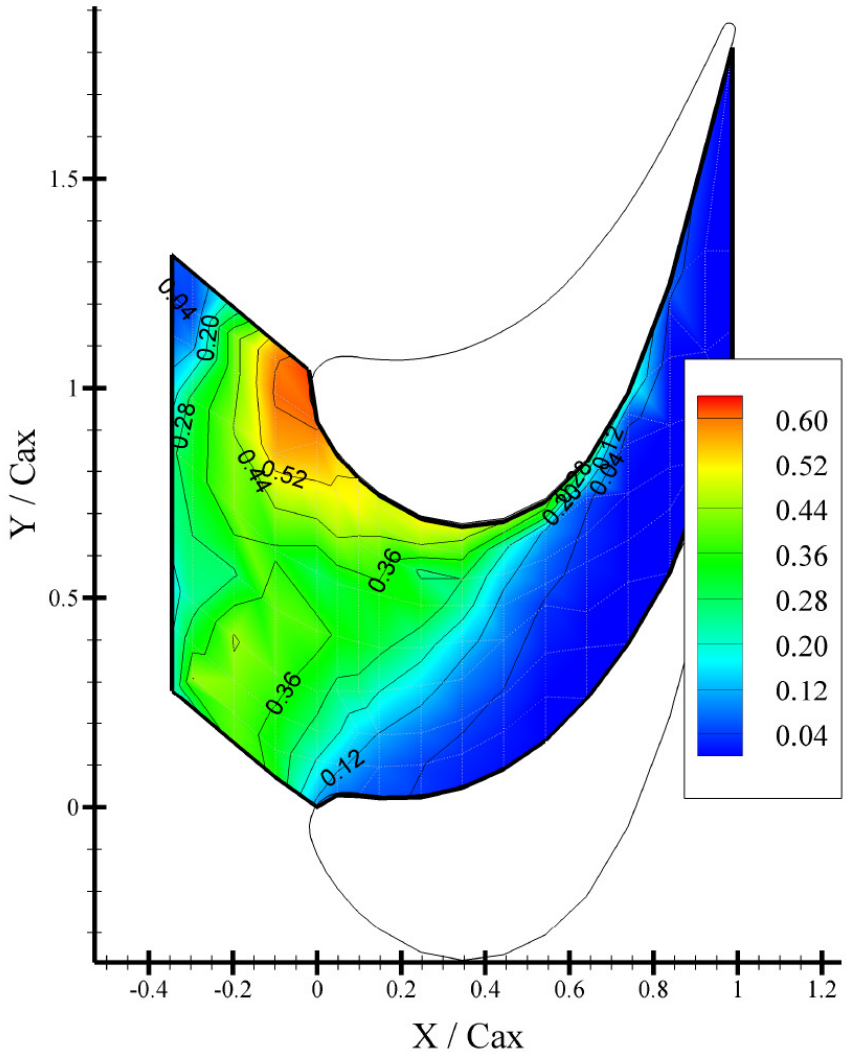

Figure 84. Endwall Adiabatic Film Cooling Effectiveness Contours for Shark Nose Endwall showing Augmentation Due to Heated Approach Flow at 1.5% Leakage MFR

7.3.3 Comparison of Dolphin Nose and Shark Nose Endwall Results

To better visualize the effects of wall contouring on endwall adiabatic effectiveness, dolphin nose results ($\eta_{dolphin}$) from Section 7.2.1 and shark nose results (η_{shark}) from Section 7.2.2 (both having a uniform approach flow temperature) are differenced. The resulting comparison data are referenced as $\Delta\eta_{comp}$ and formally defined in (Eq. 7.2). As a result of this formulation, positive $\Delta\eta_{comp}$ values indicate better performance by the dolphin nose contour and negative values indicate better performance by the shark nose

contour. Comparison results are given in Figure 85, Figure 86, and Figure 87 for leakage mass flow ratios of 0.5, 1.0, and 1.5%, respectively.

$$\Delta\eta_{comp}(x,y) = \eta_{dolphin}(x,y) - \eta_{shark}(x,y) \qquad \text{(Eq. 7.2)}$$

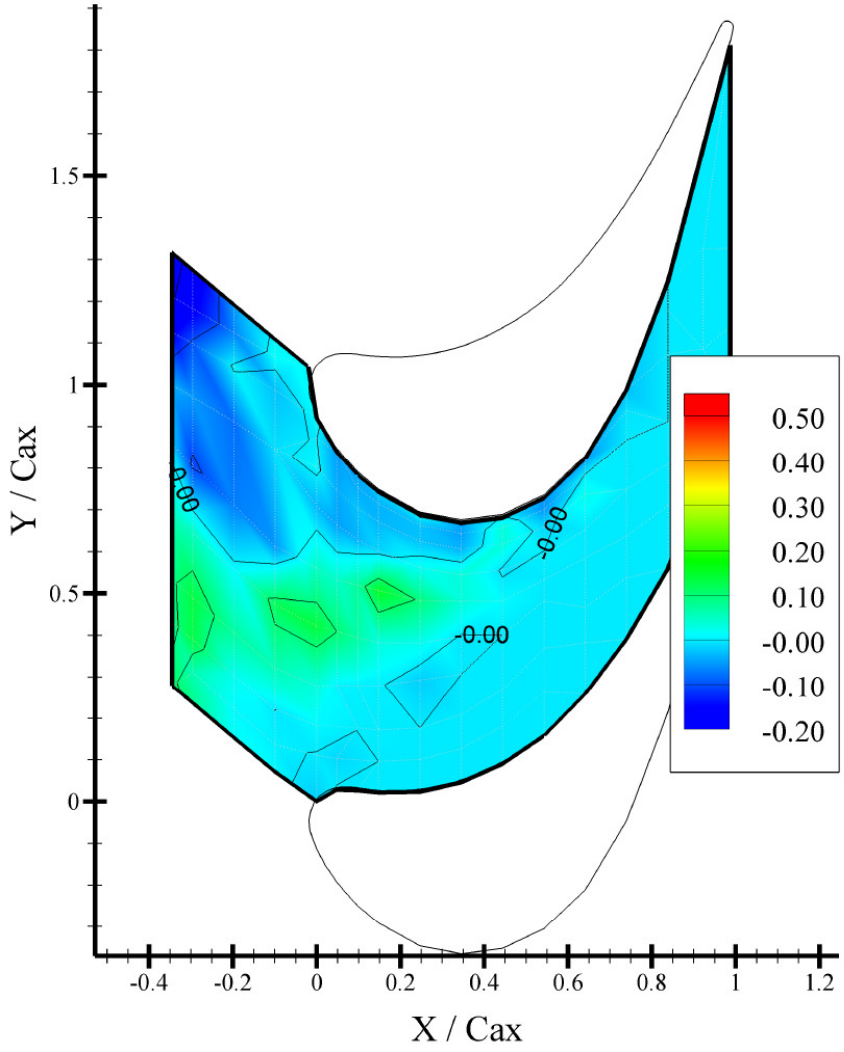

Figure 85. Endwall Adiabatic Film Cooling Effectiveness Contours for Differenced (Dolphin minus Shark Nose) Endwall Results at 0.5% Leakage MFR

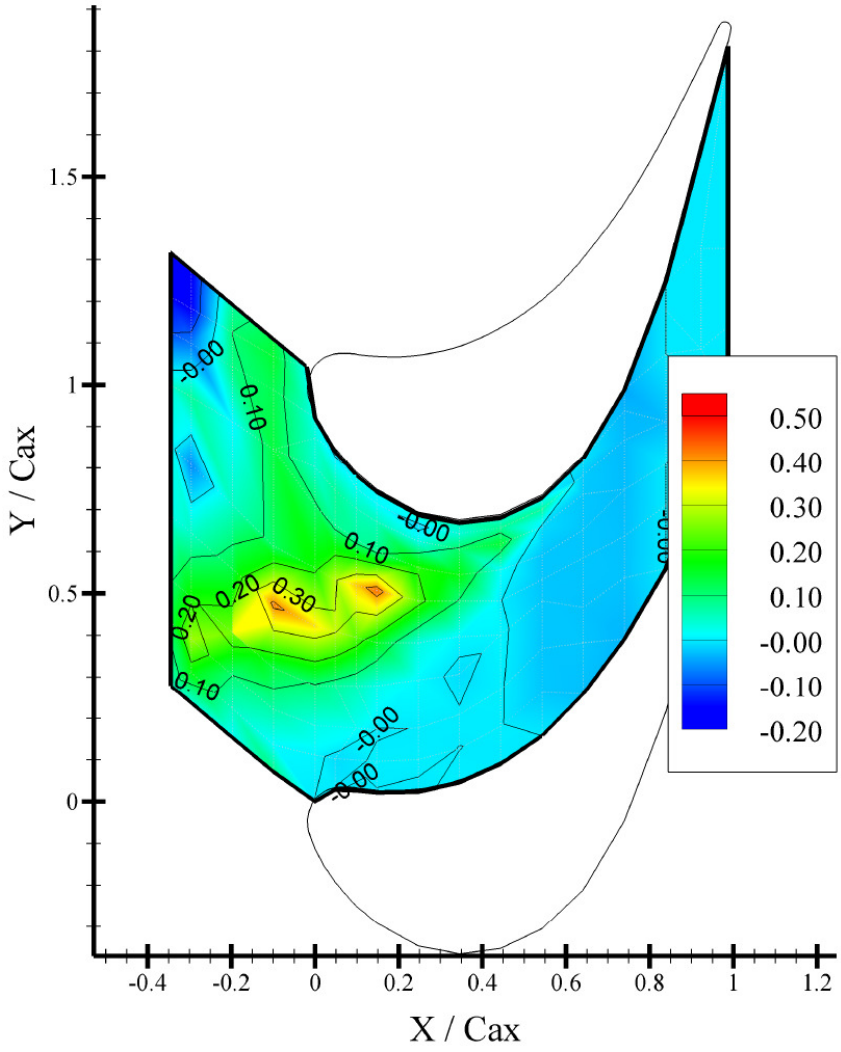

Figure 86. Endwall Adiabatic Film Cooling Effectiveness Contours for Differenced (Dolphin minus Shark Nose) Endwall Results at 1.0% Leakage MFR

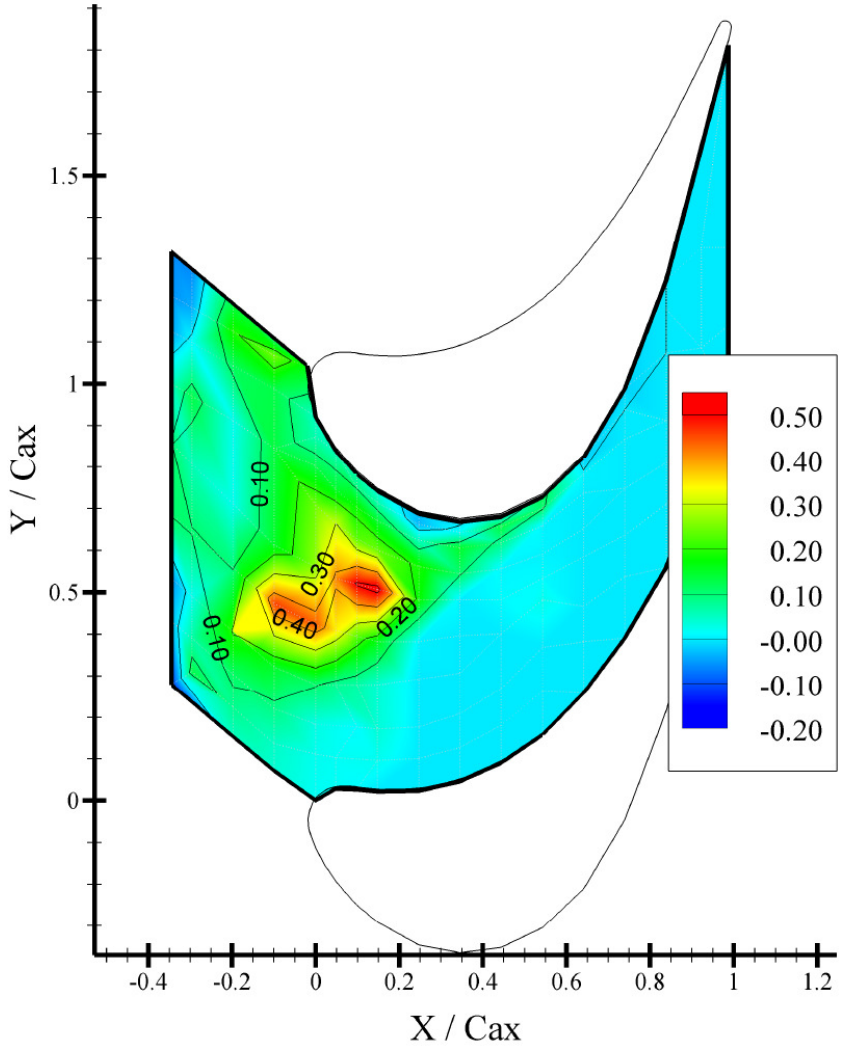

Figure 87. Endwall Adiabatic Film Cooling Effectiveness Contours for Differenced (Dolphin minus Shark Nose) Endwall Results at 1.5% Leakage MFR

Comparison results for the case of 0.5% leakage MFR indicate little variation due to wall contouring. In general, $\Delta\eta_{comp}$ values float around zero ±0.05. Three peaks of around $\Delta\eta_{comp} = 0.1$ are seen along a horizontal line of $y/C_{ax} = 0.5$. Minimum values of $\Delta\eta_{comp} = -0.1$ are seen in a small area near the top of the leakage slot. As the leakage flow is increased to 1.0% MFR, the same patterns appear but with larger magnitudes (Figure 86). The region of positive values significantly increases revealing that the dolphin nose endwall performs better with more leakage flow. This is possibly due to the stronger acceleration profile with the dolphin nose geometry. At a leakage MFR of 1.5%

(Figure 87) there appears to be no instances where the shark nose endwall performs better than the dolphin nose endwall.

7.3.3.1 Comparison of Endwall Results with a Heated Approach Flow

The same process for comparing differences in effectiveness results due to endwall contouring is repeated for the heated approach flow data sets and reported in Figure 88, Figure 89, and Figure 90. This information reveals differences between the two endwall geometries with combined leakage and approach flow cooling. In general, the results show very similar trends as those described in the previous section with a uniform temperature approach flow. The main difference is that $\Delta\eta_{comp}$ values are on average lower when a heated approach flow is included. This shows that the approach flow tends to even out both leakage flow and endwall contouring effects. In all three cases of leakage flow rate tested, the effectiveness results average to a positive $\Delta\eta_{comp}$ value. This indicates that the dolphin nose endwall still does perform better than the shark nose endwall, as alluded to in the previous section.

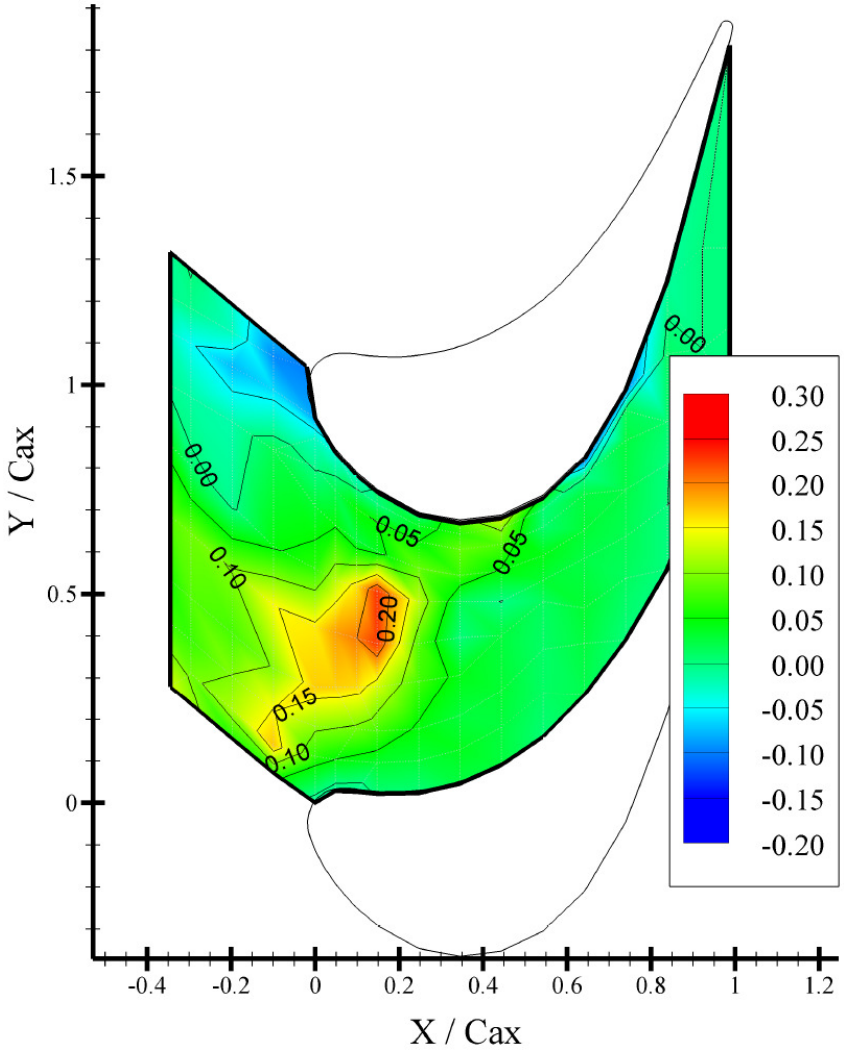

Figure 88. Endwall Adiabatic Film Cooling Effectiveness Contours for Differenced (Dolphin minus Shark Nose) Endwall Results with a Heated Approach Flow at 0.5% Leakage MFR

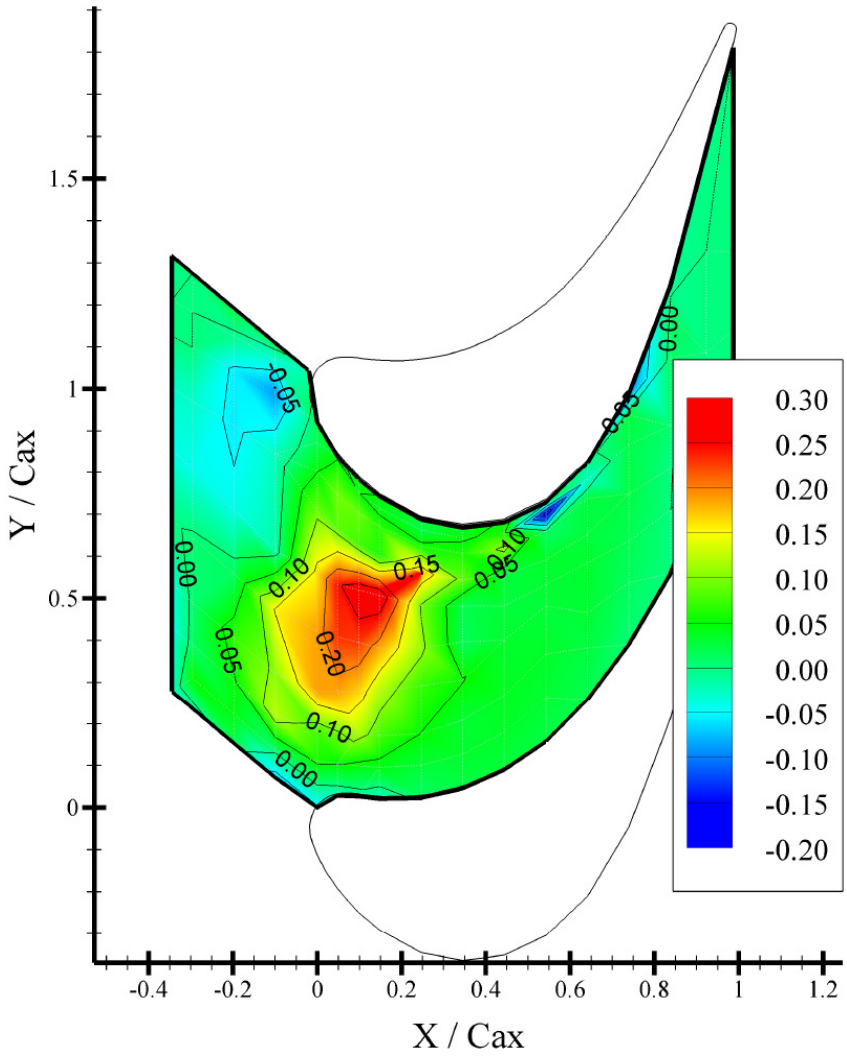

Figure 89. Endwall Adiabatic Film Cooling Effectiveness Contours for Differenced (Dolphin minus Shark Nose) Endwall Results with a Heated Approach Flow at 1.0% Leakage MFR

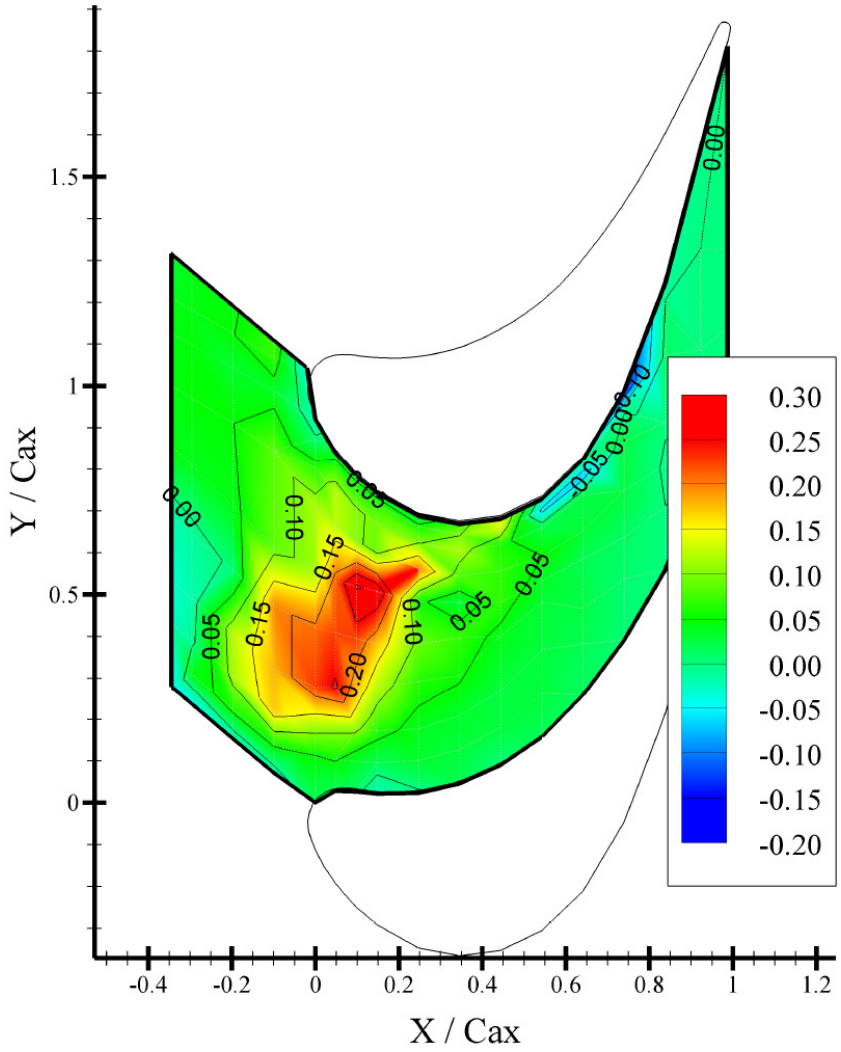

Figure 90. Endwall Adiabatic Film Cooling Effectiveness Contours for Differenced (Dolphin minus Shark Nose) Endwall Results with a Heated Approach Flow at 1.5% Leakage MFR

7.3.4 Comparison of Pitch-Averaged Endwall Adiabatic Film Cooling Effectiveness Values

Results in this section originate from the contour plot data previously reported in sections 7.3.1 and 7.3.2. They are averaged in the pitchwise direction (y/C_{ax}) and are plotted as a function of axial distance (x/C_{ax}). This information provides a simplistic two-dimensional view of the results, which is useful in assessing general trends.

Firstly, the base cases are analyzed for both endwall contours for cases that incorporate a uniform approach flow temperature and three leakage mass flow ratios. These six base cases are plotted as a function of axial distance in Figure 91.

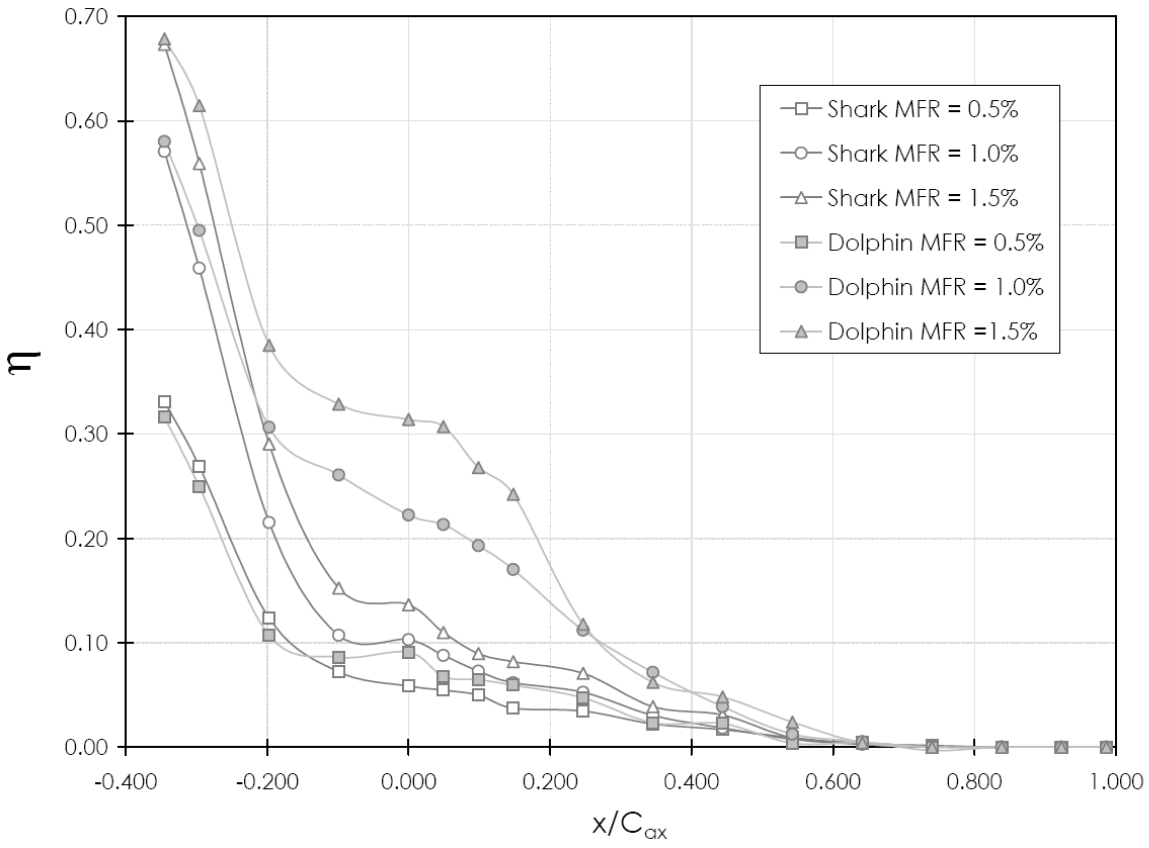

Figure 91. Pitch-Averaged Film Cooling Effectiveness Values Comparing Shark Nose and Dolphin Nose Endwalls with Unheated Approach Flow

Discussion of the plotted results in Figure 91 begins with the three shark nose endwall cases. For all three cases of leakage MFR with the shark nose endwall, peak adiabatic effectiveness (η) values are seen at the leakage slot location ($x/C_{ax} = -0.345$). These peak η values are 0.33, 0.57, and 0.67 for leakage MFR's of 0.5, 1.0, and 1.5%, respectively. The fact that η values at the leakage slot are not equal to unity (wall temperatures not equal to those at rim seal) indicates that an undesired mixing process is taking place within the leakage plenum to decrease the adiabatic effectiveness. In this experiment, only mainstream fluid could cause this change. This finding is strong

evidence that mainstream flow ingression is taking place within the test section. Furthermore, since the endwall effectiveness values are not equal to one another for the three cases, it can be said that the degree of flow ingression is dependent upon the leakage flow rate; higher leakage flow rates allowing for less ingression. Moving downstream of the leakage slot, one sees that a steep decrease in η values occurs until roughly $x/C_{ax} = -0.1$ where they are measured to be 0.07, 0.11, and 0.15 for leakage MFR's of 0.5, 1.0, and 1.5%, respectively. These data reveal that approximately 80% of the leakage flow's endwall cooling potential has been lost between the leakage slot ($x/C_{ax} = -0.345$) and this location ($x/C_{ax} = -0.1$) regardless of leakage flow rate. Moving further downstream reveals that there is little-to-no change in adiabatic film cooling effectiveness between $x/C_{ax} = -0.1$ and the leading edge plane ($x/C_{ax} = 0$) for all three leakage flow rates. One proposed explanation for this behavior is that the endwall contour is causing fluid acceleration in this area, thus temporarily decreasing leakage-to-mainstream mixing effects. From the leading edge plane to downstream into the passage, the pitch-averaged adiabatic effectiveness data gradually decrease in a fairly linear fashion for all three leakage flow rates. At a position of $x/C_{ax} = 0.75$, remnants of the leakage fluid coolant coverage have completely disappeared.

Results of the dolphin nose endwall pitch-averaged η measurements exhibit many similar features as those described for the shark nose geometry. Dolphin nose η values nearest the leakage slot ($x/C_{ax} = -0.345$) are within 0.02 of the shark nose values for all three leakage flow rates. This finding suggests that the differences in mainstream flow ingression between the two endwall contours tested are small. Moving downstream along the endwall, one sees that the dolphin nose results begin to deviate from those of the shark nose. Also, differences between the three leakage flow rate cases begin to reveal themselves. A steady drop in η is seen from the leakage slot ($x/C_{ax} = -0.345$) to approximately $x/C_{ax} = -0.2$; however, these are not as drastic those seen with the shark nose geometry. The exception to the previous statement is the case of 0.5% leakage MFR which agrees quite well with the shark nose data at this location. Between $x/C_{ax} = -0.2$ and the leading edge plane ($x/C_{ax} = 0$), endwall effectiveness values

remain fairly constant, decreasing by a maximum of 8%. This behavior is similar to that seen in the shark nose endwall; however, it is more pronounced with the dolphin nose geometry and extends over a longer streamwise distance. This region is undoubtedly dominated by the endwall contour profile; thus, the largest differences in data trends between the two geometries are seen here. It is also noted that leakage flow rate has a strong effect on cooling coverage along the endwall upstream of the leading edge plane. This is much more pronounced with the dolphin nose endwall contour than with the shark nose geometry. Moving further downstream of the leading edge plane, one sees that η values again begin to gradually decrease. At a location of $x/C_{ax} = 0.247$ there becomes no discernable difference between the 1.0% and 1.5% leakage MFR cases. This behavior continues until approximately $x/C_{ax} = 0.75$ where remnants of the leakage flow disappear altogether. One important observation to be made is that the dolphin and shark nose cases of 0.5% leakage flow show relatively little difference between them. It is possible that this flow rate is simply too small to create leakage slot velocities which have an impact on the flow in the endwall region.

The second set of pitch-averaged adiabatic effectiveness data to be discussed is plotted in Figure 92. These measurements represent three leakage MFR cases for each of the shark and dolphin nose geometries with a heated near-wall approach flow so that $T_\ell = T_w$, or the η value on the endwall just upstream of the beginning of the leakage plenum matches the η value of the leakage flow. Again, this near-wall heating simulates the effects of combustor dilution air on the approach flow thermal profile. Under these conditions, it may be said that measuring endwall surface temperatures can reveal the combined cooling effects of the leakage flow and the approach flow. It is also noted that no changes to the approach flow fluid mechanics should exist for the injection flow that creates this approach flow boundary layer is present whether it is heated or not.

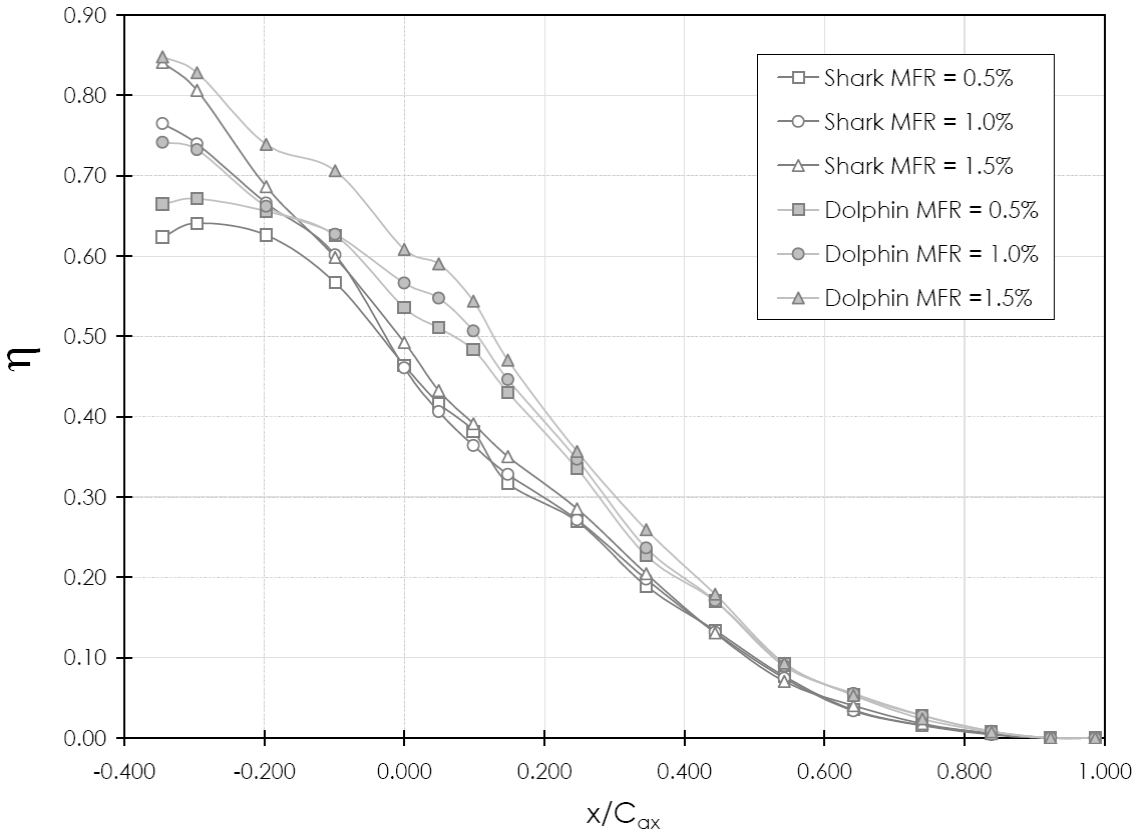

Figure 92. Pitch-Averaged Film Cooling Effectiveness Values Comparing Shark Nose and Dolphin Nose Endwalls with Heated Approach Flow

Similar to the uniform temperature approach flow data set, leakage slot ($x/C_{ax} = -0.345$) η values are fairly equal for the shark and dolphin nose geometries. Also, there is a strong dependence on leakage flow rate at this location. By comparing results within Figure 91 and Figure 92, one sees that the heated approach flow has a considerable influence on endwall temperatures, regardless of endwall contour. This influence is especially apparent in the 0.5% leakage flow data for which effectiveness values are increased by almost 100% when the heated approach flow is added. Moving downstream along the endwall, one sees an apparent divergence between the shark and dolphin endwall temperatures beginning around $x/C_{ax} = -0.2$. For all three leakage MFR's, the dolphin nose data take on a less negative slope resulting in higher η values. This feature was seen also in the uniform approach flow data set, hypothesized to be a result of the wall contouring. This increased performance persists throughout the

remainder of the passage, although decreasing with downstream distance. It is noted, however, that the dolphin nose endwall performance appears to have no dependence on leakage flow rate downstream of $x/C_{ax} \approx 0.25$. The feature of having little to no leakage flow dependence appears to persist much further upstream in the case with the shark nose geometry ($x/C_{ax} \approx 0$). This is largely a testament to the overpowering thermal effect of having the heated approach flow. The existence of measurable η values persists slightly further into the passage with the heated approach flow data than with the uniform temperature approach flow counterpart. This is likely due to the increased energy added to the passage due to heating of the approach flow.

Chapter 8

Supplementary Computational Fluid Dynamics Study

8.1 2D Study of Leakage Flow Rate and Endwall Curvature Effects

A two-dimensional CFD simulation is carried out with the software *FLUENT* to investigate the effects of endwall curvature and varying leakage flow ratios on endwall adiabatic effectiveness. The geometry modeled includes a two-dimensional cross section of the leakage plenum, endwall surface, and mainstream flow. Effects of blading, rotation, and three-dimensionality are not considered in these models. Two meshes are created for the geometry incorporating different endwall curvatures (shark nose and dolphin nose) from the cascade test section. Three leakage MFRs (0.5%, 1.0%, and 1.5%) are simulated for each mesh, totaling 6 separate cases. Steady state solutions for the energy and Reynolds Averaged Navier-Stokes (RANS) equations are found, and grid independence is verified through mesh refinement. Results suggest that the dolphin nose endwall curvature produces better thermal coverage over the endwall than the shark nose curvature at equal leakage flow rates. This is likely due to decreased leakage-to-mainstream flow mixing with the dolphin nose shape as well as better displacement of the mainstream flow away from the endwall surface. Results are also given for velocity distributions, temperature contours, and streamlines near the leakage plenum-to-mainstream interface.

8.1.1 Methodology

An example of the computational domain is given in Figure 93 showing the leakage plenum geometry (bottom) as well as the open wind tunnel volume (top). The flow is from left-to-right. The boundary conditions used in each model include velocity inlets (for the leakage slot flow and main tunnel flow), all walls are adiabatic, and one pressure outlet condition is imposed at the right edge of the domain. Turbulence is calculated using the Shear Stress Transport (SST) formulation of the k-ω model.

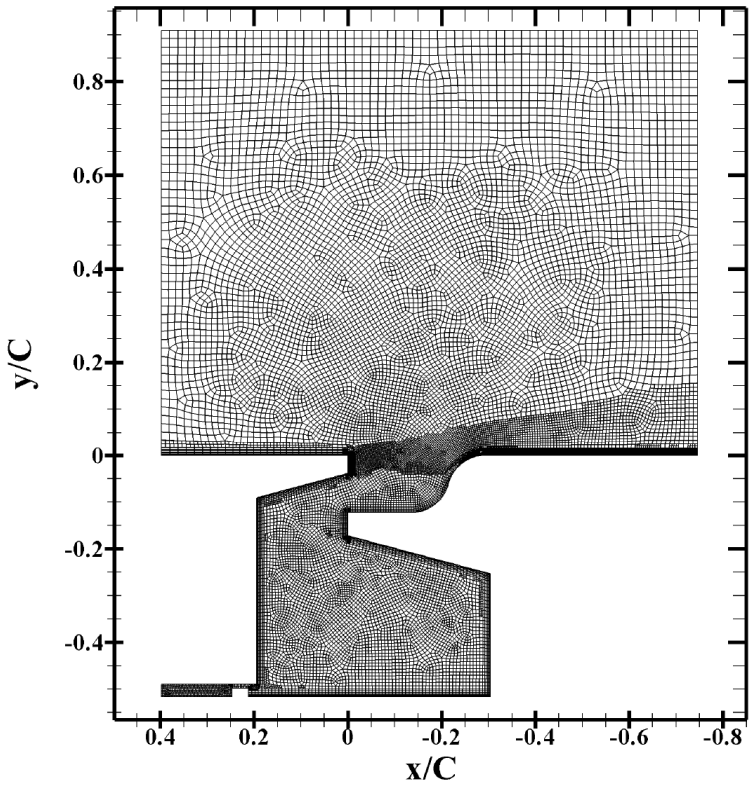

Figure 93. Example of CFD domain showing Leakage Plenum Geometry

The velocity inlet for the main wind tunnel flow is derived from hotwire velocity measurements within the tunnel. Test section inlet velocity data from Section 6.2.1 are pitchwise averaged and plotted along the spanwise distance. A very simple curve fit is then made to approximate the velocity distribution along the span. These curves are shown in Figure 94. The curve fit was then used in a Fluent "User Defined Function" (UDF) as the inlet velocity profile to the domain. A uniform turbulence intensity of 12% and length scale of 0.08 m are also prescribed at this location based on wind tunnel turbulence spectral measurements as outlined in Section 6.2.2. For simplicity, the inlet temperature field was defined to be uniform with a value of 310 Kelvin. No approach flow near-wall heating was applied.

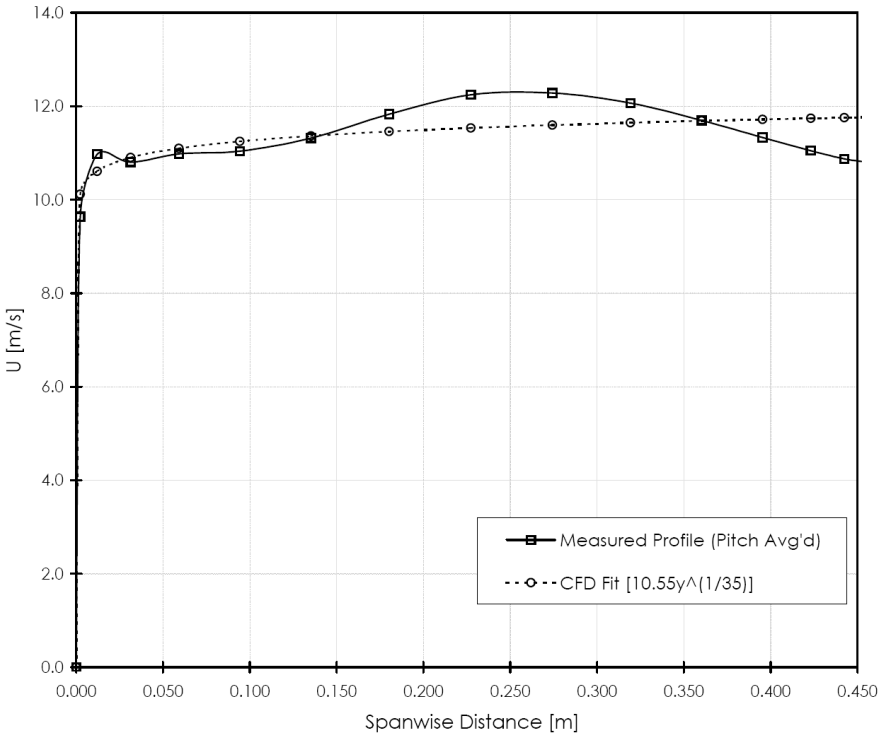

Figure 94. Test Section Pitch Averaged Inlet Velocity Profile w/ approx. Curve Fit (For CFD)

The velocity inlet condition for leakage flow injection was based on the required MFR and slot area. The MFRs evaluated (0.5%, 1.0%, 1.5%) result in three velocity boundary conditions of 1.944, 3.888, and 5.832 m/s, respectively. The leakage flow temperature was prescribed to be 290 Kelvin. This temperature difference between the leakage and main flows allowed for the calculation of adiabatic effectiveness along each endwall.

Each model was run until convergence criteria were met and the grids were then refined. The model was solved again until a grid-independent solution was verified. In all cases, a stable steady-state solution was found to exist.

8.1.2 Results

Results from these calculations are given in Figure 95 through Figure 99. Figure 95 shows the velocity distribution at the leakage slot for the shark nose endwall geometry (3 MFR cases). The computed velocities are normalized on the wind tunnel freestream

velocity, U_∞. In all three cases of different leakage flow rates, the slot flow distribution shows both outflow and inflow with respect to the leakage plenum. This finding suggests that mainstream flow ingression is possible under the given conditions. In general, designers seek to minimize ingression or avoid it altogether.

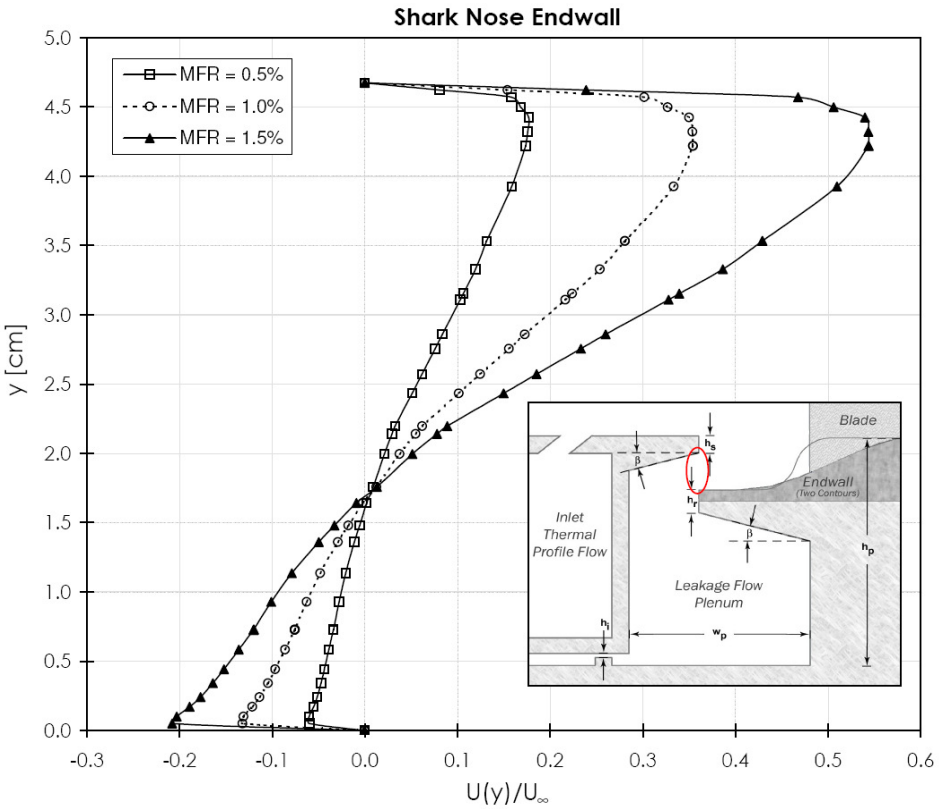

Figure 95. Normalized Velocity Profile at Leakage Slot for Shark Nose Endwall

Figure 96 displays similar velocity distributions for simulations run with the dolphin nose geometry. As was seen with the shark nose endwall cases, the velocity profiles for the dolphin nose endwall are roughly of the same shape, only differing in magnitude due to changes in leakage flow rate. This suggests that the flow structures created due to the geometry are fairly independent of leakage flow rates, within the 0.5-1.5% MFR range. This appears to be true for computations of both endwall contours.

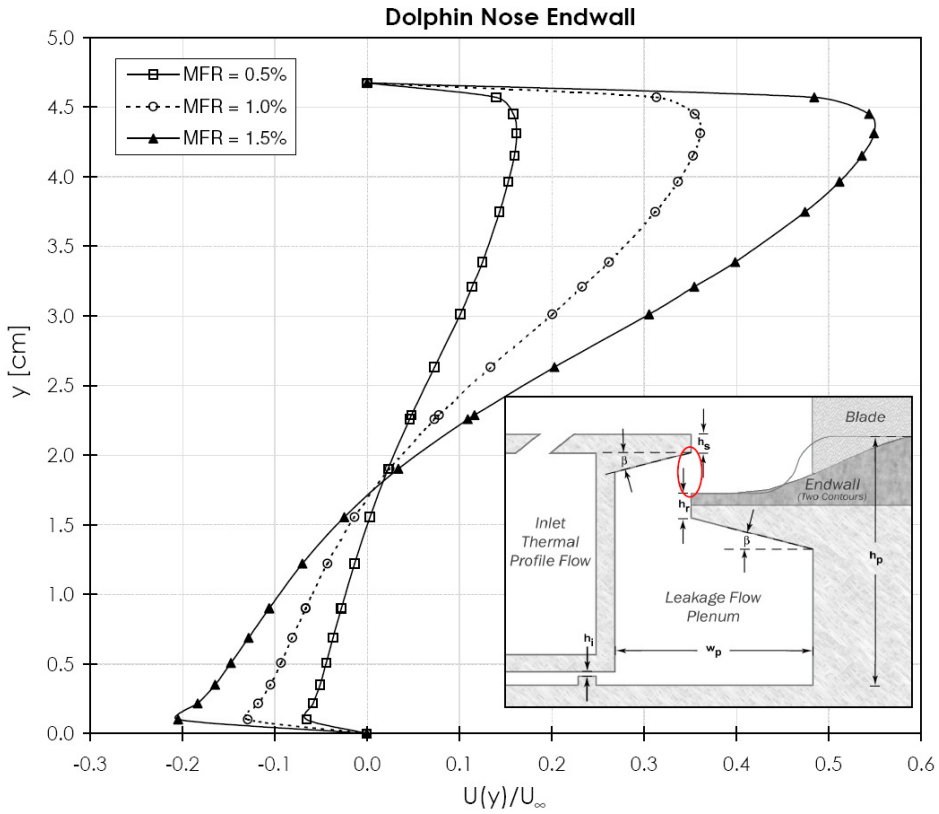

Figure 96. Normalized Velocity Profile at Leakage Slot for Dolphin Nose Endwall

The idea that flow structures near the leakage slot remain similar throughout the tested range of leakage flows can be further explored by viewing streamline patterns in Figure 97 through Figure 99. These plots also show static temperature contours which help visualize passage flow and leakage flow mixing. In viewing these plots, one sees that a large circulation exists over the contoured section of both the dolphin nose and shark nose endwalls. This circulation is driven by the mainstream flow and thus rotates in the clockwise sense. In the case of 0.5% leakage MFR (Figure 97), the circulation above the contoured endwalls entrains mainstream fluid. This in turn increases endwall temperatures in this area. Another circulation pattern is seen for both endwalls beneath the stator lip. For the case of the shark nose endwall, at 0.5% leakage MFR, this structure draws mainstream fluid further into the disc cavity. In general, the streamlines for all six cases verify flow structures near the endwall and inside the disc cavity have little dependence on leakage flow rate within the range tested. The only major trend that leakage flow rate seems to cause is the lowering of the vortex directly above the endwall

contour as flow rate is increased. While these results do not consider all of the important parameters within a real turbine, they give an idea as to some of the flow patterns and level of mixing that may occur.

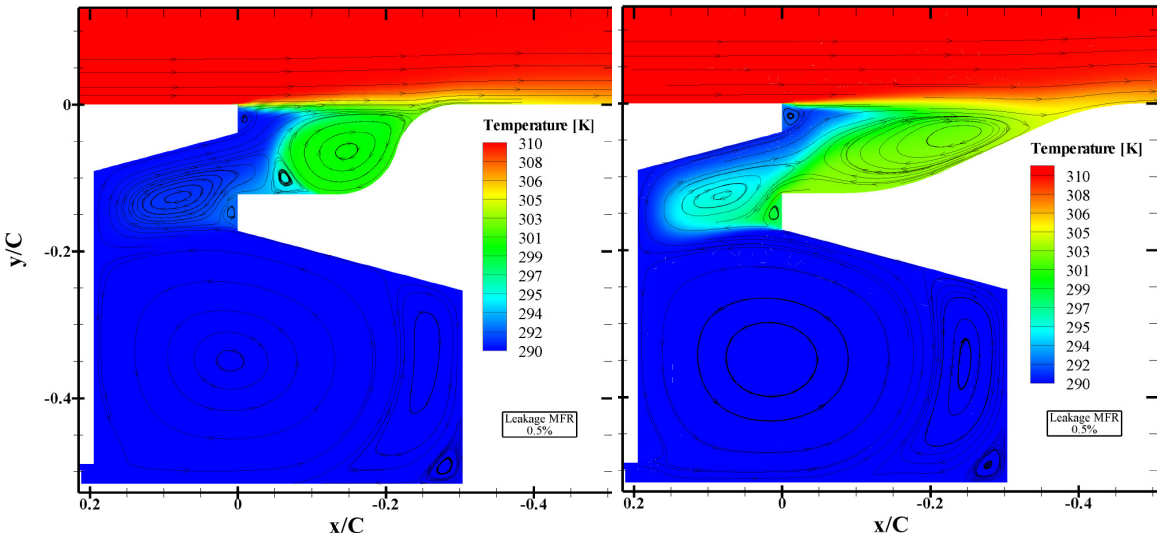

Figure 97. Streamlines and Contours of Temperature for Dolphin nose (left) and Shark nose (right) Endwalls with MFR = 0.5%

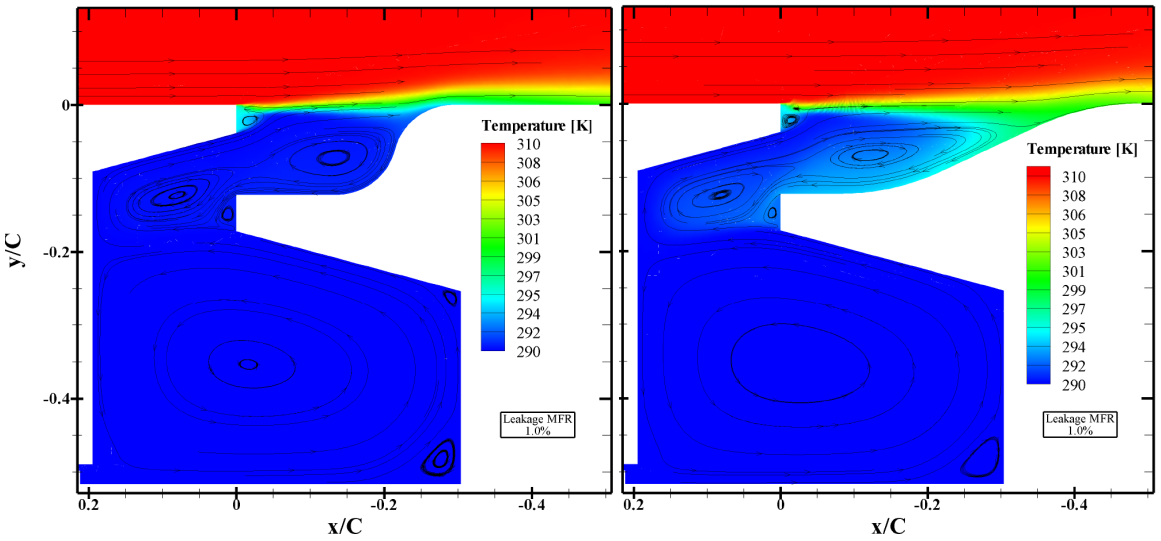

Figure 98. Streamlines and Contours of Temperature for Dolphin nose (left) and Shark nose (right) Endwalls with MFR = 1.0%

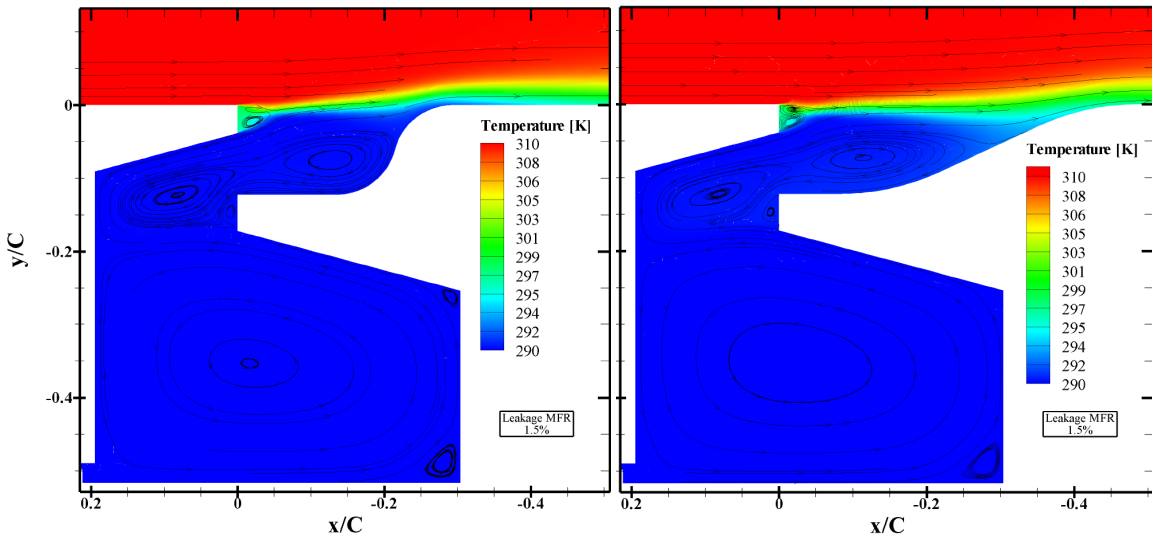

Figure 99. Streamlines and Contours of Temperature for Dolphin nose (left) and Shark nose (right) Endwalls with MFR = 1.5%

Endwall temperature data were also extracted from each simulation and used to calculate adiabatic effectiveness distributions along the endwall. This information is plotted in Figure 100. In the case of all three leakage mass flow ratios, the dolphin nose endwall geometry shows higher adiabatic effectiveness magnitudes. When Figure 100 is compared with temperature contours given in Figure 97 through Figure 99, it is seen that flow coming from the leakage slot has less axial distance to travel, and thus mixes, before the wall contouring is complete in the dolphin nose endwall geometry. In effect, this results in better displacement of the mainstream flow away from the endwall.

When the computational results of endwall adiabatic effectiveness are compared with those measured in Section 7.3.4, one can see that the two-dimensional model over predicts effectiveness values. This is largely due to the exclusion of blade effects, the cross-stream pressure gradient, and secondary flows.

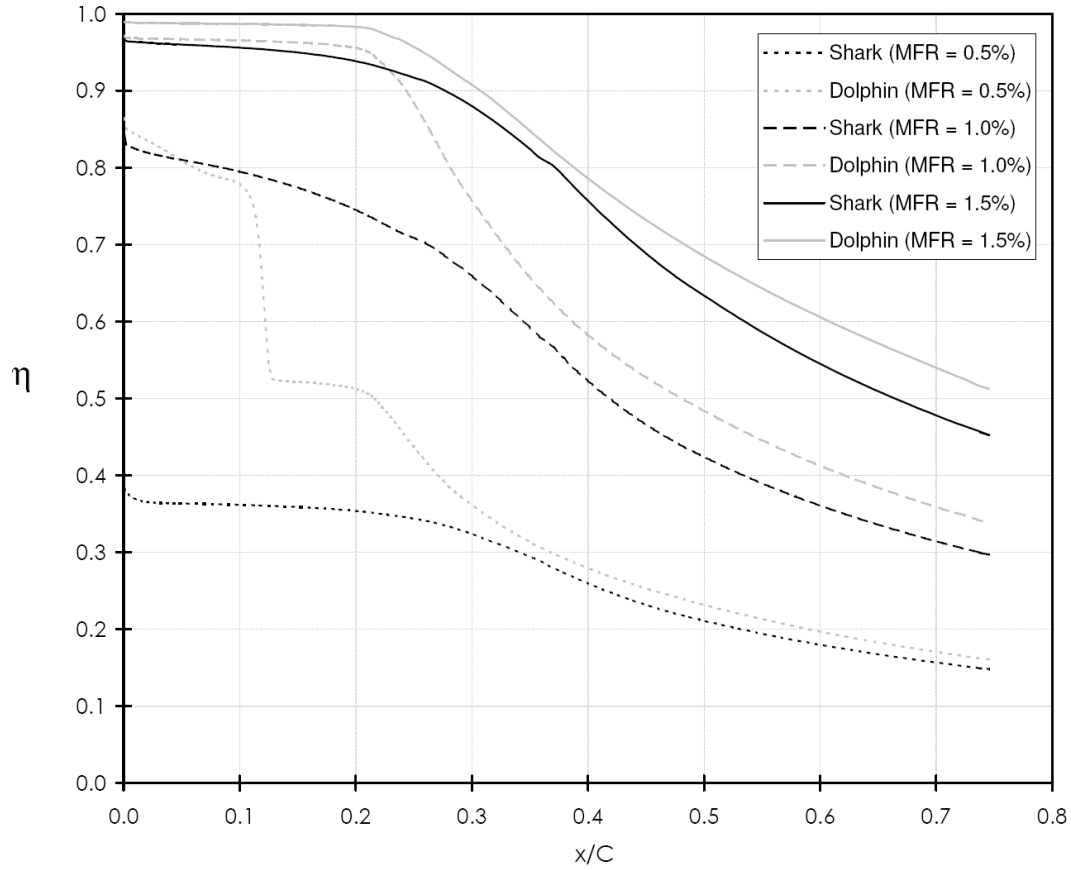

Figure 100. Adiabatic Effectiveness Distributions for Shark and Dolphin Nose Endwalls at 3 Mass Flow Ratios

8.2 3D Unsteady CFD Study of Test Section Geometry

A computational study is conducted using the commercial CFD software *FLUENT* to complement the measurements. Three-dimensional models are created for both the dolphin nose and shark nose endwall contour designs which include blades and the disc cavity plenum. These models are used for a study which more completely replicates all features found in the experimental test facility when compared to those of the previous section.

8.2.1 Methodology

The computational domain is displayed in Figure 101. This domain is an exact replication of wind tunnel test section dimensions at full scale. Meshing was performed using the commercial software *Harpoon*. The models for the two geometries have grid arrays containing roughly three million quadrilateral cells each and are refined near boundaries. The endwall boundary region has a finer mesh with y^+ values around 5. The use of such a large grid was facilitated through parallel processing provided by resources at the Minnesota Supercomputing Institute [49]. Even with the resources available, this large of a model proved to be cumbersome. Due to these difficulties, grid refinement studies were not carried out. For this and other reasons, calculations made in this study should neither be considered complete nor of high fidelity.

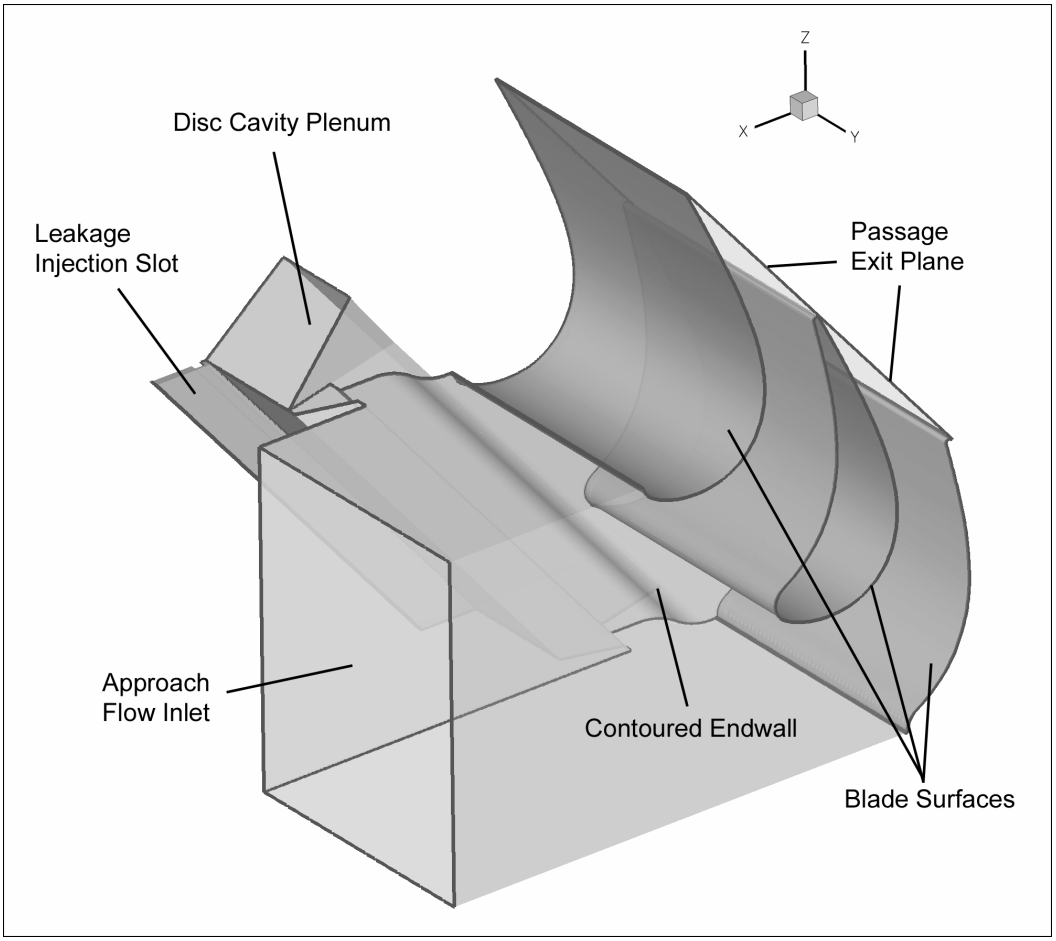

Figure 101. 3D CFD Domain which Replicates Wind Tunnel Test Section

Boundary conditions for the three dimensional models are prescribed based upon measurements from the linear cascade test section. Inlet boundary conditions have a prescribed total pressure and uniform temperature. Only cases of leakage MFR=1% are evaluated with the 3D models. The k-ω shear stress transport (SST) model is used for turbulence closure, with turbulence intensities and length scales provided from the cascade turbulence measurements taken at an upstream station (reported in Table 4). Mixing between the mainstream and leakage fluid is visible through study of the unsteady temperature profiles on endwall-normal planes. The endwall surfaces are adiabatic, allowing for adiabatic effectiveness values to be calculated from the temperature field. At the outlet of each domain is a static pressure condition set according to test section measurements. Losses in total pressure at this outlet are also evaluated.

8.2.2 Results

Time-averaged cascade measurements are compared to time-averaged values of the computational results to gain a better understanding of flow behavior in the leakage-to-passage flow mixing region and its effects on passage performance. As noted, the comparison values are time-averaged values taken from the unsteady calculation. These values are considerably different than values from a steady-flow solution of this highly-unsteady mixing flow. Though the CFD results must be treated as preliminary, they are suitable for a qualitative comparison. Results from the dolphin nose endwall CFD model (MFR=1.0%) are given in Figure 102 as contour plots of loss coefficients calculated by (Eq. 5.1). It is seen in this plot that calculated loss coefficient values are higher than those from the measurements (Figure 56). This discrepancy appears to be attributable to the CFD turbulence model. The model predicts higher than actual turbulence dissipation rates; which, in turn, causes stagnation pressure to drop excessively in all parts of the flow. This seems to be typical of cases with high-intensity, large-scale turbulence. It is expected that all forms of the RANS modeling tend to predict dissipation rates that are too large under these conditions.

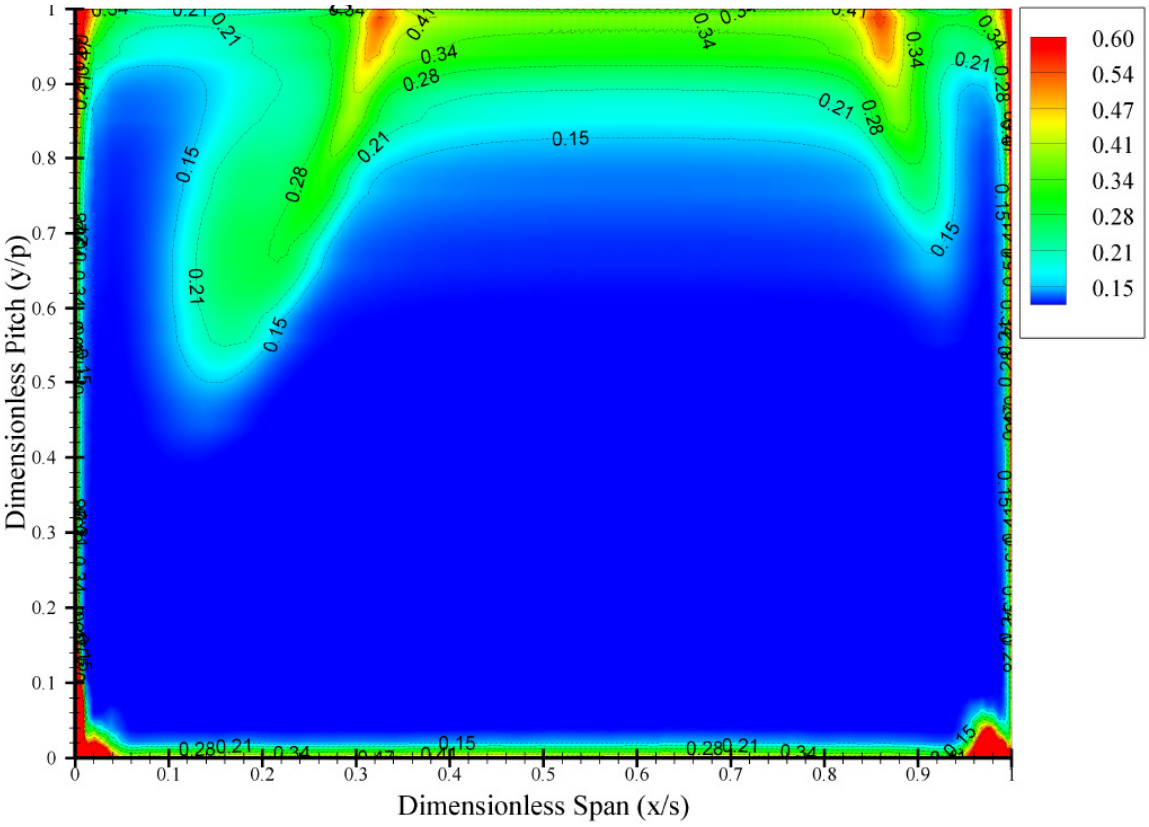

Figure 102. 3D CFD Passage Exit Plane Loss Coefficients for Dolphin Nose Endwall with 1.0% Leakage MFR. Contoured Endwall, x/s=0; Pressure Surface, y/p=0; Suction Surface, z/p=1.

Several notes may be made when comparing Figure 102 (calculated results) with Figure 56 (measured results). First, the boundary layers leaving the blade's trailing edge on the pressure side are similar in thickness. The CFD results show high losses near the two lower blade/endwall corners (locations (0, 0) and (1, 0)). Though such corner losses are expected, they are not prominent in the measurements shown in Figure 10. In both the measured and computed cases, the contoured endwall boundary layers increase in thickness as one's view traverses from the pressure side to the suction side of the passage. As stated previously, this is likely due to cross-stream pressure gradient washing boundary layer fluid toward the suction side. It may also be partially due to the further streamwise distance traveled in the skewed endwall flow. Measurements could not be taken nearer than x/s ~ 0.98 to the straight endwall. In comparing Figure 102 with Figure 56, one also sees that the passage vortices which lift off of both the contoured and flat endwalls reside at similar locations near the suction side trailing edge. The passage vortex

on the contoured endwall side separates from the suction wall at about the location (0.34, 1). The vortex near the flat endwall departs at about (0.83, 1). The sizes of these structures do vary between the measured and computed results. The CFD results show more build-up of lossy fluid in the contoured endwall vortex area and less in the flat endwall vortex area. The computed results also show less dispersion of the lossy flow, again presumed to be a product of greater dissipation of turbulence and reduced eddy diffusivity within the passage of the computed flow.

Loss coefficient results from the shark nose endwall CFD model (MFR=1.0%) are given in Figure 103. A comparison can again be made between the computed (Figure 103) and measured (Figure 59) loss coefficient results which reveals similar findings to those described with the dolphin nose endwall geometry. One major discrepancy, however, is the location of the loss core nearest the contoured endwall. The CFD calculations show a loss core which has lifted away from the endwall to approximately x/s=0.25 on the blade suction surface while the measured data suggests x/s=0.35. Additionally, the computational results show higher peak loss values which have diffused less than those in the measurements.

A comparison of results in Figure 102 and Figure 103 shows the computed differences in exit plane losses due to the different endwall contour geometries. The dolphin nose geometry leads to higher losses, in general, and a larger area influenced by the roll-up vortex in the contoured-to-suction wall corner. Also, that vortex rises higher on the suction surface wall. The general features of the lossy regions are the same, indicating that secondary flow structures are not strongly influenced by the change from one entry flow geometry to the other. Interestingly enough, the conclusion that the dolphin nose endwall geometry results in higher stage losses than the shark nose geometry is opposite of what was concluded in the measured results. Determining the cause of such differences between computational and experimental results would require further investigation.

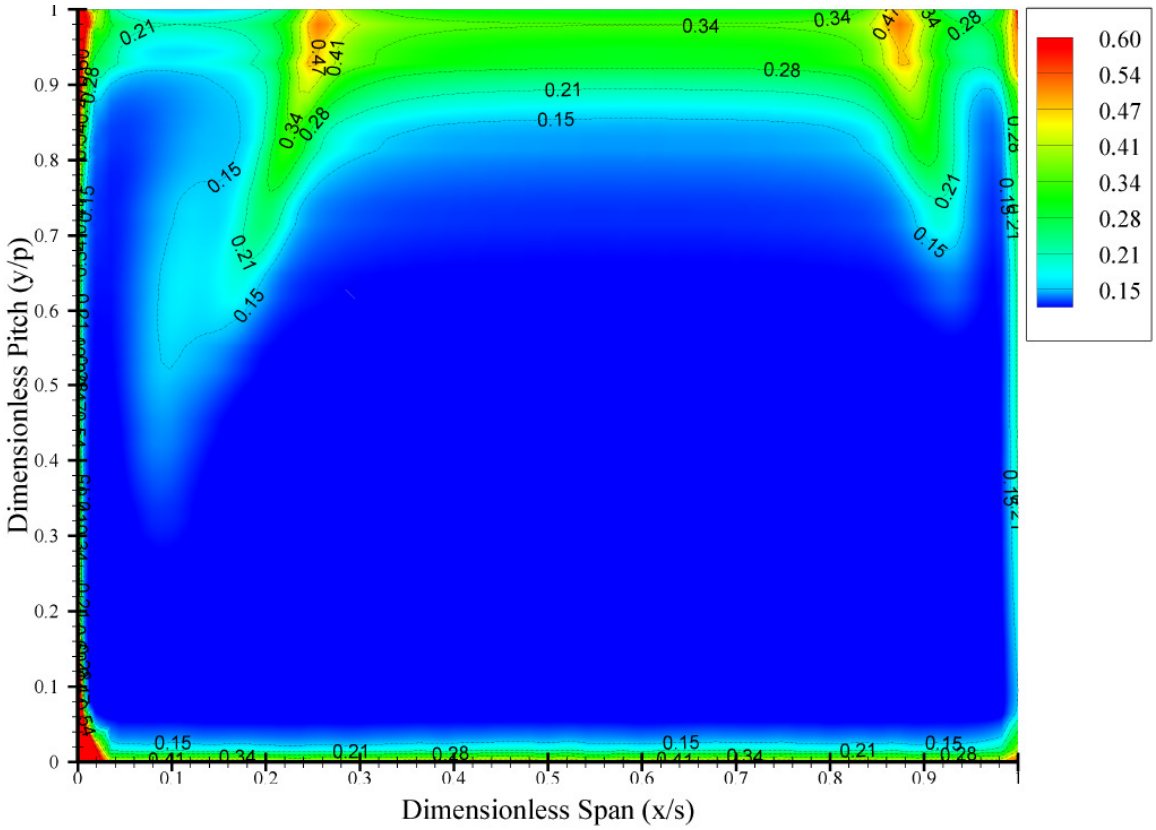

Figure 103. 3D CFD Passage Exit Plane Loss Coefficients for Shark Nose Endwall with 1.0% Leakage MFR. Contoured Endwall, x/s=0; Pressure Surface, y/p=0; Suction Surface, z/p=1.

Computed adiabatic effectiveness contours for both the dolphin nose and shark nose endwall geometries at a leakage MFR=1.0% are shown in Figure 104. The measured equivalents were reported in Figure 68 (dolphin) and Figure 77 (shark). A comparison between computed and measured results shows that the effectiveness values are generally higher in the computed case than in the experiments. This may be due to the computed more-rapid decay of turbulence leading to reduced mixing and higher effectiveness values. Generally, the pattern of coverage is the same between the computed and measured distributions; thus, the computations seem to capture the secondary flowfield appropriately. The effects of the horseshoe and passage vortices are clear in both. The computational results in the endwall region upstream of contouring show curious patterns, however. This area experiences highly unsteady flow. Also, the computed plot shows periodicity in the effectiveness pattern from one passage to the next, as it must be,

but the measurements show that this was not attained due to end effects where the upper passage meets the tunnel wall region.

A comparison between computed endwall effectiveness profiles for the dolphin and shark nose geometries in Figure 104 shows that the secondary flows in the passage have a stronger influence over the pattern for the shark nose geometry. The cooling coverage area is slightly decreased and a definite decrease in magnitude is seen.

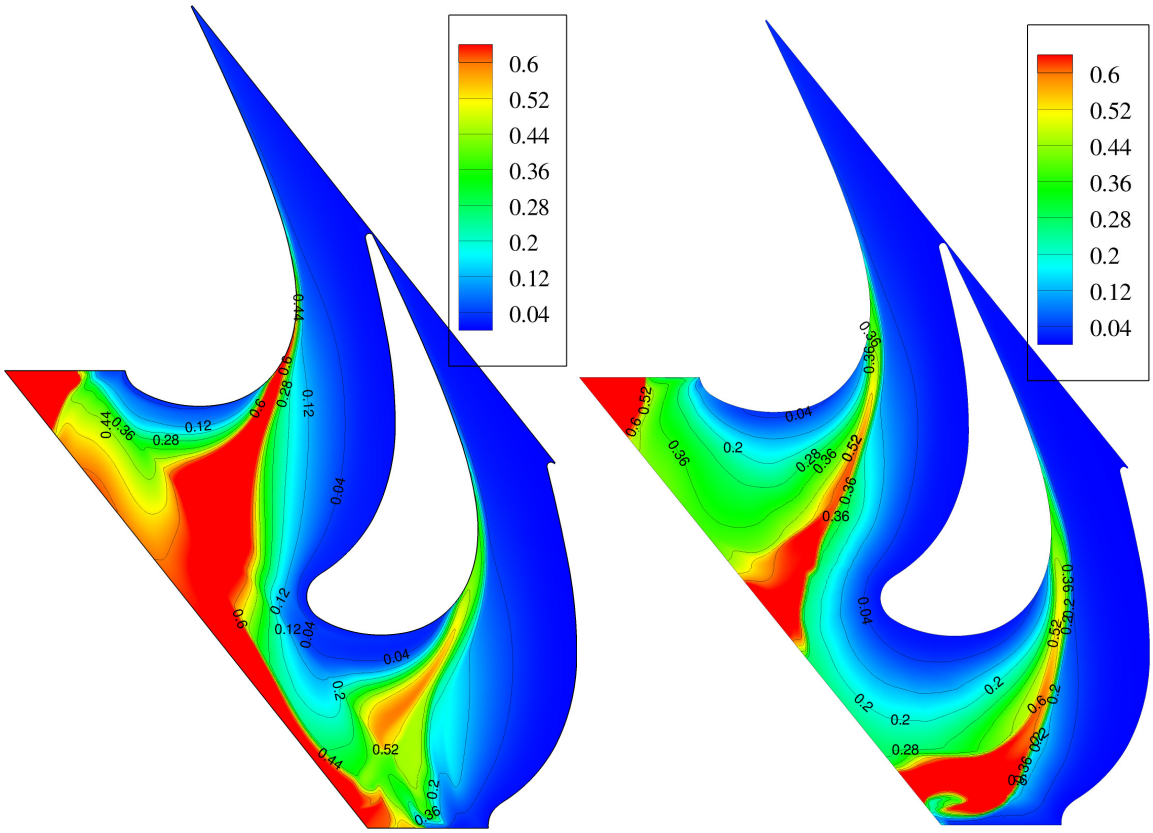

Figure 104. 3D CFD Results for Endwall Adiabatic Effectiveness on Dolphin Nose (Left) and Shark Nose (Right) Endwalls at Leakage MFR=1.0%

Chapter 9

Conclusions

An experimental study of passage flow and leakage flow mixing around the hub endwall region in a linear cascade of rotor blades has been performed. The subject of endwall contouring has been investigated through the inclusion of two different endwall profiles. These profiles have been referred to as the "dolphin nose" and "shark nose" contours. Leakage flow is injected from a plenum which replicates dimensions found in a disc cavity between stator and rotor blades. The leakage flow rate is metered and set at mass flow ratios of 0.5%, 1.0%, and 1.5% of the passage approach flow rate during these tests. Additionally, the wind tunnel facility operates at an engine representative Reynolds number ($\mathrm{Re}_c \approx 430{,}000$ based on inlet velocity and blade chord length). A combustor simulator is used to generate a uniform inlet freestream turbulence at high intensities ($Tu \approx 14\%$) and large length scales ($\Lambda / C \approx 10\%$) at $x / C_{ax} = -0.58$.

Measurements made within the test section include passage exit plane total pressure loss contours, endwall adiabatic effectiveness contours, and passage thermal field maps. Each of these measurements were made separately with both the dolphin nose and shark nose endwall geometries in place, and for each of the three disc cavity leakage mass flow ratios. A total of six different cases for each measurement type allows for endwall contouring and leakage flow rate effects to be evaluated. Additional thermal cases have been incorporated in this study to evaluate the importance of stator exit (pre-leakage flow injection) temperature profiles on endwall adiabatic effectiveness values.

During wind tunnel operation, disc cavity flow ingression was found to occur as evidenced by measurements of passage thermal fields. Simply stated, ingression is the occurrence of mainstream fluid traveling into the disc cavity between stator and rotor rows. The most upstream passage thermal field map showed this occurrence as a reduction in temperature between the rim seal location and leakage slot. This finding was shown to be dependent upon leakage mass flow ratio. Increases in leakage MFR led to increases in temperatures (less flow ingression) at the leakage slot. The two endwall

contours tested were found to have no significant effect on the occurrence of ingression. Additionally, flow in the region of the leakage slot was found to be highly unsteady. An important parameter (other than the leakage mass flow rate) affecting the amount of disc cavity ingression is hypothesized to be the leakage slot area. This dimension directly determines velocities which will occur at the leakage slot for a given flow rate. The conventional wisdom is that higher leakage slot velocities (pressures) will be less susceptible to backflow. A minimal disc cavity leakage flow is typically sought to keep its efficiency penalty small. A reduction in leakage slot area is a way of combating ingression without increasing leakage flow. These considerations must of course be balanced with the need for sufficient clearance between the rotor and stator.

Conclusions regarding the effects of endwall contouring are now discussed. With respect to aerodynamic losses, the two endwall contours tested produced fairly similar results. Mass averaged pressure coefficient calculations for the two contours differed by only 1%, on average. Data reveal that the dolphin nose endwall contour provided a slight advantage in reduction of losses. The passage exit plane loss measurements showed also that loss cores (due to passage vortices) were present in the same locations regardless of endwall contour. Their shapes and sizes were roughly the same as well. A comparison of thermal performance between the endwall contours was made through endwall adiabatic effectiveness and passage thermal field results. Endwall cooling coverage patterns remained the same size and shape regardless of endwall contour. This signifies the relative strength of passage secondary flows on endwall cooling. The extent to which leakage flow provided cooling utility within the passage was limited by the passage vortex separation line. This line was clearly seen in all endwall thermal measurements. While the endwall adiabatic effectiveness patterns for both contours were roughly of the same shape and size, their magnitudes differed. The dolphin nose contour consistently produced higher effectiveness magnitudes at equivalent leakage flow rates. This finding was corroborated and further explained by the passage temperature field measurement results. By comparing temperature fields of similar cases, one can see that the shark nose endwall contour causes a slight displacement of leakage flow away from the endwall surface. It was seen most clearly near the leading edge plane, and occurred with all three

leakage flow rates tested. The net effect was a diminished utility of leakage flow with the shark nose endwall contour. This occurrence was not seen with the dolphin nose contour as its acceleration profile kept leakage flow closer to the endwall surface.

The variation of disc cavity leakage flow rate was also documented. Measurements revealed no statistically significant change in pressure losses as a result of varying the leakage mass flow ratio between 0.5% and 1.5%. This finding was not expected, however certainly plausible since the amount of leakage flow injected was very small relative to the mainstream flow rate. Thermal measurements on the endwall revealed that increasing the leakage flow rate directly increased adiabatic effectiveness values. Pitchwise averaged effectiveness data showed also that increasing the leakage MFR from 1.0 to 1.5% produced diminishing returns when compared to an increase from 0.5 to 1.0%. This was true irrespective of endwall contour.

A further investigation carried out determined the significance of stator exit temperature distribution on endwall adiabatic effectiveness results. A relatively thin layer of heated, near-wall fluid in the approach flow immediately upstream of leakage flow injection showed a significant augmentation of adiabatic effectiveness values. This occurred as far upstream as the leakage slot which indicated the approach flow's strong mixing behavior with the leakage flow within the slot. This finding suggests that a more accurate picture of endwall heat transfer can be obtained only through the inclusion of rotor inlet temperature profiles. This information which is difficult to find in the current literature, merits consideration for further investigation.

Bibliography

[1] Langston, L.S., 2009, "The Role of Gas Turbines in Global Energy Conversion," *ICHMT Turbine 09*, *International Symposium on Heat Transfer in Gas Turbine Systems*, Antalya, Turkey.

[2] Sieverding, C.H., 1985, "Recent Progress in the Understanding of Basic Aspects of Secondary Flows in Turbine Blade Passages," ASME J. of Turbomachinery, **114**, pp. 248-257

[3] Sieverding, C. H., and Van den Bosch, P., 1983, "The Use of Coloured Smoke to Visualize Secondary Flows in a Turbine-Blade Cascade," ASME J. of Fluid Mechanics, **134**, pp. 85-89.

[4] Langston, L.S., 1980, "Crossflows in a Turbine Cascade Passage," ASME J. of Engineering for Power, **102**, pp. 866-874.

[5] Langston, L.S., 2000, "Secondary Flows in Axial Turbines-A Review," *ICHMT Turbine 2000*, *International Symposium on Heat Transfer in Gas Turbine Systems*, Annals of the New York Academy of Sciences, edited by R.G. Goldstein, **934**, pp. 11-26.

[6] Wang, H.P., Olson, S.J., Goldstein, R.J., and Eckert, E.R.G., 1997, "Flow Visualization in a Linear Turbine Cascade of High Performance Turbine Blades," ASME J. of Turbomachinery, **119**, pp. 1-8.

[7] Simon, T.W., Piggush, J.D., 2006, "Turbine Endwall Aerodynamics and Heat Transfer," AIAA J. of Propulsion and Power, **22**, No. 2, pp. 301-312.

[8] Sharma, O.P., and Butler, T.L., 1987, "Predictions of Endwall Losses and Secondary Flows in Axial Flow Turbine Cascades," ASME J. of Turbomachinery, **109**, pp. 229-236.

[9] Goldstein, R. J., and Spores, R.A., 1988, "Turbulent Transport on the Endwall in the Region between Adjacent Turbine Blades," ASME J. of Heat Transfer, **110**, pp. 862-869.

[10] Dénos, R., Paniagua, G., 2002, "Influence of the Hub Endwall Cavity Flow on the Time-Averaged and Time-Resolved Aero-Thermodynamics of an Axial HP Turbine Stage," *ASME Turbo Expo 2002,* GT2002-30185.

[11] Blair, M.F., 1974, "An Experimental Study of Heat Transfer and Film Cooling on Large-Scale Turbine Endwalls," ASME J. of Heat Transfer, **96**, pp. 524-529.

[12] Biesenger, T.E., Gregory-Smith, D.G., 1993, "Reduction of Secondary Flows and Losses in a Turbine Cascade by Upstream Boundary Layer Blowing," *ASME Turbo Expo 1993*, 93-GT-114.

[13] Owen, J.M., 1988, "Air-Cooled Gas Turbine Disks: a Review of Recent Research," Int. J. of Heat and Fluid Flow, **9**, No. 4, pp. 354-365.

[14] Bhavnani, S.H., Khodadadi, J.M., Goodling, J.S., and Waggott, J., 1992, "An Experimental Study of Fluid Flow in Disk Cavities," ASME J. of Turbomachinery, **114**, pp. 454-461.

[15] Ko, S.H., and Rhode, D.L., 1992, "Thermal Details in a Rotor-Stator Cavity at Engine Conditions with a Mainstream," ASME J. of Turbomachinery, **114**, pp. 446-453.

[16] Cao, C., Chew, J.W., Millington, P.R., and Hogg, S.I., 2003, "Interaction of Rim Seal and Annulus Flows in an Axial Flow Turbine," *ASME Turbo Expo 2003,* GT2003-38368.

[17] Paniagua, G., Dénos, R., and Almeida, S., 2004, "Effect of the Hub Endwall Cavity Flow on the Flow-Field of a Transonic High-Pressure Turbine," *ASME Turbo Expo 2004,* GT2004-53458.

[18] Pau, M., Paniagua, G., Delhaye, D., de la Loma, A., and Ginibre, P., 2008, "Aerothermal Impact of Stator-Rim Purge Flow and Rotor-Platform Film Cooling on a Transonic Turbine Stage," *ASME Turbo Expo 2008,* GT2008-51295.

[19] Burd, S.W., 1998, "Secondary Flow and Heat Transfer Control in Gas Turbine Inlet Nozzle Guide Vanes," Ph.D. Thesis, University of Minnesota, Minneapolis, MN.

[20] Girgis, S., Vlasic, E., Lavoie, J.P., and Moustapha, S.H., 2002, "The Effect of Secondary Air Injection on the Performance of a Transonic Turbine Stage," *ASME Turbo Expo 2002*, GT2002-30340.

[21] Ong, J.H.P., Miller, R.J. and Uchida, S., 2006, "The Effect of Coolant Injection on the Endwall Flow of a High Pressure Turbine," *ASME Turbo Expo 2006,* GT2006-91060.

[22] Marini, R., and Girgis, S., 2007, "The Effect of Blade Leading Edge Platform Shape on Upstream Disk Cavity to Mainstream Flow Interaction of a High-Pressure Turbine Stage," *ASME Turbo Expo 2007,* GT2007-27429.

[23] Oke, R.A., 2000, "Measurements in a Gas Turbine First Stage Nozzle Guide Vane Cascade with Film Cooling and Endwall Contouring," Ph.D. Thesis, University of Minnesota, Minneapolis, MN.

[24] Ames, F.E., 1994, "Experimental Study of Vane Heat Transfer and Aerodynamics at Elevated Level of Turbulence," NASA, Technical Report CR-4633.

[25] Chung, J.T., 1992, "Flow and Heat Transfer Experiments in the Turbine Airfoil/Endwall Region," Ph.D. Thesis, University of Minnesota, Minneapolis, MN.

[26] Wang, L., 1996, "A Study on Gas Turbine Flows, Turbulence Generation, and Film Cooling Flow Measurements," M.S. Thesis, University of Minnesota, Minneapolis, MN.

[27] Rowell, R.M., 2005, *Handbook of Wood Chemistry and Wood Composites*, CRC Press.

[28] Shaw, R., 1960, "The Influence of Hole Dimensions on Static Pressure Measurements," J. Fluid Mech., **7**, pp.550-564.

[29] Goldstein, R.J., 1996, *Fluid Mechanics Measurements*, Taylor & Francis.

[30] Sovran, G., Klomp, E.D., 1967, "Experimentally Determined Optimum Geometries for Rectilinear Diffusers with Rectangular, Conical or Annular Cross-Section," *Fluid Mechanics of Internal Flow*, Elsevier, New York.

[31] Hoffmann, J.A., 1981, "Effects of Free-Stream Turbulence on Diffuser Performance," ASME J. Fluids Engineering, **103**, pp.385-390.

[32] Piggush, J.D., 2005, "An Experimental Investigation of Endwall Leakage Flows and Misalignment in a Gas Turbine Nozzle Guide Vane Simulator," M.S. Thesis, University of Minnesota, Minneapolis, MN.

[33] Velmex, Inc., http://www.velmex.com

[34] King, L.V., 1914, "On the Convection of Heat from Small Cylinders in a Stream of Fluid -Determination of Convection Constants of small Platinum Wires with Application to Hot Wire Anemometry," Philos. Trans. R. Soc., London, Ser. A, **214**, pp.373-432.

[35] TSI, Inc., http://www.tsi.com

[36] Wilson, D. J., 1970, "An Experimental Investigation of the Mean Velocity, Temperature and Turbulence Fields in Plane and Curved Two-Dimensional Wall Jets: Coanda Effect," Ph.D. Thesis, University of Minnesota, Minneapolis, MN.

[37] Adolphson, D.A., 2003, "Oscillatory and Unidirectional Fluid Mechanics Investigations in a Simulation of a Stirling Engine Expansion Space," M.S. Thesis, University of Minnesota, Minneapolis, MN.

[38] Laufer, J., 1953, "The Structure of Turbulence in Fully Developed Pipe Flow," NACA Rep. 1174.

[39] Crowe, C. T., Elger, D. F., Roberson, J. A., 2001, *Engineering Fluid Mechanics*, 7th ed, John Wiley & Sons, Inc.

[40] Hinze, J. O., 1975, *Turbulence*, 2nd ed., McGraw-Hill.

[41] Logan, J. D., 2006, *Applied Mathematics*, 3rd ed., John Wiley & Sons, Inc.

[42] Stull, R. B., 2008, *An Introduction to Boundary Layer Meteorology*, Springer.

[43] Tennekes, H., Lumley, J. L., 1972, *A First Course in Turbulence*, MIT Press

[44] Ames, F. E., Moffat, R. J., 1990, "Heat Transfer with High Intensity, Large Scale Turbulence: The Flat Plate Turbulent Boundary Layer and the Cylindrical Stagnation Point," Report No. HMT-44, Stanford University, Stanford, CA.

[45] Kolmogorov, A. N., 1941, "Dissipation of Energy in the Locally Isotropic Turbulence," Compt. rend. acad. sci. U.R.S.S., **32**, pp.16-18.

[46] Dwyer Instruments, Inc., *Bulletins D-57 and D-3*, http://dwyer-inst.com

[47] Validyne Engineering Corp., http://validyne.com

[48] Burns, G. W., Scroger, M. G., Strouse, G. F., Croarkin, M. C., Guthrie, W. F., 1993, "Temperature-Electromotive Force Reference Functions and Tables for the Letter-Designated Thermocouple Types Based on the ITS-90," Natl. Inst. Stand. Technol., Monograph 175.

[49] Minnesota Supercomputing Institute, www.msi.umn.edu, Minneapolis, MN

Appendix A – *ME DAQ* Software

Throughout the project it has been necessary to create code that assists with taking measurements - controlling stepper motors and processing raw data. Initially, this was done with a separate executable file for each specific measurement. A more general program suitable for all measurements within this study was desired. The program written for this purpose and its source code are included with the companion thesis DVD as *ME DAQ.exe*. It was written using the C++ programming language and also uses visual components from the Borland Visual Component Library (VCL). A brief overview of its functionality is given in Table 7 and is further explained in subsequent sections. A screenshot is provided in Figure 105 showing the graphical user interface layout.

Table 7. ME DAQ Functionality

	IOtech ADC488	Agilent 34970A	Traverse Only
Device Address	13	7	2
Channels	1, 2, or 4	1, 2, 4, or 8	N/A
Sample Rates (Hz)	5, 20, 100, 1k, 5k, 10k, 20k, 50k	1	N/A
Sample Times (sec)	5, 10, 20, 30, 60	10, 20, 60	N/A
Raw Data Output	Yes	Yes	No
Reduced Data Output	Yes	No	No
Plot (Ch. 1)	Yes	Yes	No
Variability Check (Ch 1.)	Yes	No	No
Traverse Control Option	Yes	Yes	Yes

Connectivity

The *ME DAQ* software is designed to control external hardware units from a computer with a Windows operating system. The computer must have either a GPIB PCI card installed, or have a USB-to-GPIB converter. A National Instruments model GPIB-USB-HS is used in this study which satisfies the latter option. Appropriate software and drivers must be installed on the machine to make GPIB communication possible as well. From either the PCI card or USB device, IEEE 488 (GPIB) cables must be connected to all hardware units which will be controlled. Hardware device addresses must be set

according to those listed in Table 7 for the software to function properly. At this time, these addresses are hard-coded within the software.

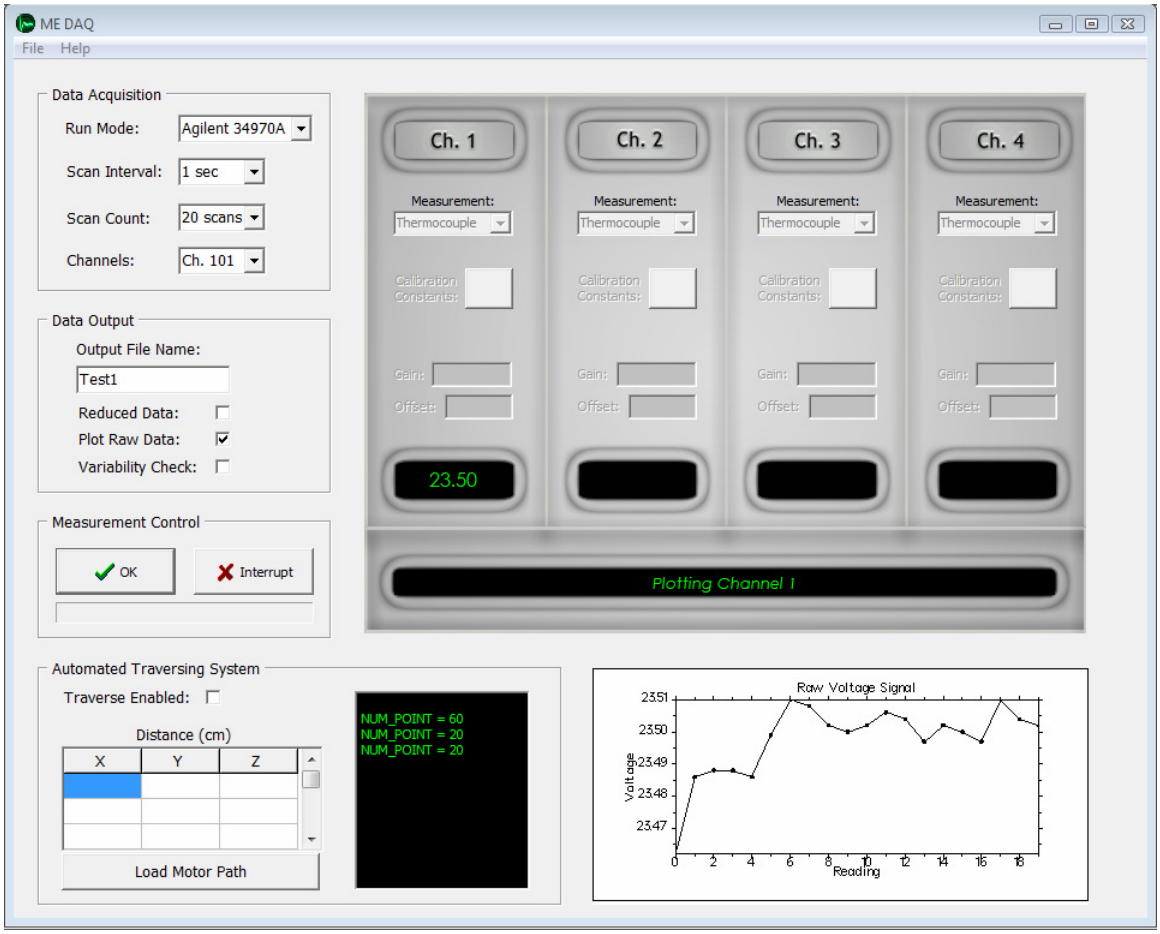

Figure 105. ***ME DAQ*** **Graphical User Interface**

Run Modes

There are three "Run Modes" available within the program: *IOtech ADC488*, *Agilent 34970A*, and *Traverse Only*. These modes are used to specify what hardware units are being controlled. Depending on the run mode selected, different features are available. The software's current capabilities are given in Table 7. In this study, the *IOtech ADC488* mode is used for voltage, velocity, and pressure measurements; the *Agilent 34970A* mode is used for temperature measurements; and the *Traverse Only* mode is used for controlling the 3-axis motor traverse without making measurements.

Data Output

Raw data are output from each series of measurements in the form of a ".csv" (comma-separated values) file. This format allows reading by any text editor or spreadsheet software and is platform independent. The file name for raw data is in the format of "*OutputFileName*_Raw.csv" and may be saved in any user-specified location. The "*OutputFileName*" is specified by the user and should contain no spaces. Each raw data file includes data acquisition settings (i.e. sample rate, sample time, etc…) for reference in the header section of the file, followed by columns for each reading taken.

Within the "Data Output" section of the program, there are three additional options which may affect output. These options are not available for every "Run Mode," as shown in Table 7. The first is the "Reduced Data" option. When selected, the "Reduced Data" checkbox causes the program to calculate values for the mean, standard deviation, and/or turbulence intensity of each reading depending on the type of measurement being taken. These calculations require "calibration constants" to be input for each channel before the measurement is taken. These values are input into the pop-up window and are specific to each type of measurement. The "Gain" and "Offset" constants are currently used only for velocity measurements. The converted data are output in a separate file in the same directory as the raw data file. The naming convention for the reduced data file is "*OutputFileName*_Sum.csv." This file contains the same header information as that of the raw data files.

The second data output option is the "Plot Raw Data" checkbox. When selected, this option causes a small plot to appear at the bottom right side of the screen at the end of each reading. It is meant to assist in giving the user a quick view of the raw data without having to use a separate plotting program. This is particularly useful when having to make test section adjustments based upon raw data. At the moment, the software supports plotting only data measured on channel 1. The plot is saved also in the working directory as "Plot.bmp" and can be opened as any other bitmap file. Be aware that this file is overwritten after each reading. If you would like to keep the small plot, you must rename it before taking another measurement.

The third and final data output option is the "Variability Check." When enabled, this option causes the program to calculate each reading's standard deviation and output that information in a text box. Currently, this feature calculates only the standard deviation of readings taken on channel 1. It was used in this study during measurements of passage aerodynamic losses to detect abrupt changes in pressure.

Automated Traversing System

The *ME DAQ* program also gives you the ability to control stepper motor movement between measurements by means of a Velmex Stepping Motor Controller/Driver. The model used in this study was a Velmex 3-axis NF90 series controller. Other models from Velmex may be compatible with this code so long as the controller commands have not changed. The automated traversing system feature was used to move probes throughout the test section which automated the measurement process. Before beginning a measurement, the program reads the "Traverse Enabled" checkbox and determines whether the feature will be used. If it is checked, the motor path table will be read and converted into commands. These commands will be executed one at a time prior to each measurement. If it is not checked, the program skips the traversing system code and executes one measurement at a time with user input needed to continue. No traverses need be connected for this option to work.

The "Load Motor Path" table is a list of (x,y,z) movements to take place before each measurement. The distances must be input in centimeters and refer to a "relative" (not absolute) coordinate system. For example, an input of (0,0,0) would cause no movement regardless of where the motor resides in the absolute coordinate system. Motor paths may be manually entered into the table, or loaded from an existing text file via the "Load Motor Path" button. The format of the text file is tab delimited containing three columns for the Motor 1, Motor 2, and Motor 3 commands, in order (as shown in Figure 106). If you would like to use fewer than three stepper motors, you must still enter values of zero in place of the unused motor. For example, the software would execute properly using the sample motor path below regardless of whether Motor 3 (far right column data filled with zeroes) was connected or not.

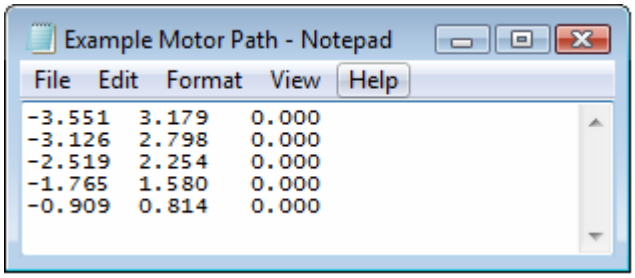

Figure 106. Example Motor Path Text (.txt) File

Save and Load Settings

If you are using the same settings and calibration constants frequently, you can simply save them for future use with the File->Save Settings option. This produces a settings file (.set) which can be loaded into the program at any time using File->Load Settings. Note that the settings files do not contain any information regarding the automated traversing system.